Università
Ca'Foscari
Venezia

Corso di Dottorato di ricerca
in Chimica
ciclo XXIX

Tesi di Ricerca

# Copper Sulfide and Copper Indium Sulfide Nanoparticles: Two Optically Active Materials with a Bright Future

SSD: CHIM/02

**Coordinatore del Dottorato**
ch. prof. Maurizio Selva

**Supervisore**
ch. prof.ssa Patrizia Canton
ch. prof. Fiorenzo Vetrone

**Dottorando**
Riccardo Marin
Matricola 810370

# Abstract

In this thesis, I present the results of the study on optically active copper sulfide and copper indium sulfide nanoparticles (NPs). These two materials are currently under intense study, since the last years of research have proved them to be viable, reliable, non-toxic, and cheap alternatives to the state of the art materials used in many application fields. They can be used for the production of theranostic agents (*i.e.* combining therapeutic and diagnostic capabilities), photovoltaic devices, sensors, and light emitting diodes, to name a few. The purpose of my research was to explore easy synthetic methods to produce NPs of these materials having specific characteristics, such as the possibility of dispersing them in polar organic solvents or better optical properties. In a second phase, I explored the effect of combining these NPs with rare-earth (RE) doped NPs to investigate the interaction between the two moieties and obtain augmented properties.

In the first chapter of the thesis, I briefly present the features of the two classes of optical materials I have been investigating during my doctoral studies: quantum dots (QDs) and plasmonic NPs (PNPs). Here, I describe the physical phenomena and the general features that characterize the behavior of these nanomaterials, later moving to a more specific look into copper indium sulfide ($CuInS_2$ – CIS) QDs and copper sulfide ($Cu_{2-x}S$ – CS) PNPs. In particular, I focus my attention on the description of their unique optical features and their great potential in many application fields, shortly reviewing the literature about the subjects.

In the second, third, and fourth chapter of the thesis, I present the results of my research on CIS QDs. Specifically, in the second chapter I discuss the properties of mercaptosilane-passivated CIS QDs synthesized via a simple one-pot thermal decomposition approach. The unique feature of these QDs is the possibility of dispersing them in organic polar solvents, a property that makes them attractive from an applicative viewpoint. Moreover, the slow reaction kinetics allow observing a growth mechanism characterized by the presence of QDs having discrete sizes, a behavior that was never reported in the literature. In the third chapter, I illustrate the effect that different halogen anions have on the final properties of CIS QDs when these ions are present in the reaction environment. I selected three halogenated salts (chloride, bromide, iodide) as the copper source and synthesized CIS QDs following a well-established thermal decomposition approach. Combining different characterization techniques, we observed evidences of the incorporation of the anions in the lattice. The results show that the

polarizability of the halogen ions affect the growth and the optical properties of the dots following the trend of the so-called *Hofmeister* series. In the fourth chapter, I expose the results of the study on the energy transfer (ET) mechanism between CIS QDs and upconverting NPs (UCNPs) doped with RE ions. I selected $LiYF_4$:Tm as the host-dopant combination for the UCNPs, and I investigated the effect that different core/shell donor (UCNP) and acceptor (QD) architectures have on the ET mechanism. I conducted the study both in solution and on samples dried on a substrate, in order to assess the nature of the ET (radiative versus non-radiative) between the two moieties. The results show that an intimate contact between the two moieties is the key factor to observe evidences of non-radiative ET.

In the fifth and sixth chapters of the thesis, I move to the study of CS PNPs, with a special focus on their potential as photothermal agents. In the fifth chapter, I present a study on CS PNPs synthesized via a newly developed green synthetic protocol. Variations of the reaction parameters such as temperature, pH, and copper-to-sulfur ratio allow for the control of the structural, morphological, and optical properties of the synthesized PNPs. In particular, I obtained quasi-spherical, pure phase covellite CS PNPs with a localized surface plasmonic resonance (LSPR) peak centered in the near-infrared region. These PNPs display a high heat conversion efficiency (HCE) of 44.2 %, a value that makes them a competitive cheaper substitute for the more studied gold-based photothermal agents. Moving from this observation, I am currently investigating the coupling of these $Cu_{2-x}S$ PNPs and RE-doped fluoride NPs. Specifically, the latter NPs were carefully designed in order to obtain both upconverted visible and near-infrared light emission under irradiation with continuous wave 980 nm laser. Thanks to the combination of the optical features of the two moieties, the so-composed nano-structure is expected to display charming properties as a potential theranostic agent.

*Dedicata ai miei genitori,*

*ai loro sacrifici e alle loro battaglie, che mi hanno cresciuto consapevole di quanto la vita possa togliere all'improvviso.*

## Ringraziamenti

Partiamo da chi mi ha supportato nell'ambiente accademico (e non solo). La prima persona che ringrazio è la Prof.ssa Patrizia Canton, mia *supervisor,* la quale mi ha accompagnato nel percorso tortuoso di dottorato guidandomi scientificamente ma sapendo anche risollevare dolcemente il mio spirito nei momenti di sconforto. Grazie per la stima mostratami e la continua interazione che non mi hai mai negato, anche nelle situazioni più "impegnative".

Ringrazio poi il mio *supervisor* per la parte canadese, il Prof. Fiorenzo Vetrone. Aver potuto lavorare nel gruppo di ricerca che ammiravo da anni è stata un'esperienza emozionante che mi ha fatto crescere grandemente come ricercatore. Grazie per il supporto datomi sotto ogni punto di vista e per i momenti meno formali e rilassati di giovialità.

Ringrazio tutti i miei compagni di ricerca, con i quali ho condiviso molti momenti in quello sperduto angolo di mondo che è Varennes. I neo-professori Rafik ed Eva, ma anche Marta, Miao, Yue, Joe ed i due neo-acquisti Chun e Alma. Una menzione particolare va ai due compagni di avventura, colleghi, compagni di ufficio, compagni di bevute e di alette di pollo piccanti: Antonio ed Artiom. Grazie per tutto il vostro supporto e per ogni momento speso assieme. Avete lasciato un segno profondo nel mio cuore e nel mio essere scienziato. Grazie Antonio per aver prestato occhi ed orecchie più di una volta alle mie richieste. E grazie Artiom, per esserci stato sotto ogni punto di vista, nonché per avermi fatto scoprire il mondo dell'arrampicata. Un ringraziamento va poi a tutti coloro che qui a Montreal ho conosciuto ed hanno fatto parte della mia vita a INRS e fuori dall'istituto. Su tutti Daniele per i molti pomeriggi e serate, nonché infinite pause caffè passate assieme. Poi tutta la gang italiana a INRS (Luca, Fabrizio, Andrea, Vincenzo, Gianluca, Matteo….) e fuori (Lidia, Paolo, Salvatore, Diego e molti altri). Un grazie altrettanto speciale va al coinquilino ed ineguagliabile amico Jason: grazie per esserci sempre stato e per avermi saputo aiutare con piccoli e grandi gesti in ogni momento di bisogno.

Non posso fare a meno di ringraziare anche Aurelie, Gianfranco, Emma e Luca, la mia famiglia di adozione qui a Montreal. Mi avete tenuto compagnia e lo spirito alto in questo ultimo periodo di scrittura della tesi soprattutto. Non esistono parole per ringraziarvi.

Ringrazio tutti i miei amici in Italia, che sono riusciti sempre a farmi sentire il loro calore ed affetto: Beppe, Taira, Tofy, Didi, Vale, Taira, Fede, Erika, Vanessa e Giulia su tutti. E tutti gli altri con loro. Mi sento fortunato ad essere circondato dall'affetto di queste persone meravigliose.

Ringrazio poi la mia famiglia: mia madre Cristina, mio padre Armando e mio fratello Dario. Siete stati sempre tutti presenti a modo vostro e come avete potuto, nonostante tutte le avversità e le difficoltà. Non avrei potuto raggiungere questo traguardo senza di voi, sulle cui spalle mi sono appoggiato molte volte. Grazie dal profondo del cuore. Un grazie va, poi a tutti i membri della mia famiglia che mi hanno pensato ed hanno dedicato almeno un pensiero a me durante questo periodo di distanza da casa.

# Table of Contents

**Abstract** ........ i

**Dedication** ........ v

**Ringraziamenti** ........ vi

**1 Introduction** ........ 1

**1.1 Quantum dots: evergreen nanoparticles** ........ 1

1.1.1 The physics of QDs ........ 1

1.1.2 Tailoring QD optical properties ........ 5

**1.2 Copper Indium Sulfide (CIS) QDs** ........ 7

1.2.1 Properties of bulk CuinS$_2$ ........ 7

1.2.2 Optical properties of CIS QDs ........ 8

1.2.3 Synthesis of CIS QDs ........ 13

1.2.4 Applications of CIS QDs ........ 19

**1.3 Plasmonic nanoparticles (PNPs)** ........ 25

1.3.1 The physics of PNPs ........ 25

1.3.2 The photothermal effect in PNPs and photothermal therapy ........ 29

**1.4 Copper sulfide plasmonic nanoparticles** ........ 31

1.4.1 Gold, the noble brother ........ 31

1.4.2 Copper sulfide PNPs: an affordable alternative ........ 33

**1.5 Aim of the research** ........ 39

**References** ........ 41

**2 Synthesis of mercaptosilane-passivated CIS QDs** ........ 53

**2.1 Materials and methods** ........ 54

2.1.1 Chemicals ........ 54

2.1.2 Synthesis of MPTS-passivated CIS QDs ........ 54

2.1.3 Characterization techniques ........ 55

**2.2 Results and discussion ........ 56**

2.2.1 Structural, morphological, and chemical characterization ........ 56

2.2.2 Optical characterization ........ 60

2.2.3 Solvent effect ........ 68

**2.3 Conclusions ........ 69**

**References ........ 71**

**3 Effect of halogen ions on the growth and properties of CIS QDs ........ 75**

**3.1 Materials and methods ........ 76**

2.1.1 Chemicals ........ 76

2.1.2 Synthesis of CIS QDs ........ 76

2.1.3 Characterization techniques ........ 77

**3.2 Results and discussion ........ 77**

3.2.1 Optical properties ........ 77

3.2.2 Structural and morphological characterization ........ 80

3.2.3 Interpretation of the anion effect ........ 87

3.2.4 Ongoing analyses ........ 88

**3.3 Conclusions ........ 89**

**References ........ 89**

**4 Study of the energy transfer between upconverting nanoparticles and CIS QDs ........ 92**

**4.1 Materials and methods ........ 93**

4.1.1 Chemicals ........ 93

4.1.2 Synthesis of nanoparticles ........ 93

4.1.3 Characterization techniques ........ 94

**4.2 Results and discussion ........ 96**

4.2.1 Material characterization ..... 96
4.2.2 Mathematical modelling of FRET ..... 100
4.2.3 Energy transfer in solution ..... 103
4.2.4 Energy transfer on dried samples ..... 110
4.2.5 Ongoing experiments ..... 114
**4.3 Conclusions ..... 115**
**References ..... 116**

**5 Green synthesis of highly PEGylated CuS plasmonic nanoparticles ..... 119**
**5.1 Materials and methods ..... 120**
5.1.1 Chemicals ..... 120
5.1.2 Synthesis of nanoparticles ..... 120
5.1.3 Characterization techniques ..... 120
**5.2 Results and discussion ..... 122**
5.2.1 effect of the S/Cu ratio ..... 122
5.2.2 Effect of the temperature ..... 124
5.2.3 Effect of the pH ..... 128
5.2.4 Effect of m-PEG amount ..... 129
5.2.5 Surface chemistry ..... 130
5.2.6 Heat conversion evaluation ..... 132
5.2.7 Free carrier density estimation and solvent effect ..... 134
**5.3 Conclusions ..... 136**
**References ..... 137**

**6 Summary and future work ..... 139**

# Chapter 1

## *Introduction*

*In this first Chapter, I will present the features of the two classes of optical materials I have investigated during my doctoral studies: quantum dots (QDs) and plasmonic nanoparticles (PNPs). I will briefly describe the physical phenomena that characterize the behavior of these nanomaterials, later moving to a more specific look into the class of copper-based sulfide semiconductors. In particular, I will focus my attention on copper indium sulfide ($CuInS_2$ – CIS) QDs and copper sulfide ($Cu_{2-x}S$) PNPs, highlighting their unique optical features and their great potential in many application fields.*

## 1.1 Quantum dots: evergreen nanoparticles

### 1.1.1 The physics of QDs

With the term *nano*-materials we refer to systems having at least one nanometric dimension. Specifically, the European Community has established that a nanomaterial can be referred to as such if at least one of its features falls in the 1-100 nm range[1]. When we reduce the size of a material to this scale, the behavior of the system changes dramatically, due to modifications of its electronic properties[2]. Here, we are particularly interested in the case of semiconductors, a well-known class of materials displaying a behavior between that of metals and insulators. In semiconductors, it is possible to define 3D (bulk), 2D (quantum well), 1D (quantum wire), and 0D (quantum dots - QD) structures depending on the number of spatial dimensions along which the free electronic motion is limited[3] (Figure 1.1a). The variation of the material size brings a modification of the electronic band structure, *i.e.* the density of states (DOS), and consequently a change of the properties influenced by electronic processes, such as electrical and heat conduction, or light absorption and emission. To understand how this phenomenon affects the optical properties of a semiconductor, it is useful to understand how the DOS changes for isotropic particles, from the bulk down to clusters of few atoms. When reducing the size of a semiconductor to the nanometric scale, its bandgap widens, *i.e.* the distance between the occupied valence band (VB) and the unoccupied conduction band (CB) increases. A further decrease of the size leads to a severe discretization of the electronic levels. We can describe this effect the other way around according to the Linear Combination of Atomic Orbitals (LCAO) theory (Figure 1.1b and 1.1c). The formation of bonds among atoms leads to a gradual decrease of the energy separation between the Highest Occupied Molecular Orbital (HOMO) and the Lowest Unoccupied Molecular Orbital (LUMO) and to more close-spaced energy levels. Eventually, this process leads to the creation of continuous bands, whose distance in energy is the so-called energy gap ($E_g$).

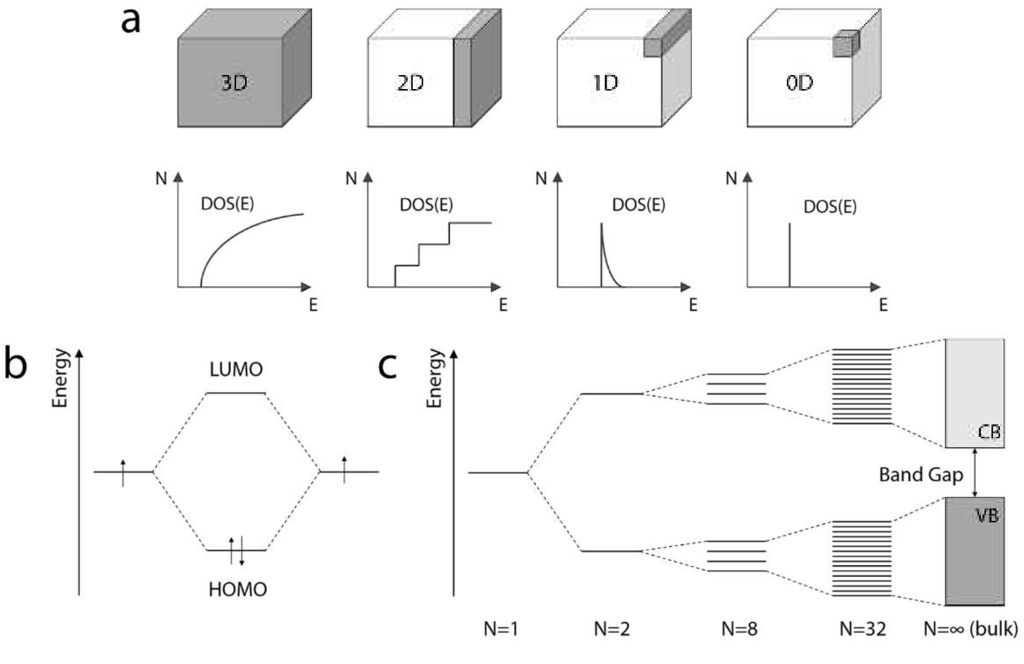

**Figure 1.1.** When the size of the material is reduced to the nanometer scale, the DOS of the material changes. Passing from the bulk 3D material to the 0D, the energy levels experience a severe discretization (*a*). The effect of the size on the electronic properties of the materials can be understood in view of the LCAO theory (*b*). When the number of atoms (N) of which the cluster is composed increases, HOMO and LUMO get closer and the energy levels become more closely spaced, eventually merging to give continuous bands (*c*).

This size-related change of the material's electronic properties is referred to as *quantum effect* and is the key to control the semiconductor properties. Specifically, QD optical properties depend directly on the energy gap, since the light (photon) emission stems from a process involving the following steps (Figure 1.2):

1- An electron (*e*$^-$) is promoted from the VB to the CB via the absorption of energy, leaving a positively charged hole (*h*$^+$) in the VB. In this way, an *e*$^-$-*h*$^+$ pair is generated. One approach to provide energy to the material is to shine light on it (*photo-excitation*): if the energy of the photon matches at least the energy gap value, the electrons of the material can absorb it.
2- The electron in the CB recombines with a hole in the VB, leading to the emission of a photon whose energy depends on the width of the energy gap itself.

The electron promotion can be obtained also using radiation whose energy is slightly smaller than that of the actual bandgap. This is the case of the formation of an *exciton*, that is an *e*$^-$-*h*$^+$ pair which behaves like a single entity. The favorable Coulombic interaction between the two oppositely charged carriers of this quasi-particle lowers the energy needed to excite the electrons from the VB. Both *e*$^-$ and *h*$^+$ are in bound states, respectively slightly below the CB and above the VB. If radiation of higher energy is used to excite the electrons, these are promoted directly to the CB and the absorption spectrum follows the profile of the DOS, giving rise to a continuous absorption profile.

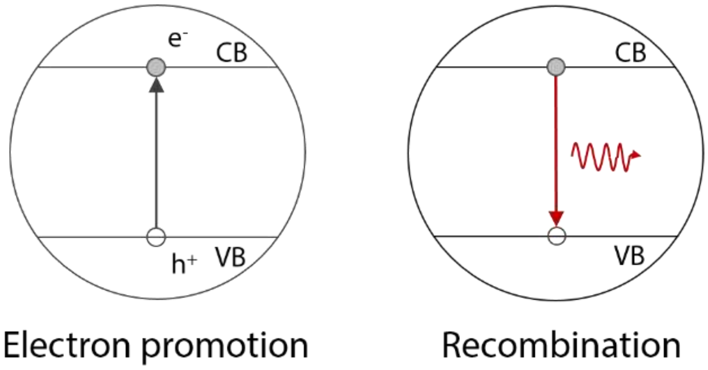

**Figure 1.2.** The usual emission mechanism in a QD consists of the promotion of an electron – black arrow - from the VB to the CB to give a *e*$^-$-*h*$^+$ pair. The electron then recombines with the hole – red arrow - releasing a photon whose energy depends on the bandgap of the QD.

The arrangement of the electronic bands is a characteristic of the material itself. We can divide semiconductors in two categories: *direct* and *indirect bandgap* semiconductors. This differentiation is based on the relative position of VB and CB in the momentum (k) space, *i.e.* the reciprocal space (Figure 3)[4]. When the VB maximum is located in correspondence of the CB minimum (*direct bandgap*), we are in the most favorable situation in order to observe an electronic transition among bands. In this configuration, the transition can take place without the involvement of lattice vibrations (*phonons*). Instead, the phonons have a major role in *indirect transitions*, since the electron has to transfer excess momentum to the crystal lattice. Thus, in direct bandgap QDs, the probability of radiative transition is higher and this translates to a higher photoluminescence quantum yield (PLQY) of these systems.

An intrinsic property of every semiconductor material is the *exciton Bohr radius* ($a_b^*$).

$$a_b^* = \varepsilon_r \left(\frac{m_e}{\mu}\right) a_b \qquad \text{where} \qquad \mu = \frac{m_e m_h}{m_e + m_h} \tag{1.1}$$

where $a_b$ is the Bohr radius (0.053 nm), $\varepsilon_r$ is the relative dielectric permittivity, $m_e$ is the electron mass, and $\mu$ is the reduced mass obtained from the free electron ($m_e$) and hole ($m_h$) mass[3]. When the QD radius is smaller than the corresponding exciton Bohr radius, the QD is in a *strong confinement regime*. This is a state where the energy levels follow the description of the particle-in-a-box model, since the size of the charge carrier wave function is comparable to the size of the box/dot. On the contrary, larger QDs are in a *weak confinement regime*.

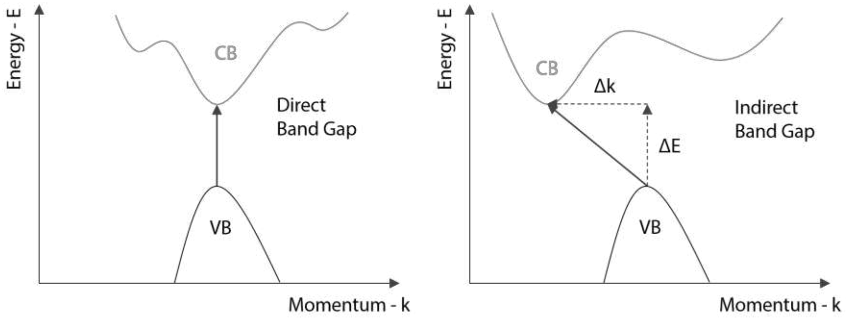

**Figure 1.3.** Direct and indirect bandgap configurations in semiconductors. In a direct bandgap semiconductor an electronic transition – black solid arrow - can take place with the sole absorption of external energy, since the top of the VB is in correspondence of the bottom of the CB. In an indirect bandgap semiconductor, also the lattice vibrations are involved in the electronic transition: the electron absorbs the external energy (ΔE) and transfer to the lattice the excess momentum (Δk).

In confined structures hole and electron wave functions have a good overlap and the exciton has an extended lifetime. Oppositely, in bulk semiconductors the exciton is not confined in space and can dissociate, thus increasing the probability of non-radiative de-excitation events such as electron trapping in defect or surface states[5]. These events are competitive with the radiative decay, so they are responsible for the emission quenching.

### 1.1.2 Tailoring QD optical properties

**Size control.** One of the easiest way to control QD optical properties is to tune their size. According to the quantum effect, larger QDs will display a red-shifted emission with respect to that of smaller QDs. However, when we approach the exciton Bohr radius, the confinement starts becoming less effective and the PLQY of the QDs drops. On the other hand, very small QDs are colloidally unstable and have a large surface-to-volume ratio, increasing the chances of non-radiative recombination (electron trapping in surface states, phonon-assisted de-excitation via interaction with molecules, etc.). Because of the limitations of this approach, researchers have developed subsidiary methods that allow for a more efficient control over QD optical features.

**Shell growth.** One common approach to increase QD PLQY is the growth of a shell of a suitable material to produce a so-called core/shell structure[6]. The choice of the shell material stems from two considerations. First, the lattice mismatch between core and shell crystalline structure has to be as small as possible, in order to facilitate the epitaxial growth of the passivating layer onto the active parent QDs. Second and most importantly, in order to obtain the desired optical properties, it is necessary to take into account the relative position of core and shell electronic bands. It is possible to realize four band alignments, depending on the desired final core/shell structure optical properties (Figure 1.4a). In Type I alignment the shell material has a wider bandgap with respect to that of the core. Therefore, the shell has a triple effect: it saturates the superficial dangling bonds (potential trap states), protects the QD core from the interaction with species in the surrounding environment, and it confines the excitons in the core. For these reasons, this configuration lowers the probability of non-radiative decays, thus greatly increasing the PLQY. A further effect of the realization of a Type I alignment is a red-shifted QD emission, which comes from a partial leakage of the excitons in the shell material. This last observation is strictly true only when no cation exchange takes place during the shell growth.

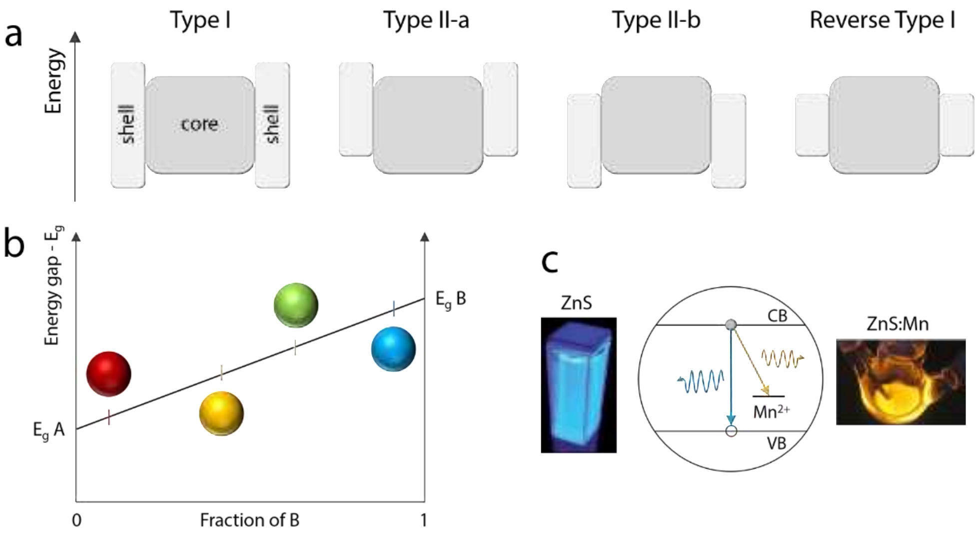

**Figure 1.4.** In a core/shell QD the alignment of the electronic bands can be of four types (*a*). The boxes represent the bandgaps of the core (dark grey) and shell (light grey) respectively, thus the position of the VB top and CB bottom. In the alloying strategy, the bandgap of the QD can be controlled varying the relative content of A and B semiconductor (*b*). In order to tailor the QD optical properties, it is also possible to dope the dot using selected elements that give rise to inter-bandgap levels, as it is the case of Mn$^{2+}$-doped ZnS (*c*). Images in *c* reproduced from Ref. [11] (ZnS) and Ref. [12] (ZnS:Mn)

We will encounter a different situation in the continuation of the discussion[7-10]. The reverse Type I alignment works in a similar way, but the charge carriers become confined in the shell, due to the favorable energetic situation in this region, so the emission is mainly governed by the shell thickness. In Type II-a and Type II-b configuration holes or electrons respectively leak in the shell, leaving the other charge carrier in the hole. In this configuration the recombination takes place at the interface of core and shell and it gives rise to a markedly red-shifted emission with respect to the one of the core.

**Alloying.** Another method to control QD optical properties relies on the production of alloyed semiconductors. Using two semiconducting materials (A and B) with different bandgaps, it is thus possible to create a library of QDs whose bandgap varies between the two extremes of pure A and pure B (Figure 1.4b)[13, 14].

**Doping.** It is also possible to introduce some ionic impurities in the QD lattice. These species bring along inter-bandgap energy levels that modify the electronic transitions. For instance, manganese creates an additional level in the ZnS QD bandgap, moving the usually intense blue luminescence of these QDs to orange (Figure 1.4c)[12].

## 1.2 Copper Indium Sulfide (CIS) QDs

In the following sections, I will illustrate the state of the art of CIS QD research. I will briefly describe the properties of the bulk material and more extensively review the studies conducted on QDs. Then, I will summarize the synthetic approaches proposed to synthesize these I-III-$VI_2$ type QDs and the strategies explored to control their features. I will also emphasize the versatility of these QDs enumerating the different applications they have been tested for, spanning from photovoltaic, photocatalysis, to biomedicine.

### 1.2.1 Properties of bulk $CuInS_2$

Copper indium sulfide (CIS) is a ternary semiconductor belonging to the I-III-$VI_2$ family, with a direct bandgap of around 1.50 eV (approximately 830 nm) and an exciton Bohr radius of 4.1 nm [15-19]. This material has attracted great interest in the past few years in the field of photovoltaic (PV) devices due to its good match with the solar spectrum, which allows for an efficient harvesting of the solar light[20]. Furthermore, bulk CIS absorption coefficient has a high value of $5 \cdot 10^5$ $cm^{-1}$, an order of magnitude higher than that of bulk CdSe[21]. Although $CuInS_2$ itself is an outstanding light harvesting material, it is possible to further improve the absorption properties of this material by synthesizing $Cu(In,Ga)(S,Se)_2$ alloys[22, 23]. All these characteristics make CIS one of the best materials for PV applications. In particular, theoretical calculations have pointed out the possibility of obtaining energy conversion efficiencies as high as 32%[24], whereas the highest efficiency reported in the literature obtained with this material is around 20%[25].

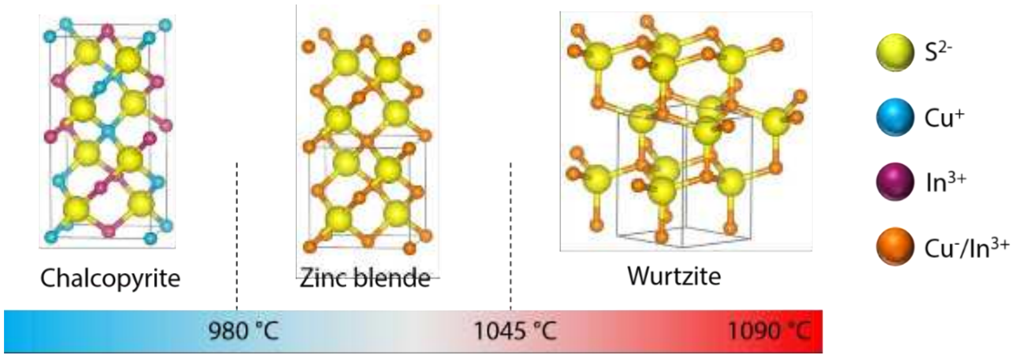

**Figure 1.5.** Bulk CIS crystallizes in three different polymorphs. Chalcopyrite (tetragonal) is stable up to 980 °C, temperature at which zinc blende (cubic) becomes the stable polymorph. This phase is retained up to 1045 °C. Wurtzite (hexagonal) appears only at temperatures close to the melting point of CIS (1090 °C). In chalcopyrite, $Cu^+$ and $In^{3+}$ occupy fixed positions in the cationic sublattice, while they are randomly distributed over the available sites in zinc blende and wurtzite.

Another important feature of CIS, is the absence of potentially toxic metal ions, such as cadmium, lead, and mercury ("the usual suspects" when talking about QDs and semiconductors in general), which are highly poisonous if released in the environment or when they accumulate in the organism. From a structural point of view, CIS crystallizes in three polymorphs: chalcopyrite (tetragonal, *I*-42*d*), zinc blende (cubic, *F*-43*m*), and wurtzite (hexagonal, *P*63*mc*) (Figure 1.5). Chalcopyrite is the thermodynamically stable polymorph at room temperature, and it is characterized by an ordered distribution of $Cu^+$ and $In^{3+}$ ions in the cation sublattice. Oppositely, in zinc blende and wurtzite, $Cu^+$ and $In^{3+}$ occupy randomly the cationic sites[26, 27]. These polymorphs also have different optical properties, as we will see in the following of the discussion.

### 1.2.2 Optical properties of CIS QDs

**General optical features of CIS QDs.** CIS QDs display four important characteristics, which distinguish them from binary QDs (Figure 1.6). First, the absorption spectrum does not show sharp excitonic features. Second, the Stokes shift (*i.e.* the separation between the excitonic absorption and emission maximum) is much larger than the one observed in binary QDs. Third, the PL emission is broad, with a profile full-width half-maximum (FWHM) of 100 nm or more[28-30]. Last, the PL lifetime (LT) is on the order of hundreds of nanoseconds. Despite these distinctive differences, the optical properties of CIS QDs still obey the quantum effect as any other QDs.

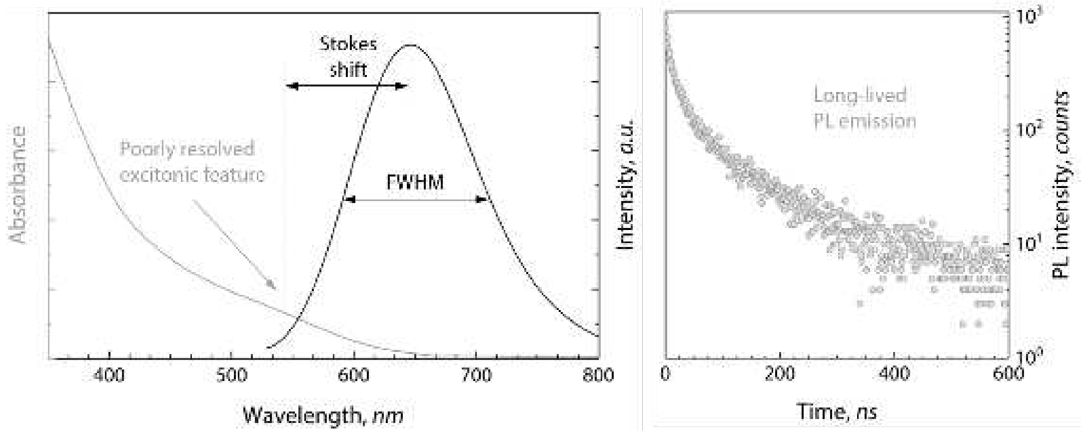

**Figure 1.6.** A usually poorly resolved excitonic feature characterizes the absorption spectrum of CIS QDs. The PL emission shows Stokes shift and FWHM both larger than 100 nm. The PL decay has a distinctive LT of hundreds of nanoseconds, due to the non-excitonic nature of the emission.

Indeed, it is possible to synthesize core-only CIS QDs of different sizes that can emit light from yellow up to the near-infra red (NIR) region. Many groups have tried to explain the unique optical features of these QDs and, at the time of the writing of this thesis, new studies have just shed more light on the mechanisms that govern the optical behavior of CIS QDs. Here also these last discoveries will be presented.

**Bulk studies.** The in-depth study of the optical properties of bulk CIS dates back to the beginning of the 1980s with Binsma, Giling, and Bloem [31, 32] and bloomed in the following years. In this material, the direct excitonic emission is hardly observed at room temperature even in single crystals [33] and most of the effort was put in elucidating the nature of the broad low energy PL bandsr[34-36]. So, excluding the emissions coming from free ($FE_A$ and $FE_B$) and bound (EX1-6) excitons to the doubly split VB, the rest of the bands were assigned to transitions involving donor and/or acceptor intra-band levels[37]. For the sake of the comparison with the behavior of CIS QDs, the bulk CIS optical features we are interested in are the broad bands appearing in the region right below that of the excitonic emission, *i.e.* between 1.50 eV and 1.30 eV. The recognized electronic transitions responsible for these bands are donor-acceptor pair (DAP) recombinations. With the term DAP we refer to oppositely charged point defects in crystals that provide an ideal recombination pathway for electrons and holes, and their energetic levels are localized in the bandgap of the material (Figure 1.7)[38]. As we will see, this attribution has influenced the interpretation of CIS QD optical properties.

**First studies on QDs.** Castro et al. were the first to investigate the nature of CIS QD emission [39]. They ascribed the particular profile of the absorption and emission spectra of the QDs to a sum of causes, which are often responsible for broad PL spectra in QDs: broad size distribution, leakage of the exciton in the organic ligand layer, and presence of intra-bandgap states. They ruled out the first two causes, concluding that the QD optical properties are understandable considering a DAP recombination mechanism. This interpretation was supported for a long time also by other groups [9, 28, 30, 40-44] in light of some experimental evidences: the impossibility of narrowing the PL emission profile via size sorting, the large Stokes shift and long LTs (hundreds of nanoseconds). Indeed, while LTs of few nanoseconds are characteristic of an excitonic emission, this long-lived PL signal is a marked characteristic of DAP-related emission. As aforementioned, the QD size has an effect on both the absorption and emission properties.

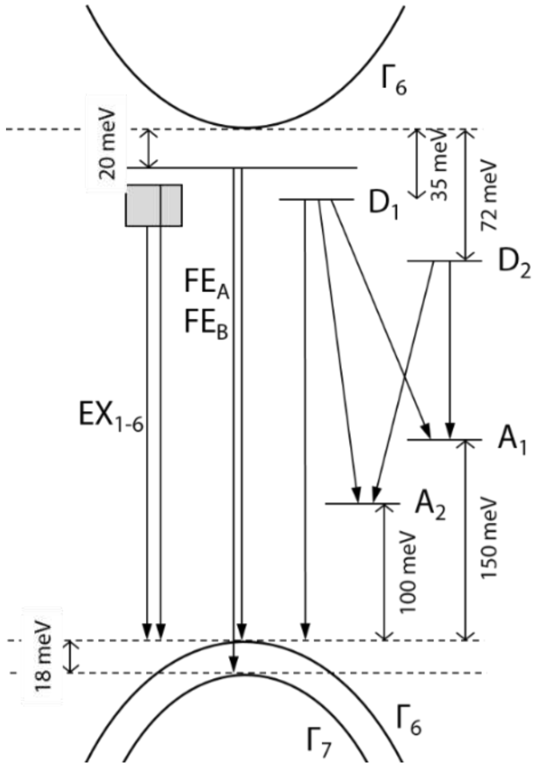

**Figure 1.7.** In this sketch, the electronic levels involved in CIS radiative transitions at the center of the first Brillouin zone (Γ) are summarized. Excitonic emissions stem from free excitons (where the electron is in a relaxed level 20 meV below the CB – $FE_{A,B}$) or bound excitons (excitons bound to crystal defects, thus with a lower energy – $EX_{1-6}$). Non-excitonic transitions take place with the involvement of donor and acceptor levels. In particular donor levels are assigned to: $D_1$ – sulfur vacancy ($V_S$) and $D_2$ – interstitial indium ($In_i$). Acceptor levels vary from the case of In-rich ($A_1$) and Cu-rich ($A_2$) CIS, and they are attributed respectively to $A_1$ – copper vacancy ($V_{Cu}$) and $A_2$ – indium vacancy ($V_{In}$) or substitutional copper ($Cu_{In}$)

To account for this effect, different groups have tried to identify the states more likely involved in the radiative electronic transitions, trying to describe their relative position with respect to VB and CB. According to these first studies, sulfur vacancies ($V_S$) and copper vacancies ($V_{Cu}$) were playing a major role [17, 29]. Moreover, the experimental evidence that copper-deficient QDs exhibit higher PLQY, wider bandgap, and a blue-shifted emission peak[45, 46] were further corroborating the involvement of $V_{Cu}$ levels. In particular, Chen et al. [45] conducted a thorough study about the effect of deviations from the Cu:In=1:1 molecularity. Actually, in these systems, the term *stoichiometry* refers to the sulfur-to-copper ratio and *molecularity* to the copper-to-indium ratio[32], which is the parameter playing the major role in the control of CIS QD optical properties. The group explained the properties of copper-deficient QDs suggesting a lowering of the VB with decreasing copper content that stemmed from the mixed nature of the top of this band, due to the hybridization between Cu *d* and S *p* orbitals.

**Time resolved studies.** Although the large number of studies reported about CIS QDs and the experimental evidences supporting the assignment of the emission to DAP-related processes, recent studies have steered the attention towards other electronic mechanisms. Several groups performed time-resolved photoluminescence (TRPL) studies obtaining contradictory conclusions. Tran [44] observed that the TRPL signals of core/shell CIS/ZnS QDs could be deconvolved using two components, respectively of the order of magnitude of tens and hundreds of nanoseconds. They attributed the emission to DAP recombination processes, since the PL peak position was dependent upon the delay of the excitation pulse: indeed distant DAP transitions become more frequent with increasing delay time, since they possess lower transition probabilities and energies[38]. In 2013 Cichy et al. [47] investigated the emission of CIS QDs of different size, observing that the multi-exponential decay behavior of the QDs can be conveniently simulated using a distribution of decay rates. They observed a strong dependence of the decay times from the QD dimension, postulating a competitive recombination of carriers from higher exciton excited states as the more probable mechanism. They justified this assumption observing that DAP recombination should not play a major role in small semiconductor nanocrystals, where strong confinement regime is dominant[47]. Later, Omata et al. compared the experimental PL data with theoretical models[48]. They concluded that the main radiative transition takes place from a substitutional indium level ($In_{Cu}$), positioned approximately 0.1 eV below the CB, to a bound VB state 1S(h). Cadirci et al. used a pump-probe technique to analyze the transmittance of 2 and 3 nm CIS QDs[49]. They concluded that *trion* formation was the main mechanism underneath the decay of fractional transmittance, and the hole trapping as the main bleaching process. Sun et al. used transient absorption (TA) analysis to characterize CIS/ZnS QDs and observed one bleaching and one photo-induced absorption feature[50]. The bound 1S(e) states in the CB are the carrier reservoir from where the transition takes place to a localized $h^+$ state. The DAP recombination mechanism was discarded by the group, due to the relatively high PLQY observed in the system, for which the aforementioned process cannot account for. The results of this study are in accordance also with those of Cadirci where the authors pointed out hole trapping as a fundamental process[49]. Similarly, Kraatz et al. published a well-conducted study of the behavior of CIS/ZnS QDs under pump-dump-probe conditions[51]. The group observed three optical density variations in TA spectra, respectively ascribed to ground state absorption, stimulated emission, and excited state absorption. The most likely emission mechanism resulted to be an electronic transition from a sub-bandgap state to the VB or a trap level just above the VB. They identified the sub-bandgap level as $In_{Cu}$. The group claimed that the involvement of $V_S$ is irrelevant in a fully passivated CIS/ZnS QD, since these defects are localized mainly on the QD surface.

**Magneto-optical studies.** Two recent studies have proven fundamental in providing a more accurate description of the radiative electronic transitions in CIS QDs[52, 53]. These works compared the similar emission displayed by CIS QDs and Cu-doped binary QDs. Exploiting the paramagnetic behavior of $Cu^{2+}$, the researchers conducted magneto-optical analysis to compare the PL emission of the different QDs. They observed the same behavior in both families of particles, concluding that also in ternary chalcogenide QDs the emission stems from the recombination of an electron delocalized in the CB with a hole trapped in a $Cu^{+}/Cu^{2+}$ level (Figure 1.8). This mechanism is currently the *consensus* for the description of radiative electronic transitions in CIS QDs.

**Single-particle studies.** Witham et al. were the first to report on single-particle spectroscopy on CIS/CdS QDs[54]. They observed severe blinking (*i.e.* severe PL intermittence) at the single particle level, and confirmed the characteristic broadness of CIS QD PL emission. They justified this observation invoking a strong electron-phonon coupling in the excited states. However, in 2017 Klimov's group published a thorough study on CIS/ZnS giant core/shell QDs[55]. Using a very thick shell, they were able to suppress the blinking and they successfully measured single particle spectra. For the first time, the results showed that single particle emission profile is as narrow as 60 meV (compared to more than 300 meV for the ensemble) and the group showed that the broadness of the PL signal in CIS QDs stems from the heterogeneity in the sample. The difference of optical behavior from dot to dot has two sources: size inhomogeneity and random variations in the physical position of the emissive defect within the QDs. The nature of these recombination centers is still not completely clear, but the authors agree in considering them to be Cu-related.

As we can judge from this (not so) brief summary on the studies of CIS QD optical properties, this is a still very lively research field and further studies are expected to give an even more accurate description of the system.

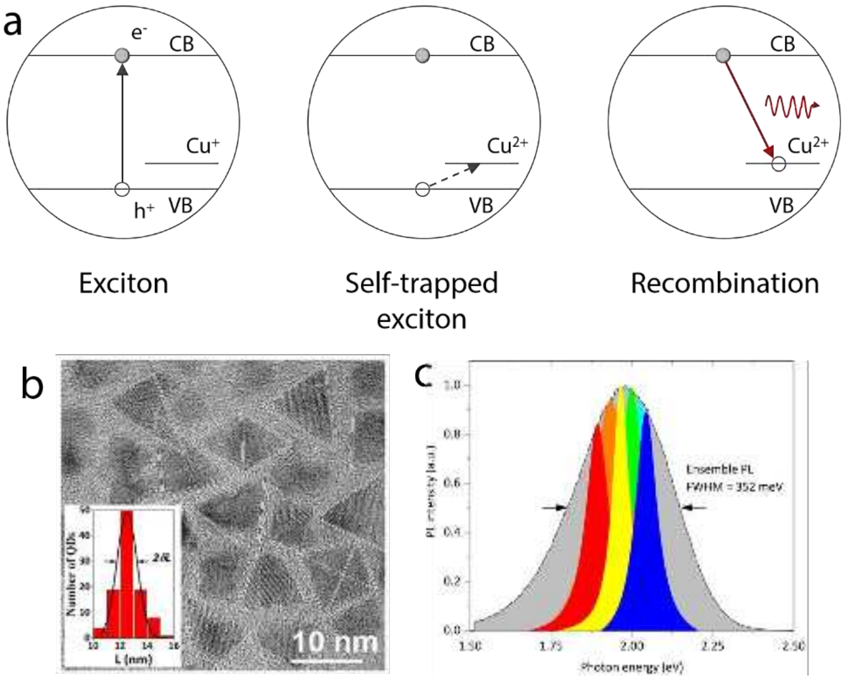

**Figure 1.8.** The emission in CIS QDs stems from a three step process (*a*). After the electron promotion to the CB (exciton formation), the delocalized hole in the VB get trapped in a $Cu^+$ acceptor state to give a $Cu^{2+}$-like state. The electron eventually recombines with the localized hole releasing energy as light. In the recent study by Klimov, thick shell CIS/ZnS QDs were produced (*b*) in order to suppress blinking phenomena and perform single-particle spectroscopy. The results show that the linewidth of the single particle emission is much narrower than that of the whole sample (60 meV *vs.* 305 meV) and the position of the single QD PL peak depends mainly on the size of the dot (*c*). *b* and *c* reproduced from Ref. [55].

### 1.2.3 Synthesis of CIS QDs

The preparation of CIS QDs can be accomplished via different approaches, such as thermal decomposition[17, 29, 41, 42, 56, 57], hydro/solvothermal[58-61], polyol route[62-64], microwave-assisted[65-67], sono-chemical[68], photolysis[69], and precipitation from solution[70]. However, the most exploited synthetic method is the thermal decomposition, either in its one-pot (heat up) or in the hot injection version. This approach consists in the breakdown of metal-organic precursors at high temperature (200 – 250 °C) in high boiling point solvents, such as 1-octadecene (ODE). This is a reproducible approach, which gives high quality QDs. For this reason, most of the next considerations will pertain to thermal decomposition. When synthesizing CIS QDs, changes in the reaction parameters can lead to significantly different results in terms of structural and physical properties of the final product. Paramount reaction parameters in order to grow high quality QDs are temperature, time, ligands, solvent and precursors. Moreover, the strategies mentioned in Section 1.1.1, such as alloying and shell growth, can be used to tailor the optical properties of CIS QDs.

**Ligands.** The choice of ligand molecules (*i.e.* capping agents) is the pivotal parameter in the synthesis of CIS QDs. It is not straightforward to generalize the data in the literature, due the diversity of the synthetic methods and the large variety of ligands tested. Moreover, the solvent itself can have coordinating properties, and it further interferes with the reaction process. The ligands have the fundamental role of creating metal-organic complexes and controlling reactivity of the ions during the QD growth. This kinetic control exerted by the ligands allow for the synthesis of QDs with a reduced amount of trap states in the lattice, *i.e.* a higher PLQY. Moreover, the ligand molecules attached on the surface of the QDs endow them with colloidal stability in the desired environment. Xie et al. observed that the simultaneous presence of capping agents with hard and soft Lewis base behavior (*e.g.* fatty acids and alkyl thiols respectively) allows for a fine control over the reactivity of the metal ions in the solution[71]. This is because indium and copper are respectively hard and soft Lewis acids. However, even when only alkyl thiols are present in the reaction environment, indium reactivity could still be controlled by introducing a large excess of ligand molecules[28, 72].

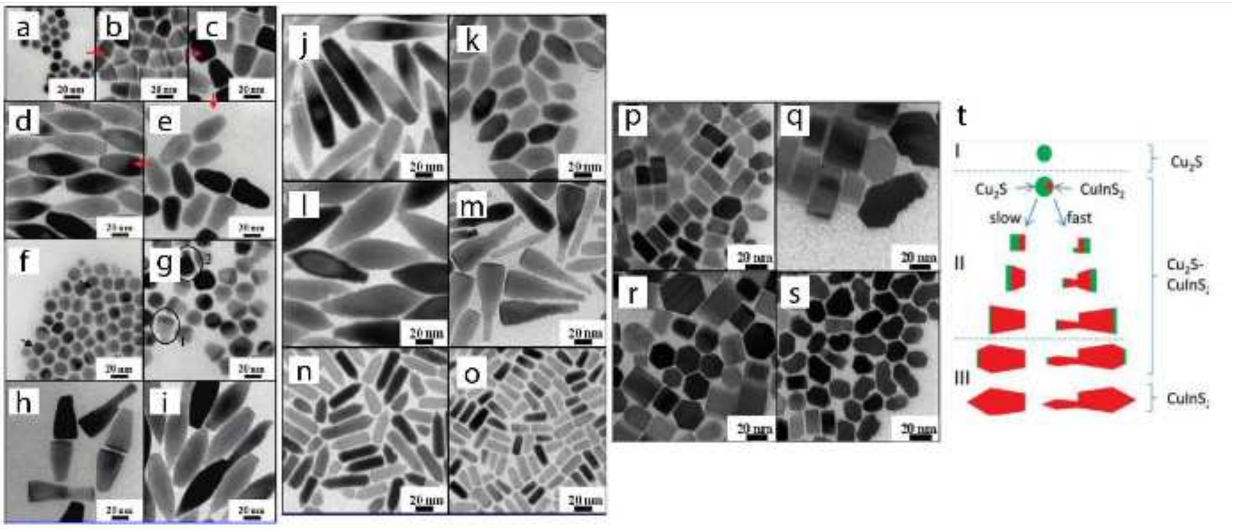

**Figure 1.9.** In this image we can observe the degree of complexity of the morphology that can be obtained varying the reaction parameters. Variations of parameters like reaction time and precursor ratio (*a*-*i*), TOP and DDT amount (*j*-*o*), and type of phosphonic acid (*p*-*s*) lead to very different morphologies, since they determine the growth kinetics (*t*). Reproduced from Ref. [26]

Chang et al.[73] observed that the phase of the nanocrystals produced in the presence of 1-octadecene (ODE), oleic acid (OA), and 1-dodecanethiol (DDT) is influenced by the solvent-to-ligand ratio. In particular, the fine kinetic control of the reaction allows for the production of thermodynamically unstable phases, such as wurtzite. Beautiful flower-like and nano-pompoms structures can be obtained by introducing surfactants in the reaction mixture, such as polyvinylpirrolidone (PVP) and cetyltrimethyl ammonium (CTAB)[74]. In 2012 Deng et al. published a well-conducted study on the synthesis of CIS/ZnS QDs and focused on the effects of the synthetic parameters on the luminescent properties of QDs[17]. They found that the amount of DDT plays a fundamental role in the production of QDs with high PLQY, with a minor effect over the position of the emission band. Niezgoda et al. managed to control the reactivity of the metal ions to obtain spherical QDs, exploiting the capping capabilities of phosphorous-containing ligands, namely tri-octylphosphine oxide (TOPO) and dodecyl phosphonic acid (DDPA), along with those of 1-hexadecyl amine (HAD)[75]. He et al. discovered that the ligand molecules $Sn(acac)_2Cl_2$ has a critical role in determining the size and shape of the product, the morphology of the QDs passing from polydisperse flute-like to almost monodisperse polygonal[76]. Kazuya et al. investigated the effect of various solvents and/or ligands on the morphology and structure of the QDs[77]. They showed that ligands with different coordinating capabilities lead to different polymorphs and that the preferred formation of one phase instead of another is strongly related to the structure of the initial $Cu_{2-x}S$ nuclei. These pre-generated copper sulfide species are the seeds over which CIS QDs grow thanks to cation exchange and diffusion of $In^{3+}$ in place of $Cu^{+}$. Similarly, this intermediate $Cu_{2-x}S$ state was observed by Kruszynska et al., who were able to grow an incredible variety of CIS and CIS/ZnS morphologies changing the type and amount of ligand molecules in the reaction environment[26] (Figure 1.9). This marked effect of the ligand molecules is observed also for different synthetic methods. For example, Liu et al. ascertained that the concentration of 3-mercaptopropionic acid (MPA) in the aqueous reaction environment is fundamental in determining the optical properties and the colloidal stability of the obtained QDs[58].

**Time and temperature.** Copper and indium precursors used in most synthetic approaches are only slightly soluble at room temperature in high boiling point solvents, even in the presence of suitable ligands. For this reason, usually the first step of these reactions is the maintenance of a temperature above 100 °C for some minutes, in order to allow the dissolution of the precursors and the homogenization of the solution. In the heat up approach, the synthesis is conducted at temperatures above 200 °C[77] and the reaction mixture is kept at this temperature (generally for 0.5 to 10 h) to promote the decomposition of sulfur-containing metal-organic precursors and the growth of the dots. In the hot injection version, the temperature at which the sulfur solution is swiftly introduced in the reaction environment is usually lower than that used in heat up processes (*i.e.* below 200 °C), and the reaction time is shorter (usually up to 30 min). Generally, the fast burst of nucleation ensures a less polydisperse sample, but batch-to-batch differences are more pronounced due to the presence of the critical injection step (differences in the operator *modus operandi* and variability in the fast injection rate). In a general way, the longer the reaction time the bigger the produced QDs, *i.e.* their bandgap is wider and their PL emission peak progressively red-shifts. An increase of the reaction temperature has a similar effect. Nonetheless, with too long times the reaction enters the Ostwald ripening regime, which eventually might lead to the aggregation of the QDs. The use of too high temperature determines an uncontrolled growth of highly defective QDs, but at low temperatures the QD crystallinity might be poor [29]. Moreover, at temperatures below 160 °C copper sulfide is present as unavoidable impurity [57]. To conclude, both the choice of reaction time and temperature is critical to obtain well crystallized and stable QDs, whose size has to be kept desirably below 8.2 nm (since the exciton Borh radius is 4.1 nm) in order to have good optical properties.

**Precursor ratio.** As mentioned in Section 1.2.2, copper-deficient CIS QDs have different optical properties than stoichiometric QDs. According to a number of studies[45, 46, 78], samples where copper vacancies are intentionally introduced show higher PLQY values (Figure 1.10a and 1.10b). These improved performances are accompanied by a blue-shift of both absorption and emission, an effect explained as a consequence of the copper and sulfur orbital hybridization[29, 30]. It has to be noted that the optimal copper-to-indium ratio depends on the synthetic method, since the reactivity of each cation is strongly dependent upon the species (namely the ligand molecules) present in the reaction environment. For this reason, the actual molecularity of the sample can heavily differ from the nominal amount of precursors in the reaction environment[78].

**Alloying.** The alloying of $CuInS_2$ with other metal chalcogenides is a strategy often exploited to tune the optical properties of CIS QDs. For instance, alloyed CIS-ZnS QDs can be synthesized to effectively cover the broad blue to NIR spectral range[79, 80] (Figure 1.10c). Other materials CIS can be alloyed with are $CuGaS_2$ ($E_g$ = 2.43 eV) and $CuInSe_2$ ($E_g$ = 1.70 eV).

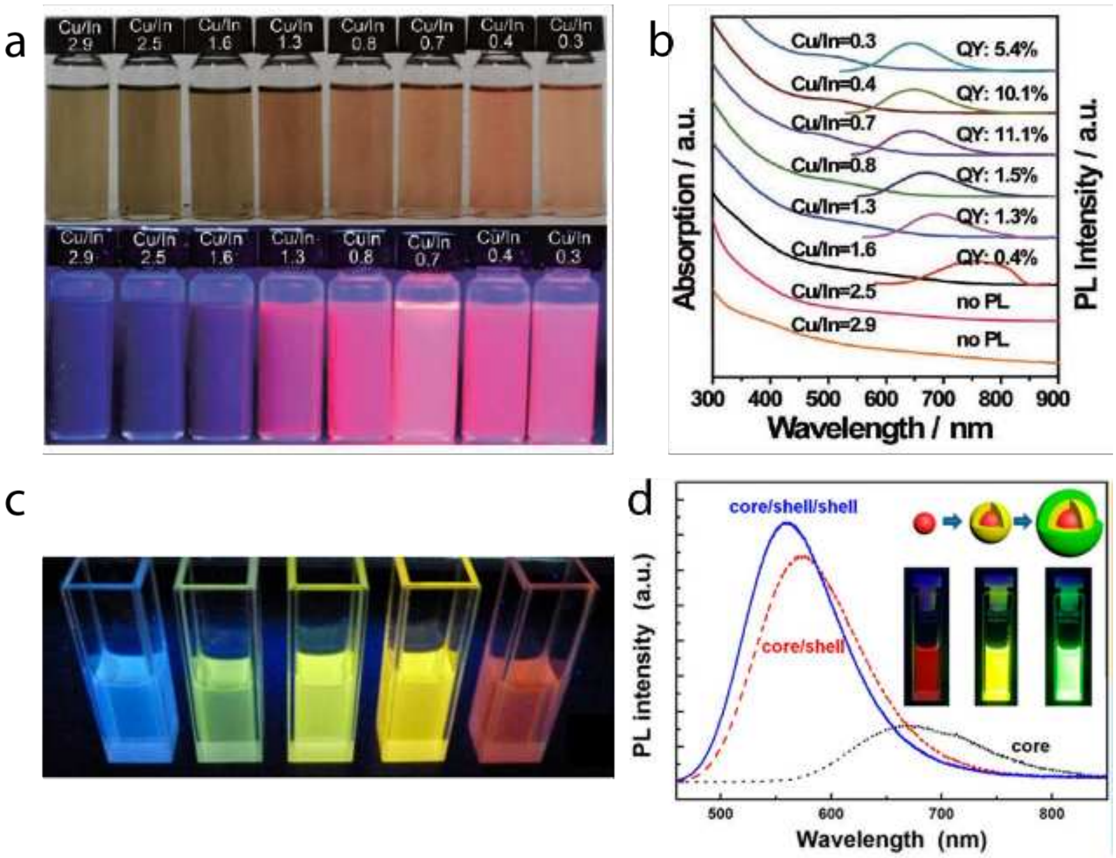

**Figure 1.10.** An intentional introduction of a controlled amount of copper vacancies in CIS QDs leads to improved optical properties (*a*, *b* – reproduced from Ref. [45]). The alloying strategy with ZnS is a reliable approach to obtain QDs whose emission covers the blue to NIR range (*c* - reproduced from Ref.[72]). The growth of a ZnS shell on core CIS QDs has the double effect of increasing the PLQY and blue-shifting the emission (*d* - reproduced from Ref.[82]). This last effect is more or less pronounced depending on the reaction conditions.

---

The alloying with the former allows covering effectively the visible range[81], instead the partial substitution of sulfur with selenium gives a fine tunability of the emission in the NIR region[14]. With this strategy, it is possible to tailor the emission of the QDs simply varying the ratio between the metal precursors while keeping fixed other already optimized synthetic parameters which are more critical to control (such as temperature and time). In this way, the QD size is kept almost constant throughout the different batches, avoiding the issues related to small and large size.

**Shell growth.** The best strategy to obtain an increased PLQY is the growth of a passivating shell[17, 42]. The only configuration obtained so far for these QDs is a Type-I band alignment using ZnS ($E_g$ = 3.54 eV) and CdS ($E_g$ = 2.42 eV). Although a CdS shell imparts the best optical performances[42], ZnS allows obtaining almost equally performing QDs maintaining the heavy metal-free nature of the material[17]. ZnS is chemically stable and has a large bandgap; furthermore it has a small lattice mismatch of 2 - 3 % with respect to the core crystalline structure (considering the CIS chalcopyrite and ZnS wurzite structures, respectively)[9, 56]. After the growth of a ZnS shell, the PLQY increases considerably (reaching values as high as 80 %) and the PL emission peak blue-shifts[83, 84] (Figure 1.10d). This last effect likely stems from: *a)* the core shrinkage caused by the cation exchange ($Zn^{2+}$ in place of $In^{3+}$ and $Cu^+$) and *b)* formation of a $CuInS_2$-ZnS alloyed layer between the core and the shell[10, 29, 85, 86]. This explanation is supported by the work of Booth et al., where the authors better fitted CIS/ZnS QD diffractograms using a Cu-In-Zn-S single phase instead of two $CuInS_2$ and ZnS phases[21]. X-ray photoelectron spectroscopy (XPS) analysis provided further evidences for the substitution of $Zn^{2+}$ in place of $Cu^{+}$[29]. Although more studies are needed to assess the actual core/shell structure of CIS/ZnS QDs, it is indisputable that this approach leads to a drastic improvement of the PL properties of the dots, which is accompanied by a blue shift of the emission.

**Surface modification.** As mentioned above, high quality QDs are usually synthesized in non-polar organic solvents. This might be an issue when applications in hydrophilic environments are foreseen, such as in the biomedical field. To obtain water-dispersible QDs, reactions exploiting a hydrophilic environment have been designed[58] and numerous aqueous transfer procedures have been proposed. To turn hydrophobic QDs into hydrophilic colloids, it is possible to employ ligand exchange[87], encapsulation in micelles[17, 56], coating with polymers[88], and encapsulation in silica[57, 89]. All these methods are quite general, and apply to most hydrophobic NPs. For instance, CIS QDs have been coated with polylactic glycolic acid–polyethylene glycol (PLGA-PEG) co-polymer[90], modified poly(maleic anhydride-alt-1-octadecene) (PMAO) polymer[85, 88, 91, 92], polyethylene glycol-methyl acrylate (PEGMA)[93], 6-armed N-hydroxysuccinimide (NHS)-functionalized PEG[94], [1,2-diacyl-sn-glycero-3-phosphoethanolamineN-methoxy(polyethylene glycol)] (DSPE-mPEG)[95], albumin[96], chitosan[17], and trimethyl(tetradecyl)ammonium bromide (TTAB)[97]. Often ligand exchange results difficult in these QDs, due to the high affinity of DDT (used in most of the oil-based synthesis of CIS QDs) with the QD surface. However, there are reports about successful ligand exchange with mercaptopropionic acid (MPA)[97], mercaptoundecanoic acid[98], and dihydrolipoic acid-polyethylene glycol (DHLA-PEG)[43, 99]. Silica coating has the advantage of an easy surface modification with different chemical groups[89] and allows for the simultaneous incorporation of different NPs in the same entity, endowing the system with multiple capabilities (*e.g.* magnetic and luminescent - Figure 1.11)[57].

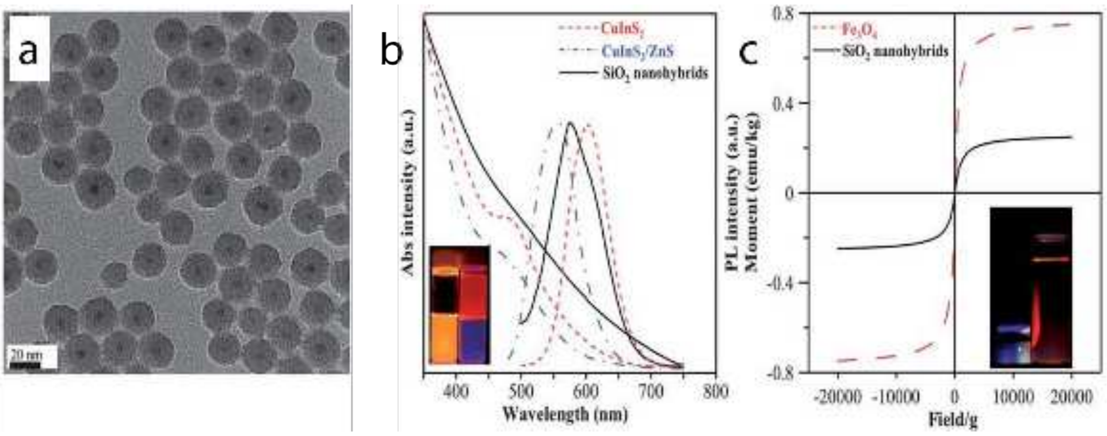

**Figure 1.11.** One of the strategies to transfer to water CIS QDs is to encapsulate them in silica. Following this approach, it is also possible to co-encapsulate other NPs. For instance, iron oxide NPs and CIS QDs can be combined in the same entity (*a*) to obtain optical (*b*) and magnetic (*c*) properties in the same system. Reproduced from Ref. [57]

Although for some applications the QD transfer to water is necessary, an unavoidable drawback of this procedure is the loss of part of the original PLQY[100]. This decrease of PL emission efficiency is due to the high energy of water phonons that effectively support non-radiative de-excitation processses[101]. In conclusion, post-synthesis QD surface modification is a crucial step in particular for the preparation of water-dispersible system. Many methods to transfer CIS QDs in water are currently available in the literature; however, they are not specific for these QDs but rather generally applicable to virtually any hydrophobic NP.

### 1.2.4 Applications of CIS QDs

**Photovoltaic.** The most studied application field for CIS-based materials is the preparation of PV devices. Thin film $Cu(In,Ga)(S,Se)_2$ solar cells have been showing increasing potential in the photovoltaic panorama, reaching record values of energy conversion as high as 20 %[22]. Instead, CIS QDs can also be used in the technology of QD-sensitized solar cells (QDSSCs) (Figure 1.12a). In this approach, QDs act as the light absorbing species where $e^-$ and $h^+$ are photo-generated. The effective charge separation is achieved thanks to the fast injection of $e^-$ in the $TiO_2$ layer (with a rate constant of $5.75\ 10^{11} s^{-1}$ [102]), which leaves free $h^+$ in the VB available for the transfer to the redox species (electrolyte). The good performances of CIS QDSSCs are guaranteed by a favorable band alignment of the QDs with $TiO_2$ (Figure 1.12a). The deposition of the QDs on the oxide can be accomplished for instance via dip coating after support modification[103], drop casting[104], successive ionic layer absorption-reaction (SILAR)[105], or electrophoretic deposition[106]. In particular, using this last approach, Santra et al. obtained a respectable power conversion efficiency of 3.9 %[106]. In the study the authors showed that the growth of a CdS layer around both $TiO_2$ and CIS QDs improved the performances of the device, by enhancing the photo response of the QDs in the red region and improving the effect of charge separation. The record efficiency reported so far for CIS-based QDSSCs has been obtained in 2014 from the group of Bisquert[107]. They immobilized MPA-capped CIS/ZnS QDs on a $TiO_2$ electrode and took advantage of the broadband absorption of the QDs to boost the efficiency of Cd and Pb free solar cells to the record efficiency of 7.04 %. This is a remarkable result in the world of "green" QDSSC, considering that the absolute record in this field is 11.6 % and has been obtained in 2016 with Zn-Cu-In-Se QDs[108].

Another PV application, in which CIS QDs have proven competitive with the state of the art materials, is that of linear solar concentrators (LSC). This technology is based on the harvesting of the solar light, its conversion to a suitable wavelength, and the concentration of this emission on a small surface. Roughly speaking, a LSC is a polymeric waveguide in which the photoactive species (QDs in this particular case) are dispersed and the design of the device allows for the concentration of the light at its edges, where the photovoltaic devices are located. A good performance of a LSC is ensured by minimal self-absorption phenomena (large Stokes shift) and a broadband emission covering good part of the solar spectrum. These are both characteristics of CIS QDs. Indeed, Meinardi et al. succeeded in the preparation of large and almost colorless LSCs using $CuIn(S,Se)_2$ QDs, which had a power efficiency conversion as high as 3.27 %[109].

This is, of course, only a very limited part of the work that has been done in the PV field using CIS QDs. Indeed, due to the incredibly large number of papers about the subject, owing to the perfectly suited properties of CIS QDs for PV applications, an accurate review of the literature is not possible in the context of this thesis.

**White Light Emitting Diodes (WLEDs).** Due to their efficient emission in the red region of the electromagnetic spectrum, CIS QDs are ideal candidates for applications in WLEDs technology. One of the most exploited method to obtain white light in LED technology is the use of a polymeric layer, in which inorganic phosphors (converters) are dispersed, that is put in front of a blue-emitting GaN or InGaN semiconductor. Phosphors of cerium-doped yttrium aluminum garnet (YAG:Ce) are the most used converters, due to the high absorption cross section of $Ce^{3+}$ in the blue region, the broadband emission covering most of the visible spectral range, and a stable PLQY of approximately 85 % even at high temperature[110]. The scattering of the part of blue emission that is not absorbed by the phosphors combined with the phosphor emission itself gives white light. Co-doping YAG with another rare-earth (RE) ion, such as $Eu^{3+}$, $Sm^{3+}$, or $Pr^{3+}$, having strong emission lines in the red region, allows for the obtaining a "warmer" white light[111, 112]. The broad emission of CIS QDs is similar to the one of YAG:Ce and makes these QDs ideal candidates for WLED production. Kim et al. first reported the use of CIS/ZnS crystals dispersed in polystyrene as a coating layer for WLEDs[113]. Nonetheless, the obtained device showed poor stability under continuous operation and a large part of the emission fell in the NIR. Later, the same group reported the incorporation of these QDs in a silicone-based polymer along with a green emitting phosphor, obtaining an high quality wavelength converter layer, with high stability under various operating currents and CIE values of (0.327, 0.312)[114]. Similarly, Yang's group synthesized a series of $Cu(In,Ga)S_2$/ZnS QDs, obtaining highly emisive QDs with a PLQY as high as 83% (Figure 1.12b)[81]. Better performances and a color rendering index (CRI) higher than 90 was obtained using at the same time YAG:Ce phosphors and CIS QDs as blue light converters[115]. Although the device showed slightly decreased luminous efficiency, the use of CIS QDs moved the CIE coordinates (0.334, 0.328) towards the pure white values (0.333, 0.333). The same approach was recently adopted by Aboulaich et al.[7]. The semiconductor chip was covered using two layers of a silicone blend: the first containing YAG:Ce phosphors and the second CIS/ZnS QDs. The authors obtained a CRI of 84, but observed a drop of the luminous efficiency. Recently, Peng et al. obtained a double emission from Zn-Cu-In-S QDs doped with $Mn^{2+}$ [116]. The combination of the blue emission of the LED and the extended QD emission allowed obtaining CIE coordinates of (0.332, 0.321) and a CRI of 90 without the use of a secondary phosphor such as YAG:Ce. The main issue in CIS QDs-based WLEDs is the stability over prolonged operating times, since all of the presented studies show a significant drop of the performances already after few hours of operations. CIS QDs could also be used as the main semiconductor component to build colored LEDs. Eventually, Chen et al. investigated Cu-Zn-In-S/ZnS QDs electroluminescent properties concluding that these particles are promising LED core materials[45].

**Biomedical.** According to Al-Ahmadi, in order to be applied in the biomedical field, a QD has to fulfill some prerequisites: *i.* thermodynamic stability, *ii.* narrow size distribution, *iii.* broad absorption spectrum, *iv.* low non-specific affinity towards biological molecules, and *v.* colloidal and chemical stability in aqueous media[117]. A major concern in this application field is the possible release and accumulation of toxic metal ions in the body. Although all the points reported by Al-Ahmadi can be addressed with the identification of a suitable synthetic method, post-synthesis purification, and surface modification, the problem related to the toxicity of the metal ions of which QDs are constituted cannot be satisfactorily overcome in compounds such as CdSe, CdS, HgS, and PbS. For this reasons, heavy metal-free QDs, such as CIS QDs, are currently under intense investigation. In 2009, Li et al. reported the first example of CIS QD application in the biological field[9]. In this study, CIS/ZnS quantum dots were produced with emission spanning from green to NIR. Water transfer was accomplished via ligand exchange of DDT with DHLA. The QDs were administered to mice via injection in the tail and the fluorescence signal was acquired at different time points for 24 h after the injection, observing only slight fading of the signal and no changes in the vital functions of the mice. The authors observed QD accumulation essentially in lungs, liver, and spleen, a common behavior of almost all the NPs when administered *in vivo*. Since this first report, a number of studies have dealt with the applications of CIS both in vivo and in vitro[79, 85, 93, 95, 99, 118]. Cassette et al. demonstrated the applicability of $CuIn(S,Se)_2$ QDs in lymph node imaging site[100]. For the same purpose dihydrolipoic acid polyehtylene glycol (DHLA-PEG1000) or dipalmitoyl phosphotidylethanolamine polyehtylene glycol (DPPE-PEG2000) stabilized QDs were used by Pons et al.[56]. In this study, the authors prepared two control batches using CdTeSe/ZnS QDs, observing the absence or a markedly reduced inflammation of the regional lymph node for CIS-based formulations in comparison with the $Cd^{2+}$-containing ones. Prasad's group further reported on the use of CIS QDs as probes for optical imaging[95]. The implementation of magnetic properties in CIS QDs-containing systems was reported as well. For instance, Hsu et al. embedded magnetite NPs and CIS QDs in silica creating a composite with both magnetic and fluorescent properties, thus applicable both as optical marker and magnetic resonance imaging (MRI) contrast agent[57]. The group also bound cis-platinum anticancer drug on the composite surface, obtaining a multimodal theranostic system. Ding et al. endowed CIS QDs themselves with magnetic properties by means of $Mn^{2+}$ incorporation in the crystalline lattice[43]. Instead, Cheng et al. produced multimodal probes attaching a magnetic Gd-complex on the QD surface. They further modified this complex with folic acid imparting to the system active tumor targeting capabilities[92]. Active targeting was also implemented in CIS QDs-containing chitosan micelles by Deng et al.[17]. The group exploited the extended QD absorption to obtain subcutaneous fluorescence imaging exciting at 766 nm and recording the signal above 800 nm (Figure 1.12d). Although the major hurdle is the possible toxicity of the QDs, only sparse information is available about this topic, with some cell viability tests conducted over some cell lines[68, 92, 97]. All of these tests seem to confirm the substantial lack or low toxicity of CIS QDs on HeLa, HepG2, and MCF-7 cells up to 100-200 µL/mL. Still, rigorous, long term, *i.e.* more than 24 h, tests should be conducted in order to assess the real impact of these nanoparticles on cells. A more complex study was made *in vivo* on *Caenorhabditis elegans*, as a model organism[119]. CIS/ZnS QDs were transferred to water with chitosan micelles, and the group tracked $Zn^{2+}$ leaching from the QDs observing a high chemical stability of the dots. Eventually, Chetty et al. investigated the nano-xenotoxicity of MUA-capped CIS/ZnS QDs in zebra fish embryos[98]. Their results confirm a lack or a modest toxicity of these systems too. It is worth mentioning that on a more general note, the toxicity of NPs is strongly dependent upon their superficial composition other than on the material itself, so it is difficult and to some extent pointless to speak about CIS QD toxicity. Instead, it is necessary to assess the toxicity of the system in its complexity case by case.

**Probes for bioassays.** Su's group has been working intensively on the application of these QDs for bioassays. In the last years the group demonstrated the possibility to efficiently detect and quantify a number of molecules using *ad hoc* modified CIS QDs and monitoring their emission as a function of the concentration of the target molecules. The group reported on the effective detection of ascorbic acid[120], dopamine[60], alkaline phosphatase[121], heparin and heparinase[122], thrombin[123], arsenate[124], anthrax lethal factor DNA[125], copper, cobalt, and cadmium[126].

**Photocatalysis (de-pollution and water splitting).** Another field in which CIS QDs have proven to be an efficient system, is photocatalysis[40, 127-129]. For instance, Zhang et al. observed a complete degradation of the model pollutant Rhodamine B (RhB) dissolved in a suspension of Cu-Zn-In-S QDs, after 2 h or irradiation with visible light[40]. Similarly, Ye et al reported the degradation of RhB exploiting nanorods of the same alloy. They achieved a remarkable result, with 90 % of the pollutant degraded just after 2 min of irradiation[129]. The best performances are obtained with composite materials, in particular in the field of hydrogen production from water (water splitting). This is the case of Cheng et al., who used a composite of $WS_2$ nanotubes, Au-NPs, and CIS QDs in hydrogen generation. The authors exploited the plasmonic effect of Au-NPs to enhance light absorption in the visible, thus increasing the performance of the system[130]. Tsuji et al. employed a solid solution of ZnS-$CuInS_2$-$AgInS_2$ for the efficient generation of hydrogen under visible light irradiation[131]. In the work of Yuan et al., the authors coupled $MoS_2$ nanosheets with a thin layer of CIS obtaining a higher hydrogen generation rate than with CIS alone[132]. However, as we can see often in these applications CIS is used as a bulk film rather than as QDs.

**Batteries.** This semiconductor can also be used to build anodes for rechargeable lithium batteries. In the work by Zhang's group, the authors were able to produce high surface hollow nanospheres (NSs) composed of smaller QDs via a solvothermal process. In particular, the NSs showed enhanced electrochemical properties compared with CIS QDs alone. The authors ascribed this increase of the performances to the increased surface area and the stable structure of the composites.

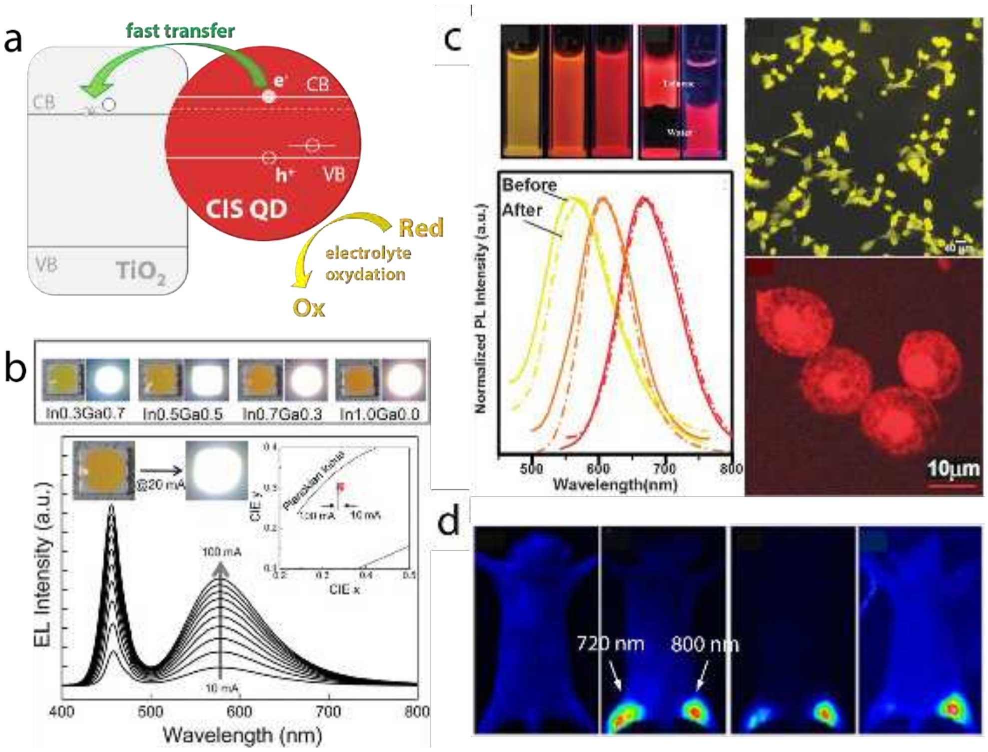

**Figure 1.12.** CIS QDs are nanomaterials suitable for a number of applications. In the PV field, their favorable band alignment with respect to that of $TiO_2$ allows for the preparation of highly efficient QDSSCs, which rely on the fast injection of the electrons from the QD CB to $TiO_2$ CB (*a* – adapted from Ref. [106]). In LED technology, CIS QDs can be incorporated in a polymeric matrix to give a converting layer, giving a layer that can effectively convert to red light part of the blue emission of a blue emitting diode (*b* – reproduced from Ref.[81]). The heavy metal free nature of CIS QDs makes them especially suited for biomedical applications. For instance, they can be employed in cell staining (*c* – reproduced from Ref.[79]) and as nanoprobes for subcutaneous optical imaging, thanks to their excitability and emission at wavelengths falling in the NIR region where scattering and absorption phenomena in biological tissues are reduced (*d* - reproduced from Ref.[17]). The white arrows in d indicate the site of injection of two CIS QDs batches and their respective PL emission maxima. From left to right the images are acquired with the following parameters: *i.* before injection, *ii.* $\lambda_{ex}$ = 660 nm, a 700 nm long pass filter, *iii.* $\lambda_{ex}$ = 660 nm, an 800 nm long pass filter, *iv.* $\lambda_{ex}$ = 766 nm, an 800 nm long pass filter.

The variety of fields for which CIS QDs properties have been tailored and refined throughout almost fifteen years show the versatility of this material. There is no wonder that the research on this material is currently a hot topic. As pointed out in one of the latest work in the field, effort should be put on two fronts: *i.* the precise determination of the emission mechanism in CIS QDs, particularly the attribution of the acceptor levels involved in the radiative transitions and their localization in the crystalline lattice; *ii.* the development of synthetic approaches that allows for a fine control over the size distribution (to avoid the broadband emission characteristic of these QDs) and a "reduction in the positional heterogeneity in the distribution of the emitting centers within a QD"[55].

## 1.3 Plasmonic nanoparticles (PNPs)

In the previous sections I have described the electronic properties of semiconductors, while here I shift my attention to metals and metal-like compounds. In particular, I will focus on the plasmonic phenomena that PNPs host, which have been already extensively studied and applied in a number of field.

### 1.3.1 The physics of PNPs

The optical features of PNPs can be understood in the light of their electronic properties. Here I will consider the case of metals, since the theory was developed for these materials. Nonetheless, the results can be extended to semiconductors and every material in general that under specific condition display a metal-like behavior. Metals do not display separate electronic bands, but rather a continuum of energy levels due to the overlap of VB and CB (Figure 1.13). Because of this overlap, the electrons involved in the formation of the metallic bond are not spatially confined in the nearby of the parent atom, but are delocalized all over the crystalline lattice[133]. These charge carriers (or simply carriers) are free to move and respond to externally applied electric and magnetic fields, such as the AC ones of electromagnetic radiation (*i.e.* light). The optical response of a metal is modulated by a single parameter, which is distinctive for each element: the carrier density ($N_e$). This value allows determining the so-called *plasma frequency* according to the formula:

$$\omega_p = \sqrt{\frac{N_e e^2}{\varepsilon_0 m^*}} \qquad (1.2)$$

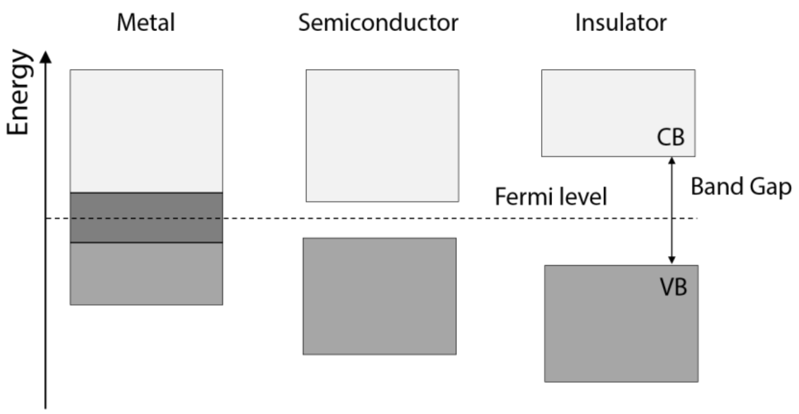

**Figure 1.13.** The behavior of the electronic bands in insulators, semiconductors, and metal differs in the distance between VB and CB. While in insulator the top of the VB and the bottom of the CB are far apart one from the other, in semiconductors the bandgap narrows usually allowing for a direct photoexcitation of the electrons with photons in the visible visible-NIR range. In metals the bands overlap give a continuum of energy levels.

---

Where $e$ is the electronic charge (1.6022 × $10^{-19}$ C), $\varepsilon_0$ is the dielectric permittivity of vacuum (8.8542 × $10^{-12}$ $F{\cdot}m^{-1}$), and $m^*$ is the electron effective mass in the material. This value $\omega_p$ is the characteristic frequency at which the electrons of the material naturally oscillate around their position after a perturbation of the equilibrium. This motion is generated by the restoring force exerted on the electrons by the fixed nuclei: this force pulls the electrons back to their original position but, due to the inertia, they overshoot and start a collective oscillation. Thus, a *plasmon* is a quasiparticle described as a quantized collective motion of charge density. The plasma frequency ($\omega_p$) is a fundamental parameter in the Drude model, which was developed to describe the behavior of metals at the beginning of 1900[134]. In particular, according to this theory, the dielectric permittivity of a metal is given by the formula:

$$\varepsilon(\omega) = \varepsilon_\infty - \frac{\omega_p^2}{\omega^2+\gamma^2} + i\frac{\omega_p^2\gamma}{\omega(\omega^2+\gamma^2)} = Re[\varepsilon(\omega)] + iIm[\varepsilon(\omega)] \qquad (1.3)$$

Where $\varepsilon_\infty$ is a background dielectric constant and $\gamma$ is the damping parameter. The former account for high-frequency interband transitions, the latter for the collision frequency of the carriers[135]. As we can see from Equation 1.3, the dielectric permittivity is a property that depends upon the frequency of the applied field, since the material has a non-instantaneous response to the external stimulus. Moreover, $\varepsilon(\omega)$ is a complex function, where the real part is related to the energy that remains stored in the material, and the imaginary part (*dielectric* *loss*) accounts for the energy losses. An interesting optical phenomenon takes place at the interface of the metallic material and a dielectric upon shining a light of a suitable wavelength: when the Surface Plasmon Resonance (SPR) conditions are satisfied, a collective motion of carriers localized at the surface of the material starts. This can be viewed as an electromagnetic surface wave propagating in a waveguide-like fashion and whose properties are highly influenced by variations of the local dielectric constant. The SPR conditions are matched when the real part of the metal dielectric permittivity is negative and its magnitude is larger than that of the dielectric material[135, 136]:

$$Re[\varepsilon(\omega)]_{metal} < 0 \qquad \text{and} \qquad |Re[\varepsilon(\omega)]_{metal}| > |Re[\varepsilon(\omega)]_{dielectric}| \qquad (1.4)$$

In the frequency domains in which these conditions are satisfied, the light strongly interacts with the carriers. In the case of air/metal and water/metal interfaces, these frequency domains fall in the visible-NIR range. A particular case of SPR is the Localized Surface Plasmon Resonance (LSPR) (Figure 1.14). This phenomenon can be observed only in NPs whose size is smaller than that of the impinging light[137]. The “localized” character of the phenomenon is given by the decrease of the material size below the mean-free path of the carriers. This greatly influences the optical properties of the plasmonic NPs (PNPs): for instance, the damping parameter $\gamma$ in Equation 1.3 becomes larger than in bulk, since the probability of scattering events is higher due to enhanced interaction of the carriers with the PNP surface (boundary effect). When the electric component of an electromagnetic radiation interacts with a PNP, the carriers are displaced from their equilibrium position, leaving a localized uncompensated charge density at the PNP surface.

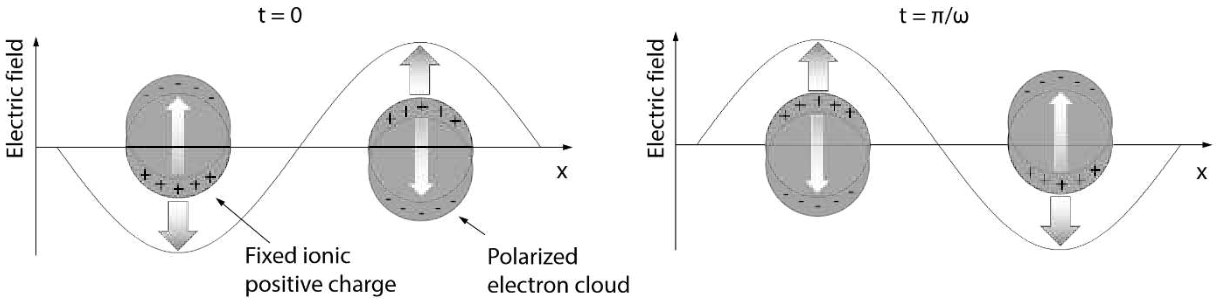

**Figure 1.14.** When a photon with a frequency ($\omega$) satisfying the LSPR condition hits a PNP surface, its oscillating electric field triggers an oscillation of the carriers. In the case of metal PNPs the cloud of electrons

starts oscillating around the original position while the nuclei that compose the lattice can be considered to maintain a fixed position. This charge displacement determines the creation of a dipole moment inside the PNP.

The carrier oscillations that follow this event are identical to those described for bulk materials. In order to quantitatively describe this phenomenon, it is useful to consider two approximations: *i.* the electronic structures of the PNPs are considered similar to that of bulk material and *ii.* the polarization generated by the light is uniform inside each PNP[138]. Under these conditions, the response of the spherical PNP electrons to an AC electric field is described by the dipolar approximation:

$$\alpha = 4\pi R^3 \frac{\varepsilon - \varepsilon_m}{\varepsilon + 2\varepsilon_m} \tag{1.5}$$

Where $\alpha$ is the electric polarization, $\varepsilon_m$ is the dielectric permittivity of the medium in which the nanoparticles are embedded (dielectric), and $R$ is the PNP radius. Considering the imaginary part of the dielectric permittivity negligible, the LSPR condition is satisfied for (Fröhlich condition)[139]:

$$Re[\varepsilon(\omega)] = -2\varepsilon_m \tag{1.6}$$

This means that the frequency at which the localized surface plasmon is observed is:

$$\omega_{LSPR} = \sqrt{\frac{N_e e^2}{\varepsilon_0 m^* (2\varepsilon_m + \varepsilon_\infty)} - \gamma^2} \tag{1.7}$$

As we can observe from Figure 1.15, there is a mismatch between the predicted values (a) and the actual LSPR peak position (b). This effect stems from the fact that the model described above does not take into account the imaginary part that accounts for the losses[135]. To conclude, although not being extremely accurate, this theory describe the plasmonic effect in a straightforward way, allowing for an easy and immediate estimation of the PNP properties. The considerations that have been made in this Section considering the behavior of metals can be extended to any kind of materials having either negatively (electrons) or positively (holes) charged free carriers. In particular, the latter is the case of copper sulfide PNPs.

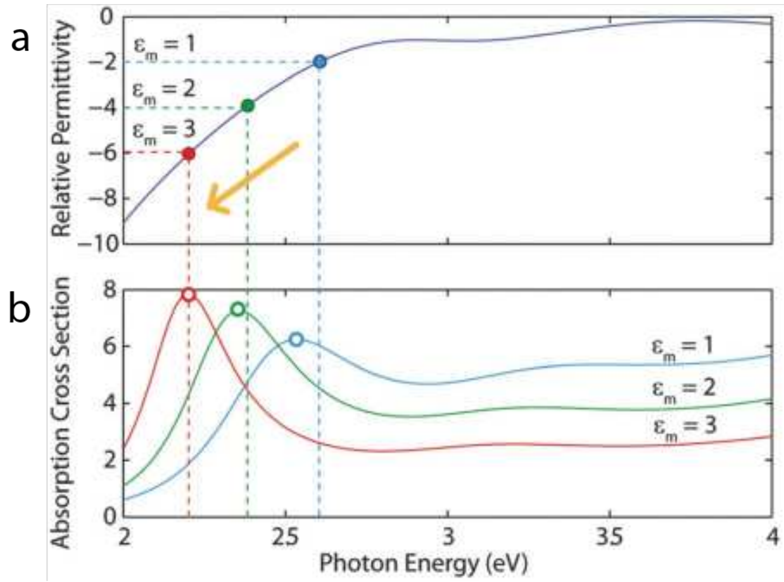

**Figure 1.15.** The LSPR frequency of Au-PNPs depends on the dielectric permittivity of the environment. In *a* it is possible to graphically appreciate how the resonance condition is satisfied in different environments by observing the intersection of the real part of the permittivity with an horizontal (dashed) line drawn at $-2\varepsilon_m$. The difference between the so-calculated $\omega_{LSPR}$ and the one observed in the absorption spectra simulated in the dipole approximation (*b*) stems from the fact that in *a* the imaginary part of the dielectric permittivity is neglected. Reproduced from Ref. [135]

## 1.3.2 The photothermal effect in PNPs and photothermal therapy (PTT)

In the wavelength range where LSPR peak is located, PNPs display an enhanced molar extinction coefficient. This is composed of two components accounting respectively for the absorption and the scattering. The part of radiation that is absorbed by the material is converted into heat through a series of non-radiative processes[140, 141]. This phenomenon is referred to as *photothermal effect*. The heat conversion takes place following three steps:

1- Part of the impinging light is absorbed by the PNPs, while the rest is scattered.

2- Electron thermalization takes place on a femtosecond timescale. A state of hot electrons is reached due to electron-electron interactions. The hot electrons temperature can reach values of thousands of degrees.

3- The electrons exchange the heat via electron-phonon relaxation processes. This happens in picoseconds, and the lattice temperature can increase of tens of degrees.

4- After the creation of a hot lattice stage, the lattice eventually cools off by means of phonon-phonon relaxation. This last stage corresponds to the dissipation of the heat in the surrounding environment.

It is on this effect that photothermal therapy (PTT) is based. This therapeutic method for the treatment of solid tumors takes advantage of the use of heat converters (*e.g.* PNPs) that can be excited with a light of a suitable wavelength. These PTT agents then convert the light into heat, transferring it to the nearby cells. A controlled local increase of the temperature between 40 - 45 °C leads to a programmed cellular death (*apoptosis*), which is a process that does not lead to inflammatory conditions[142]. This therapeutic approach is minimally invasive and allows for an extremely precise control of the treated area, thus minimizing the side effects on healthy cells[143]. This control can be exerted simultaneously in two ways: promoting a specific accumulation of the PTT agents exclusively at the tumor site and shining the triggering light only on the area of interest. The applicability of PTT is, however, limited by the penetration depth through the biological tissue of the triggering light (Figure 1.16). Indeed, often PTT is used to treat skin conditions and melanomas. For this reason, with the aim of expanding the boundaries of this therapeutic modality, NIR absorbing PNPs are currently being deeply explored as PTT agents[144].

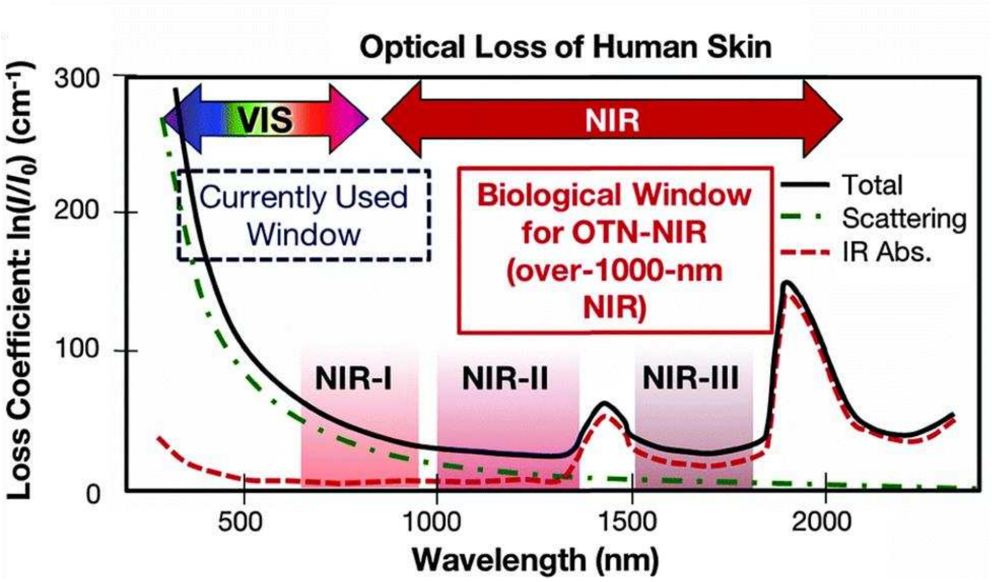

**Figure 1.16.** When designing an optical system to be used *in vivo*, it is necessary to take into account the different depth of penetration that different wavelengths display. In particular scattering (mainly in the UV-visible range due to lipids) and absorption (mainly in the NIR range due to water) contribute for the total loss coefficient of biological tissues. The three OTWs (here named NIR-I, NIR-II, and NIR-III) are optical ranges where the penetration depth is maximized. This enhanced penetration stems from the reduced losses that a light of a wavelength falling in this intervals experiences travelling through a biological tissue. Reproduced from Ref.[146]

Actually, NIR light penetrates deeper in biological tissues than visible light does, due to reduced absorption and scattering phenomena occurring in this spectral region. In particular, it is possible to individuate specific wavelength ranges, also called optical transparency windows (OTWs), where the light penetration is maximized[145].

## 1.4 Copper sulfide plasmonic nanoparticles.

### 1.4.1 Gold, the noble brother

The unique optical behavior of metal PNPs made them a prosperous research subject in the last years. Specifically, silver, copper, and gold NPs all show LSPR bands falling in the visible region, unlike other metals that display weak UV-centered LSPR bands. Above all, gold received the greatest deal of attention, in particular due to its outstanding chemical stability and the ease of the synthetic methods to produce Au-PNPs. Here, I will not review the countless works that have been published so far about the synthesis and application of Au-PNPs. Actually, their preparation follows completely different approaches than those proposed for $Cu_{2-x}S$ PNPs, and an accurate review of these synthetic routes would fall out of the scope of the thesis. However, I will briefly enumerate some application fields for which Au-PNPs have been proposed and used for, in order to set the ground for a comparison with $Cu_{2-x}S$ PNPs.

Indeed, Au-PNPs are extremely versatile in terms of the control that can be exerted over their optical properties by tuning their size and morphology. Au-PNPs can be synthesized in the shape of nanospheres (NSs)[147], nanorods (NRs)[148], nanostars[149], nanourchins[150], nanocages[151], nanoshells[152], and hollow NSs[153], just to name the most common ones (Figure 1.17). Each morphology has distinctive optical features. Profiting from the high degree of sophistication that the synthesis of these plasmonic nanostructures has achieved, it is possible to tailor the LSPR properties of Au-PNPs to span an incredibly extended optical range, from the visible to the NIR (Figure 1.17b). Moreover, Au surface chemistry is very well-known: the high affinity displayed by Au-PNPs toward amine and thiol groups makes the surface modification of these systems straightforward, allowing for a fine control over the specific interaction of Au-PNPs with other moieties. Depending on their sizes, the range in which their LSPR peak falls, and their surface chemistry, these Au-PNPs can be used for different applications.

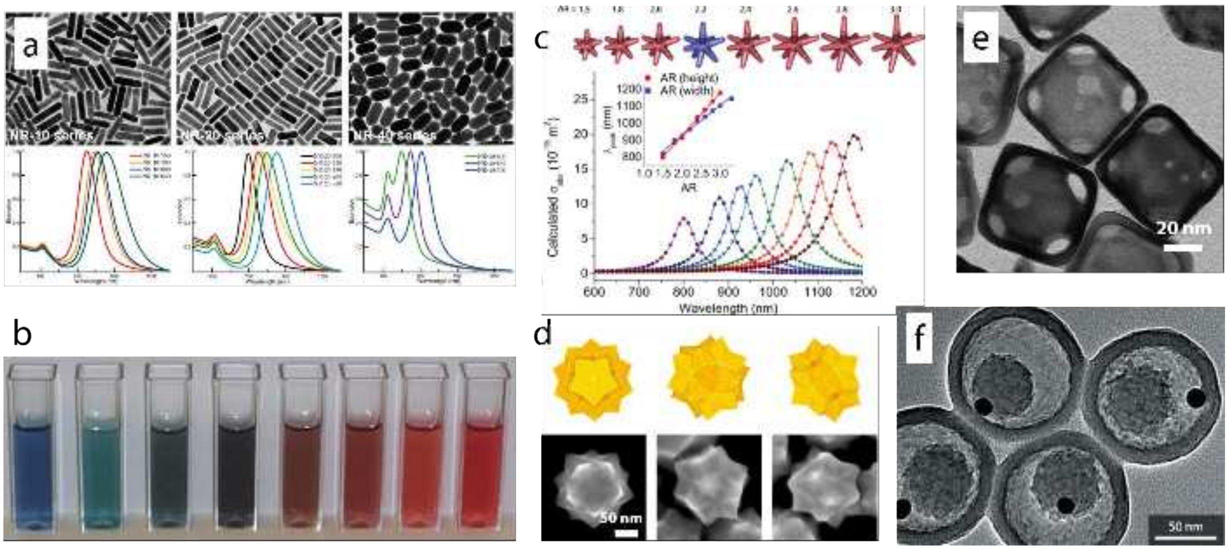

**Figure 1.17.** Different types of Au-PNPs that have been designed to effectively reach the NIR range: GNRs (*a* – Reproduced from Ref. [154]) and sols of GNRs with different aspect ratios (*b* – Reproduced from Ref.[140]), Au-nanostars (*c* and *d,* reproduced respectively from Ref.[155] and Ref. [156]), Au-nanocages (*e* – Reproduced from Ref. [157]), and Au-nanoshells (*f* – Reproduced from Ref.[158]). In *d* the scale bar is 50 nm.

For instance, Au-PNPs whose surface has been conveniently modified can be used in colorimetric assays for the determination of metal ions in solution[159], small molecules such as glucose[160] and uric acid[161], hydrogen peroxide[162], proteins[163], and DNA[164] to name a few. Au-PNPs are well-established probes in surface enhanced Raman scattering (SERS) spectroscopy[165]. They can also be used for the creation of anti-bacterial agents[166] and to enhance the performances of photovoltaic devices[167]. One of the fields where Au-PNPs finds an incredible number of applications is nanomedicine. Au-PNPs have been often engineered to act as drug delivery systems, since different drugs can be easily attached on their surface[149, 168]. This approach allows for an increased accumulation of the formulation at the tumorous site thanks to the enhanced permeation and retention (EPR) effect, which is promoted by the blood vessel fenestration in correspondence of the tumor[169]. A more specific accumulation of the drug is achieved via the surface modification of Au-PNPs with molecules that specifically binds to cancer cells receptors (active targeting). Specifically, the drug attached on the Au-PNP surface can be a photosensitizer (PS) for photodynamic therapy (PDT)[170]. PSs are a class of molecules that absorb light and transfer the energy to nearby oxygen to give cytotoxic reactive oxygen species (ROS), leading to cell apoptosis[171]. Due to their large absorption cross-section, Au-PNPs have been proposed as radiation therapy enhancers. The incorporation of Au$^{198}$ isotope in the particles that accumulate in the site to be treated enhance the effective radiation dose of more than 200 % with respect to normal tissues[172].

More recently, Au-PNPs have also been tested as photoacoustic contrast agents[173]. Eventually, Au-PNPs are outstanding PTT agents, thanks to their ability to convert light into heat according to the photothermal effect described in section 1.3.2.

### 1.4.2. Copper sulfide PNPs: an affordable alternative

**Properties.** Copper sulfide is a semiconductor material with an incredibly rich chemistry. Indeed, a large number of compounds falls under the general name of copper sulfide and they all display a defined chemical composition with a unique crystalline structure. For this reason, the community usually refers to the large family of copper sulfide materials with the generic formula $Cu_{2-x}S$, where $x$ can take values between 0 and 1[174]. Other than the two extreme compounds (CuS – covellite and $Cu_2S$ - chalcocite), in the $Cu_{2-x}S$ family we find $Cu_{1.97}S$ – djurleite, $Cu_{1.80}S$ – digenite, $Cu_{1.75}S$ – anilite, $Cu_{1.60}S$ – geerite, $Cu_{1.40}S$ – spionkopite, and $Cu_{1.12}S$ – yarrowite. Bulk copper sulfide is an important material from a technological viewpoint due to its outstanding superconductor behavior at 1.63 K in its bulk covellite phase[175]. However, in its nano-sized form it has been recently brought to the attention of the community for a plethora of applications. Generally speaking, $Cu_{2-x}S$ is a degenerate (*i.e.* self-doped) p-type semiconductor with a wide variety of direct energy gap values[135]. The self-doped character of this semiconductor stems from the distinctive Cu-deficient stoichiometry of the material. Indeed, when one Cu atom is removed from the structure, one vacancy is introduced in the VB[135]. The presence of these charge carriers is the reason for the metal-like behavior of heavily sub-stoichiometric polymorphs ($x \approx 1$). It is evident, that covellite (CuS) is the compound of the copper sulfide family that shows the strongest p-type metallic behavior, since it has the largest number of free carriers. Therefore, it is not surprising that this is also the compound displaying the more intense LSPR band. In this regard, it is worth noticing that the plasmonic peak of this material is naturally centered in the NIR region. This feature makes $Cu_{2-x}S$ (and particularly CuS) PNPs incredibly charming in view of their application for PTT and, in general, for *in vivo* applications that requires NIR triggered agents, as we will see later. Cu and S valence is a fundamental parameter in $Cu_{2-x}S$ compounds, since it gives an insight about the electronic behavior of the system. The top of the VB has a marked contribution from the p orbitals of S, so that the introduction of vacancies in the VB should bring along a change of the chalcogen valence. Actually, XPS studies conducted on thin films have shown that the valence of Cu is always +1, while the one of S passes from -2 in chalcocite to a value higher than -2 in sub-stoichiometric compounds.

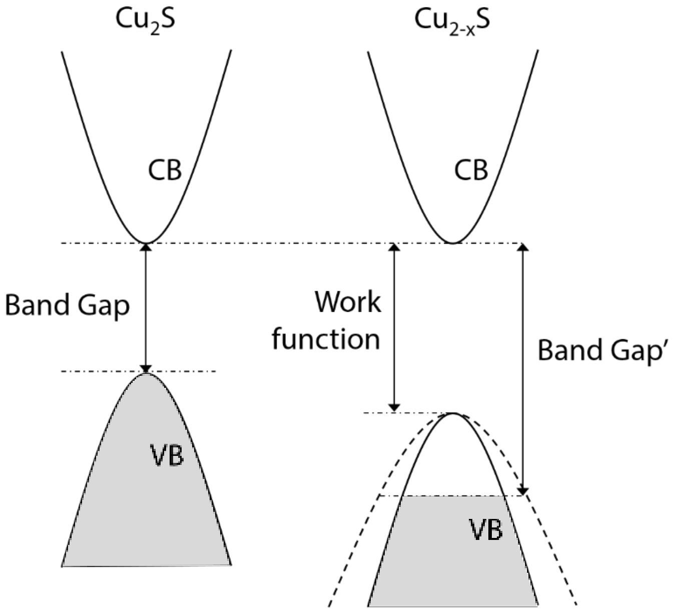

**Figure 1.18.** When passing from $Cu_2S$ to $Cu_{2-x}S$ the effect of removing a $Cu^+$ ion is the introduction of a hole in the VB. At the same time, the VB energy decreases with a consequent increase of the work function (*i.e.* the energy needed to remove one electron from the material surface). Moreover, the curvature of the VB increases, leasing to a decrease of the hole effective mass. Adapted from Ref. [135]

This in accordance with the observation of the strong S 2p character of top of the VB. However, in the particular case of $Cu_{2-x}S$ PNPs, this is still under debate. Some studies have assigned to Cu a valence between 1 and 1.5[176], while sulfur is present both as $S^{2-}$ and $S_2^{2-}$ [177]. The plasmonic properties of CuS PNPs can be rationalized in the frame of the Drude model described in Section 1.3.1. The only substantial difference with respect to the formula there reported is that the density of charge carriers is actually a density of holes ($N_h$). Although the seminal work about the synthesis and study of plasmonic CuS PNPs was published in 2009 by the group of Burda[178], a first quantitative description of the plasmonic properties of these self-doped semiconductor PNPs was reported the following year by the group of P. Alivisatos[179]. The authors observed that the LSPR peak intensity and position are both size-dependent. Specifically, in very small PNPs (below 3 nm) the LSPR extinction is absent, and its intensity increases with increasing PNP size. A solvatochromic effect was observed when dispersing the PNPs in organic solvents with different refractive index. This behavior is in accordance with the strong dependence of the LSPR effect upon the dielectric permittivity of the medium in which the PNPs are embedded. Furthermore, the authors submitted the PNPs to a controlled oxidation via exposition to ambient air, observing that the increased number of vacancies introduced by this oxidative event enhances the plasmonic properties of the material. However, the most intense work has been conducted by the group of Manna, who has been investigating in depth the behavior of plasmonic chalcogenide PNPs in general[135, 180, 181]. Indeed, most of the considerations about the optical properties of CuS PNPs made so far come from the investigation conducted by this group.

**Synthesis and applications of $Cu_{2-x}S$ PNPs.** Generally speaking about copper sulfide nanosystems, non-plasmonic $Cu_{2-x}S$ NPs have been successfully applied in *in vitro* assays for glucose[182], DNA[183], and food borne pathogens[184] to name a few. These applications rely on the good conductive properties displayed by these PNPs. However, more recently attention has been shifting toward the use of $Cu_{2-x}S$ PNPs for *in vivo* applications, due to the strong plasmonic feature displayed by this material in the NIR that well matches the range of the OTWs. There are two main advantages in using $Cu_{2-x}S$ PNPs instead of systems based on Au. First, the cost production is lower. Second, the LSPR peak remains located in the NIR region even for small PNPs, while to reach such long wavelengths with Au-PNPs it is necessary to synthesize large structures (NRs, nanostars, or nanoshells). This is a pivotal feature, since the use of small PNPs in theranostic applications favors the accumulation at the tumor site due to the EPR effect[185]. The synthesis of $Cu_{2-x}S$ PNPs dates back to the work of Zhao et al., where the authors synthesized different polymorphs using three different approaches: sonoelectrochemical, hydrothermal, and solventless thermolysis[178]. They performed an accurate analysis of the optical properties of the different materials both considering the excitonic absorption at short wavelengths and the NIR LSPR feature. Finally overcoming the wrong assignment of an indirect bandgap to this class of material[186], they also correctly attributed the dependence of the plasmonic absorption on the carrier concentration in the material. For the first time water-dispersible $Cu_{2-x}S$ PNPs were synthesized and proposed as PTT agents by Li et al. using thioglicolic acid (TGA) and thioacetamide[187]. Nonetheless, these particles displayed a rather weak LSPR absorption band, which limited their efficacy as therapeutic agents. Tian et al. synthesized digenite PNPs in oleylamine (OLAm) using Cu(diethyldithiocarbamate) via a thermal decomposition approach. They performed the water transfer via a ligand exchange with 6-amino caproic acid and used this system for PTT, obtaining a heat conversion efficiency (HCE) of 25.7 %[188]. Later, the same group demonstrated that the use of superstructures increases the HCE of almost 50 % with respect to single covellite PNPs[189]. In this study, the PNPs were synthesized via a hydrothermal approach in the presence of PVP changing the reaction time from 12 h to 48 h in order to obtain either the single PNPs or flower-like composites.

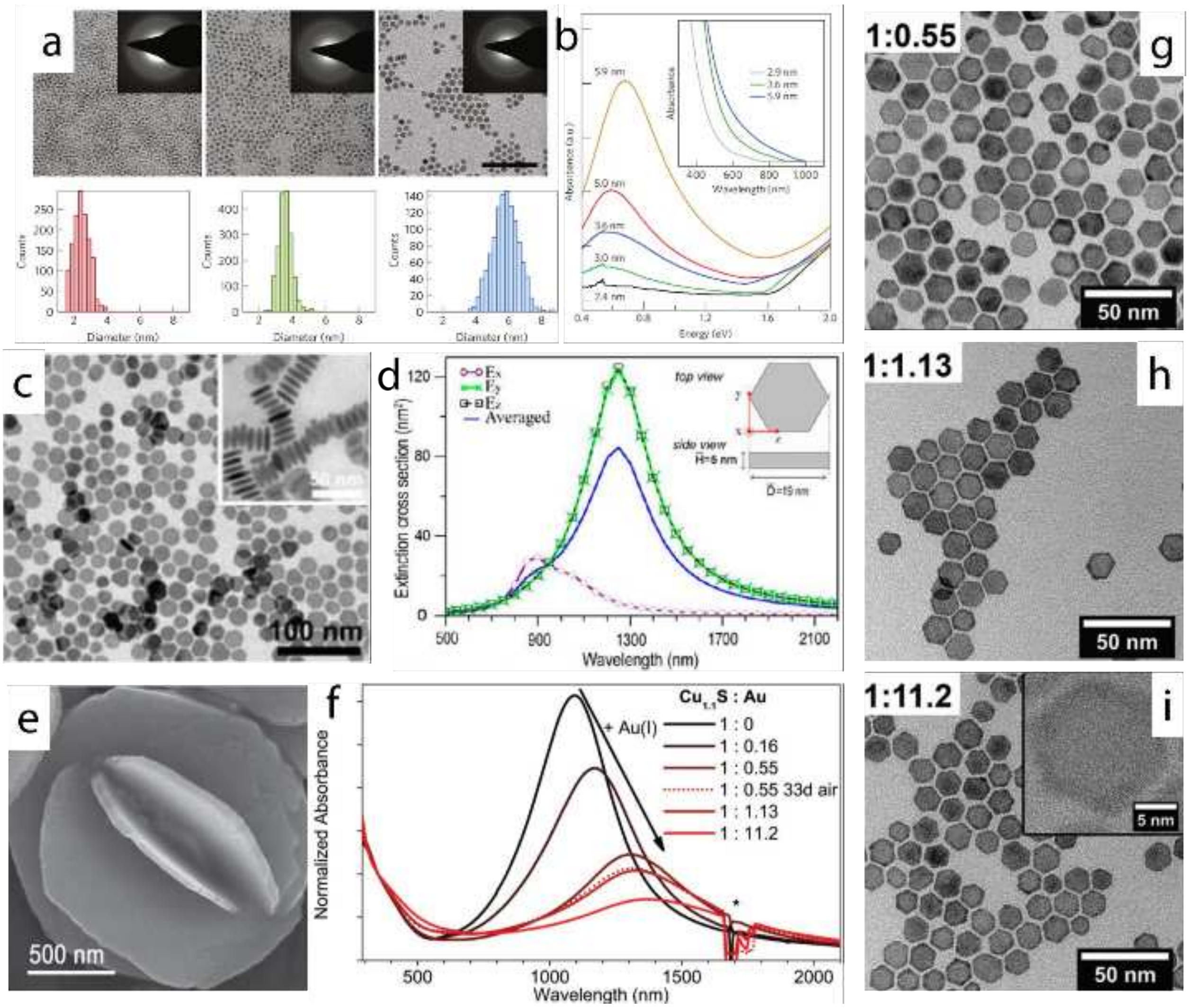

**Figure 1.19.** Some of the $Cu_{2-x}S$ PNPs synthesized in the last 8 years. Small djurleite PNPs (*a*) with strong LSPR absorption (*b*) were synthesized by Luther et. al. (reproduced from Ref.[179]). Xie et al. studied the optical response of covellite nanoplatelets (*c*) finding a weak contribution of out-of-plan modes (*d*) (reproduced from Ref. [180]). CuS PNPs superstructures (*e*) allow to obtain an increased HCE if compared to the parent building blocks (reproduced from Ref.[189]), while a controlled intercalation of $Ag^+$ in $Cu_{1.1}S$ nanodisks was shown to red-shift the LSPR peak and increase the PNP resistance to oxidation (*f*). The PNPs resulting from this intercalation process are shown in g, h, I (reproduced from Ref.[191]).

On the same path, recently Tan et al. investigated the behavior of CuS PNP mesostructures[190], finding an enhanced phothermal activity with respect to the single building blocks under 980 nm excitation. Luther et al. published a study on the optical properties of djurleite PNPs synthesized from Cu(acetylacetonate) in OA and DDT with a thermal decomposition approach, managing to control the PNP size by changing the S/Cu ratio[179]. Later, Ku et al. first reported the use of pegylated $Cu_{2-x}S$ PNPs as exogenous contrast agents for photoacoustic tomography (PAT)[192]. They synthesized the PNPs directly in water, using citrate as the stabilizer molecule, and then they pegylated them to impart biocompatibility and more colloidal stability. Using a 1060 nm CW laser, they were able to image the PNPs in mouse brain and rat lymph nodes. Most importantly, they showed that these contrast agents could be localized under almost 5 cm of chicken breast. Recently, also Ding et al. similarly reported on the possibility of using $Cu_{2-x}S$ PNPs, directly synthesized in a PEG-thiol solution, as PAT contrast agents[193]. Wang et al. produced 6.5 nm $Cu_{2-x}S$ PNPs via the hot injection of a ODE sulfur solution in a OLAm solution of copper [181]. After a pegylation step, they confirmed the good performances of the particles as PTT agents (HCE = 16.3 %) and reported the generation of ROS upon NIR irradiation, claiming for the evidence of $Cu_{2-x}S$ PNP mediated PDT[181]. However, the ROS generation does not stem from the PNPs themselves, but rather from the leakage of $Cu^{2+}$ ions in solution that undergo a redox reaction leading to the production of ROS. On the side of more fundamental studies, in 2013 Xie et al. analyzed the optical properties of covellite nanoplatelets synthesized in OA, OLAm, and ODE[180]. The authors pointed out the presence of different in-plane and out-plane LSPR modes, and a carrier density as high as $10^{22}$ $cm^{-3}$. Then, Ann Mary et al. compared the behavior of nanospheres and nanoplatelets synthesized in water in the presence of PVP: they observed that the nanoplatelets are more efficient NIR absorbers (thus heat converters) due to the presence of less stacking faults and twinning, *i.e.* trap levels, in the crystals [194]. The good affinity of amine groups towards copper is often exploited in the synthesis of these systems. For instance, OLAm was used for the synthesis of $Cu_{2-x}S$ PNPs from Huang et. al., who successfully transferred the particles to water using phospholipid micelles [195]. The water dispersed PNPs were employed as subcutaneous PTT agent thanks to their remarkable HCE of 31.4 %. Following the OLAm synthetic route, Wolf et al. explored the possibility of alloying $Cu_{1.1}S$ PNPs (and $Cu_{2-x}Se$) with $Au^+$ and $Ag^+$ via a cation exchange process[191]. They showed that intercalation of $Ag^+$ and ion exchange with $Au^+$ in $Cu_{1.1}S$ PNPs both lead to a bathochromic shift of the LSPR peak (*i.e.* a shift toward longer wavelengths) and an increased resistance of the material towards oxidation. Covellite PNPs were synthesized in OLAm also from Liu et al.[203]. They obtained a mixture of nanoplatelets and NSs that they separated via centrifugation, observing that the addition of ammonium sulfide in this stage leads to a controlled growth of the two populations of PNPs. Controlling the size of the particles, they were able to tune the LSPR peak position over a broad NIR range. Moreover, theoretical calculations demonstrated the predominance of in-plane modes in plasmonic response of these PNPs. An innovative use of $Cu_{2-x}S$ PNPs as light-triggered sterilants was proposed by Liu et al., who managed to permanently sterilize male mice after local injection of the nanoheaters and irradiation with a

980 nm CW laser[204]. Recently, Cheung et al. described a continuous-flow microfluidic approach for the synthesis of different $Cu_{2-x}S$ PNPs[205]. The relatively low reaction temperature of 120 °C in organic solvents (ODE, OLAm, and OA) and ease of operation make this approach a robust synthetic method for the reproducible synthesis of chalcogenide PNPs. At the time this thesis has been written, the record value of HCE has been obtained with digenite PNPs by Li et al., with an outstanding value of 56.7 %[198] which makes these chalcogenide PNPs incredibly efficient heat converters even compared to some Au-PNPs (Table 1.1).

**Composite systems.** Other than systems based only on $Cu_{2-x}S$, more complex nanostructures have been proposed as multimodal theranostic agents. In particular, Xiao et al. synthesized a core/satellite structure using silica-coated upconverting NPs (UCNPs) decorated with $Cu_{2-x}S$ PNPs. This system combines the effect of PTT and enhanced radiotherapy with the possibility of real-time tracking using magnetic resonance (MR), upconversion (UC)-based optical imaging, and computed tomography (CT)[206]. Exploiting the same multimodal concept, Lv et al. developed an *in situ* strategy to grow $Cu_{2-x}S$ PNPs on the surface of dopamine coated UCNPs[207].

**Table 1.1.** Comparison of the HCE of different systems reported in the literature.

| Material | $\lambda_{ex}$, *nm* | I, *mW* | HCE, *%* |
|---|---|---|---|
| Hollow Au-Ag alloy nanourchins[196] | 808 | 1000 | 80.4 |
| Au NRs[197] | 815 | 151 | 61 |
| Au/AuS nanoshells[197] | 815 | 161 | 59 |
| $Cu_{7.2}S_4$ nanoplatelets[198] | 980 | 290 | 56.7 |
| Au NRs[199] | 808 | 2000 | 50 |
| Dopamine-melanine colloidal NSs[200] | 808 | 2000 | 40 |
| Biodegradable Au nanovescicles[201] | 808 | 1000 | 37 |
| $Au/SiO_2$ nanoshells[197] | 815 | 163 | 34 |
| CuS NSs[195] | 808 | 1 ($W/cm^2$) | 31.4 |
| $Cu_9S_5$ nanoplatelests[188] | 980 | 510 | 25.7 |
| Au nanoshells[199] | 808 | 2000 | 25 |
| $Cu_{2-x}Se$ nanoparticles[202] | 800 | 2000 | 22 |
| Au NRs[201] | 808 | 1000 | 22 |
| Au nanoshells[201] | 808 | 1000 | 18 |
| $Cu_{1.8}S$ NSs[181] | 808 | 1890 | 16.3 |

The incorporation of $Cu^{2+}$ ions in the polymeric layer during the transfer to water of UCNPs allowed for the subsequent growth of the PNPs directly on the surface of the phosphors upon addition of sodium citrate and $Na_2S$. Liu et al. developed a simple method to synthesize mesoporous silica-coated $Cu_{2-x}S$ PNPs: the PNPs are grown directly in a CTAB aqueous solution and, after the silica coating, the system can be loaded with doxorubicin (DOX) to obtain a PTT agent with drug delivery capabilities[208]. The silica shell impart also stability to the system that can withstand without apparent degradation several cycles of laser irradiation. A common strategy to obtain efficient drug carriers is to build hollow structures. Indeed, Han et al. produced $Cu_{2-x}S$ hollow PNPs loaded with a PS molecule (indocyanine green) to perform simultaneous PTT and PDT under 808 nm laser irradiation[209]. The nanostructure was further engineered attaching on its surface bovine serum albumin (BSA) and folic acid to impart stealth and active targeting properties respectively. Eventually, for the first time plasmon-enhanced UC emission was reported using $Cu_{2-x}S$ PNPs[210]. Zhou et al. prepared sulfide and UCNP films of controlled thickness placing between them a $MoO_3$ spacer layer. The thickness of this oxide layer has a strong impact on the UC signal enhancement along with the size of the PNPs.

As we can observe from the relatively limited literature about the subject, the systematic use and study of $Cu_{2-x}S$ PNPs is a young and expanding research field, which is expected to grow even more in the next years due to the unique properties of this plasmonic material.

## 1.5 Aim of the research

In this thesis, I present the results of the study on optically active CIS QDs and $Cu_{2-x}S$ PNPs. As presented in the previous sections, these chalcogenide-based nanoparticles are currently under intense study, since the last years of research have proved them to be viable, reliable, non-toxic, and cheap alternatives to the state of the art materials used in many application fields. The purpose of my research has been to develop easy synthetic methods to produce NPs having specific characteristics, such as the possibility of dispersing them in polar organic solvents or displaying better optical properties. In a second phase, I explored the effect of combining these NPs with rare-earth (RE) doped NPs to investigate the interaction between the two moieties and obtain augmented properties.

Specifically, my research on CIS QDs has led to the preparation of mercaptosilane-passivated CIS QDs synthesized via a simple one-pot thermal decomposition approach

(Chapter 2). The unique feature of these QDs is the possibility of dispersing them in organic polar solvents due to a complex surface chemistry. This distinctive characteristic, obtained without any post-synthesis surface modification, makes these QDs attractive from an applicative viewpoint, since only few QDs display this particular property. Moreover, the slow reaction kinetics allowed observing a growth mechanism characterized by the presence of QDs having discrete sizes, a behavior that was never reported in the literature.

In the framework of the optimization of the synthetic approaches for CIS QD synthesis, I later shifted my attention to the most commonly utilized thermal decomposition method conducted in 1-octadecene and 1-dodecanethiol. Although this procedure is well-established, a precise knowledge of the effect that each synthetic parameter has on the final properties of the QDs has not been achieved yet. In this regard, I analyzed the effect that different halogen anions have on the properties of CIS QDs when these ions are present in the reaction environment in the form of copper (I) chloride, bromide, and iodide (Chapter 3). Combining different characterization techniques, we observed evidences of the incorporation of the anions in the lattice. The results show that the polarizability of the halogen ions affect the growth and the optical properties of the dots following the trend of the so-called *Hofmeister* series.

The expertise gained in the synthesis and control of the optical properties of CIS QDs was later used to investigate the energy transfer (ET) mechanism between CIS QDs and upconverting NPs (UCNPs) doped with RE ions (Chapter 4). This fundamental study was carried in order to deepen the knowledge about this subject that has been scarcely tackled in the literature. The results of these investigations would be valuable information for the development of all-inorganic probes for Förster resonance energy transfer (FRET)-based assays. With the aim of setting the ground for the design of these optical probes, I selected $LiYF_4$:Yb,Tm as the host-dopant ions combination for UCNPs and investigated the effect that different core/shell donor (UCNP) architectures have on the ET mechanism. The study was conducted both in solution and on samples dried on a substrate, in order to assess the nature of the ET (radiative versus non-radiative) between the two moieties. The results show that FRET can be observed between these inorganic species only when they are constrained in close proximity (*i.e.* in their dried form). Furthermore, a careful design of the donor is necessary in order to increase the fraction of optically active ions on the UCNP surface without decreasing the PLQY value too much.

On a different side, I designed a green and cheap approach for the synthesis of $Cu_{2-x}S$ PNPs, especially focusing my attention on their potential application as photothermal agents (Chapter 5). This field has become a particularly hot topic in the last few years as shown in the previous Sections. So the development of synthetic protocols that allow for an easy and controlled synthesis of non-metallic PNPs readily dispersible in water is particularly attractive. In particular, following this newly developed approach, quasi-spherical pure phase covellite CuS PNPs with a localized surface plasmonic resonance (LSPR) peak centered in the NIR region were obtained. The characterization of these PNPs showed that variations of the reaction parameters such as temperature, pH, and copper-to-sulfur ratio allow for a fine control over structural, morphological, and optical properties. These PNPs display a high heat conversion efficiency (HCE) of 44.2 %, a value that makes them a competitive cheaper substitute for the more studied gold-based photothermal agents.

## References

1. The European Commission. *Official Journal of the European Union* **2011,** 275, 38-40.
2. Vajtai, R., *Springer Handbook of Nanomaterials*. Springer Berlin Heidelberg: 2013.
3. Koole, R.; Groeneveld, E.; Vanmaekelbergh, D.; Mieijerink, A.; Donegá, C. d. M., Size Effects on Semiconductor Nanoparticles. In *Nanoparticles*, Donegá, C. d. M., Ed. Springer Berlin Heidelberg: 2014; pp 13-51.
4. Parak, W. J.; Manna, L.; Simmel, F. C.; Gerion, D.; Alivisatos, P., Quantum Dots. In *Nanoparticles*, Wiley-VCH Verlag GmbH & Co. KGaA: 2005; pp 4-49.
5. Smith, A. M.; Nie, S. *Acc Chem Res* **2010,** 43, (2), 190-200.
6. Reiss, P.; Protière, M.; Li, L. *Small* **2009,** 5, (2), 154-168.
7. Aboulaich, A.; Michalska, M.; Schneider, R.; Potdevin, A.; Deschamps, J.; Deloncle, R.; Chadeyron, G.; Mahiou, R. *ACS Appl Mater Interfaces* **2014,** 6, (1), 252-258.
8. Jia, Y.; Wang, H.; Yan, Z.; Deng, L.; Dong, H.; Ma, N.; Sun, D. *RSC Adv.* **2016,** 6, (96), 93303-93308.
9. Li, L.; Daou, T. J.; Texier, I.; Tran, T. K. C.; Nguyen, Q. L.; Reiss, P. *Chem Mater* **2009,** 21, (12), 2422-2429.
10. Park, J.; Kim, S.-W. *J Mater Chem* **2011,** 21, (11), 3745-3750.
11. Mandal, A.; Dandapat, A.; De, G. *Analyst* **2012,** 137, (3), 765-772.
12. Zhang, W.; Li, Y.; Zhang, H.; Zhou, X.; Zhong, X. *Inorg Chem* **2011,** 50, (20), 10432-10438.

13. Bailey, R. E.; Nie, S. *J Am Chem Soc* **2003,** 125, (23), 7100-7106.

14. Shen, S.; Wang, Q. *Chem Mater* **2013,** 25, (8), 1166-1178.

15. Yakushev, M. V.; Mudryi, A. V.; Victorov, I. V.; Krustok, J.; Mellikov, E. *Appl Phys Lett* **2006,** 88, (1), 011922.

16. Wang, Y. H.; Zhang, X.; Bao, N.; Lin, B.; Gupta, A. *J Am Chem Soc* **2011,** 133, (29), 11072-11075.

17. Deng, D.; Chen, Y.; Cao, J.; Tian, J.; Qian, Z.; Achilefu, S.; Gu, Y. *Chem Mater* **2012,** 24, (15), 3029-3037.

18. Jaffe, J. E.; Zunger, A. *Phys Rev B* **1984,** 29, (4), 1882-1906.

19. Kolny-Olesiak, J.; Weller, H. *ACS Appl Mater Interfaces* **2013,** 5, (23), 12221-12237.

20. Scheer, R.; Klenk, R.; Klaer, J.; Luck, I. *Sol Ener* **2004,** 77, (6), 777-784.

21. Booth, M.; Brown, A. P.; Evans, S. D.; Critchley, K. *Chem Mater* **2012,** 24, (11), 2064-2070.

22. Contreras, M. A.; Romero, M. J.; Noufi, R. *Thin Solid Films* **2006,** 511-512, 51-54.

23. Park, M.; Ahn, S.; Yun, J. H.; Gwak, J.; Cho, A.; Ahn, S.; Shin, K.; Nam, D.; Cheong, H.; Yoon, K. *J Alloys Compd* **2012,** 513, 68-74.

24. Connor, S. T.; Hsu, C. M.; Weil, B. D.; Aloni, S.; Cui, Y. *J Am Chem Soc* **2009,** 131, (13), 4962-4966.

25. Li, Q.; Zhai, L.; Zou, C.; Huang, X.; Zhang, L.; Yang, Y.; Chen, X.; Huang, S. *Nanoscale* **2013,** 5, (4), 1638-1648.

26. Kruszynska, M.; Borchert, H.; Parisi, J.; Kolny-Olesiak, J. *J Am Chem Soc* **2010,** 132, (45), 15976-15986.

27. Bao, N.; Qiu, X.; Wang, Y. H.; Zhou, Z.; Lu, X.; Grimes, C. A.; Gupta, A. *Chem Commun* **2011,** 47, (33), 9441-9443.

28. Nam, D.-E.; Song, W.-S.; Yang, H. *J Mater Chem* **2011,** 21, (45), 18220-18226.

29. Nam, D.-E.; Song, W.-S.; Yang, H. *J Colloid Interface Sci* **2011,** 361, (2), 491-496.

30. Zhang, R.; Yang, P.; Wang, Y. *J Nanopart Res* **2013,** 15, (9), 1910.

31. Binsma, J. J. M.; Bloem, L. J.; J. Bloem, J. *J Lumin* **1982,** 27, 55-72.

32. Binsma, J. J. M.; Bloem, L. J.; J. Bloem, J. *J Lumin* **1982,** 27, 35-53.

33. Nose, K.; Soma, Y.; Omata, T.; Otsuka-Yao-Matsuo, S. *Chem Mater* **2009,** 21, (13), 2607-2613.

34. Schön, J. H.; Bucher, E. *Phys Status Solidi (a)* **1999,** 171, (2), 511-519.

35. Krustok, J.; Schön, J. H.; Collan, H.; Yakushev, M.; Mädasson, J.; Bucher, E. *J Appl Phys* **1999,** 86, (1), 364-369.

36. Krustok, J.; Raudoja, J.; Schön, J. H.; Yakushev, M.; Collan, H. *Thin Solid Films* **2000,** 361-362, 406-410.
37. Hofhuis, J.; Schoonman, J.; Goossens, A. *J Phys Chem C* **2008,** 112, (38), 15052-15059.
38. Williams, F. *Phys Status Solidi B* **1968,** 25, (2), 493-512.
39. Castro, S. L.; Bailey, S. G.; Raffaelle, R. P.; Banger, K. K.; Hepp, A. F. *J Phys Chem A* **2004,** 108, 12429-12435.
40. Zhang, W.; Zhong, X. *Inorg Chem* **2011,** 50, (9), 4065-4072.
41. Zhong, H.; Zhou, Y.; Ye, M.; He, Y.; Ye, J.; He, C.; Yang, C.; Li, Y. *Chem Mater* **2008,** 20, (20), 6434-6443.
42. Li, L.; Pandey, A.; Werder, D. J.; Khanal, B. P.; Pietryga, J. M.; Klimov, V. I. *J Am Chem Soc* **2011,** 133, (5), 1176-1179.
43. Ding, K.; Jing, L.; Liu, C.; Hou, Y.; Gao, M. *Biomaterials* **2014,** 35, (5), 1608-1617.
44. Tran, T. K. C.; Le, Q. P.; Nguyen, Q. L.; Li, L.; Reiss, P. *Advances in Natural Sciences: Nanoscience and Nanotechnology* **2010,** 1, (2), 025007.
45. Chen, B.; Zhong, H.; Zhang, W.; Tan, Z. a.; Li, Y.; Yu, C.; Zhai, T.; Bando, Y.; Yang, S.; Zou, B. *Adv Funct Mater* **2012,** 22, (10), 2081-2088.
46. Kim, Y.-K.; Ahn, S.-H.; Chung, K.; Cho, Y.-S.; Choi, C.-J. *J Mater Chem* **2012,** 22, (4), 1516-1520.
47. Cichy, B.; Bednarkiewicz, A.; Strek, W. *J Opt* **2013,** 15, (8), 085303.
48. Omata, T.; Nose, K.; Kurimoto, K.; Kita, M. *J Mater Chem C* **2014,** 2, (33), 6867-6872.
49. Cadirci, M.; Masala, O.; Pickett, N.; Binks, D. *J Chem Phys* **2014,** 438, 60-65.
50. Sun, C.; Cevher, Z.; Zhang, J.; Gao, B.; Shum, K.; Ren, Y. *J Mater Chem A* **2014,** 2, (27), 10629-10633.
51. Kraatz, I. T.; Booth, M.; Whitaker, B. J.; Nix, M. G. D.; Critchley, K. *J Phys Chem C* **2014,** 118, (41), 24102-24109.
52. Knowles, K. E.; Nelson, H. D.; Kilburn, T. B.; Gamelin, D. R. *J Am Chem Soc* **2015,** 137, (40), 13138-13147.
53. Rice, W. D.; McDaniel, H.; Klimov, V. I.; Crooker, S. A. *J Phys Chem Lett* **2014,** 5, (23), 4105-4109.
54. Whitham, P. J.; Marchioro, A.; Knowles, K. E.; Kilburn, T. B.; Reid, P. J.; Gamelin, D. R. *J Phys Chem C* **2016,** 120, (30), 17136-17142.
55. Zang, H.; Li, H.; Makarov, N. S.; Velizhanin, K. A.; Wu, K.; Park, Y. S.; Klimov, V. I. *Nano Lett* **2017,** 17, (3), 1787-1795.

56. Pons, T.; Pic, E.; Lequeux, N.; Cassette, E.; Bezdetnaya, L.; Guillemin, F.; Marchal, F.; Dubertret, B. *ACS Nano* **2010,** 4, (5), 2531-2538.
57. Hsu, J.-C.; Huang, C.-C.; Ou, K.-L.; Lu, N.; Mai, F.-D.; Chen, J.-K.; Chang, J.-Y. *J Mater Chem* **2011,** 21, (48), 19257-19266.
58. Liu, S.; Zhang, H.; Qiao, Y.; Su, X. *RSC Adv* **2012,** 2, (3), 819-825.
59. Yue, W.; Han, S.; Peng, R.; Shen, W.; Geng, H.; Wu, F.; Tao, S.; Wang, M. *J Mater Chem* **2010,** 20, (35), 7570-7578.
60. Liu, S.; Shi, F.; Zhao, X.; Chen, L.; Su, X. *Biosens Bioelectron* **2013,** 47, 379-384.
61. Chang, J. Y.; Lin, J. M.; Su, L. F.; Chang, C. F. *ACS Appl Mater Interfaces* **2013,** 5, (17), 8740-8752.
62. Sheng, X.; Wang, L.; Yang, D. *J Sol-Gel Sci Technol* **2012,** 62, (1), 87-91.
63. Wang, Y.; Jin, Z.; Liu, H.; Wang, X.; Zheng, X.; Du, H. *Powder Technol* **2012,** 232, 93-98.
64. Der Wu, J.; Ting Wang, L.; Gau, C. *Sol Energy Mater Sol Cells* **2012,** 98, 404-408.
65. Sabet, M.; Salavati-Niasari, M.; Ghanbari, D.; Amiri, O.; Yousefi, M. *Mater Sci Semicond Process* **2013,** 16, (3), 696-704.
66. Gardner, J. S.; Shurdha, E.; Wang, C.; Lau, L. D.; Rodriguez, R. G.; Pak, J. J. *J Nanopart Res* **2007,** 10, (4), 633-641.
67. Bensebaa, F.; Durand, C.; Aouadou, A.; Scoles, L.; Du, X.; Wang, D.; Le Page, Y. *J Nanopart Res* **2009,** 12, (5), 1897-1903.
68. Lee, S. J.; Kim, Y.; Jung, J.; Kim, M. A.; Kim, N.; Lee, S. J.; Kim, S. K.; Kim, Y.-R.; Park, J. K. *J Mater Chem* **2012,** 22, (24), 11957-11963.
69. Nairn, J. J.; Shapiro, P. J.; Twamley, B.; Pounds, T.; von Wandruszka, R.; Fletcher, T. R.; Williams, M.; Wang, C.; Norton, M. G. *Nano Lett* **2006,** 6, (6), 1218-1223.
70. Zhang, W.; Zeng, H.; Yang, Z.; Wang, Q. *J Solid State Chem* **2012,** 186, 58-63.
71. Xie, R.; Rutherford, M.; Peng, X. *J Am Chem Soc* **2009,** 131, (15), 5691-5697.
72. Li, S.; Chen, Y.; Huang, L.; Pan, D. *Nanotechnology* **2013,** 24, (39), 395705.
73. Chang, J.; Waclawik, E. R. *Cryst Eng Comm* **2013,** 15, (28), 5612-5619.
74. Liu, Y.; Xie, Y.; Cui, H.; Zhao, W.; Yang, C.; Wang, Y.; Huang, F.; Dai, N. *Phys Chem Chem Phys* **2013,** 15, (13), 4496-4499.
75. Niezgoda, J. S.; Harrison, M. A.; McBride, J. R.; Rosenthal, S. J. *Chem Mater* **2012,** 24, (16), 3294-3298.
76. He, J.-J.; Zhou, W.-H.; Guo, J.; Li, M.; Wu, S.-X. *Cryst Eng Comm* **2012,** 14, (10), 3638-3644.

77. Kuzuya, T.; Hamanaka, Y.; Itoh, K.; Kino, T.; Sumiyama, K.; Fukunaka, Y.; Hirai, S. *J Colloid Interface Sci* **2012,** 388, (1), 137-143.

78. Uehara, M.; Watanabe, K.; Tajiri, Y.; Nakamura, H.; Maeda, H. *J Chem Phys* **2008,** 129, (13), 134709.

79. Tang, X.; Cheng, W.; Choo, E. S.; Xue, J. *Chem Commun* **2011,** 47, (18), 5217-5219.

80. Pan, D.; Weng, D.; Wang, X.; Xiao, Q.; Chen, W.; Xu, C.; Yang, Z.; Lu, Y. *Chem Commun* **2009**, (28), 4221-4223.

81. Song, W.-S.; Kim, J.-H.; Lee, J.-H.; Lee, H.-S.; Do, Y. R.; Yang, H. *J Mater Chem* **2012,** 22, (41), 21901-21908.

82. Park, S. H.; Hong, A.; Kim, J. H.; Yang, H.; Lee, K.; Jang, H. S. *ACS Appl Mater Interfaces* **2015,** 7, (12), 6764-6771.

83. Fu, M.; Luan, W.; Tu, S.-T.; Mleczko, L. *Green Processing and Synthesis* **2016**.

84. Zhang, J.; Xie, R.; Yang, W. *Chem Mater* **2011,** 23, (14), 3357-3361.

85. Guo, W.; Chen, N.; Tu, Y.; Dong, C.; Zhang, B.; Hu, C.; Chang, J. *Theranostics* **2013,** 3, (2), 99-108.

86. De Trizio, L.; Prato, M.; Genovese, A.; Casu, A.; Povia, M.; Simonutti, R.; Alcocer, M. J. P.; D'Andrea, C.; Tassone, F.; Manna, L. *Chem Mater* **2012,** 24, (12), 2400-2406.

87. Kim, H.; Suh, M.; Kwon, B. H.; Jang, D. S.; Kim, S. W.; Jeon, D. Y. *J Colloid Interface Sci* **2011,** 363, (2), 703-706.

88. Speranskaya, E. S.; Sevrin, C.; De Saeger, S.; Hens, Z.; Goryacheva, I. Y.; Grandfils, C. *ACS Appl Mater Interfaces* **2016,** 8, (12), 7613-7622.

89. Lin, Z.; Fei, X.; Ma, Q.; Gao, X.; Su, X. *New J Chem* **2014,** 38, (1), 90-96.

90. Demillo, V. G.; Liao, M.; Zhu, X.; Redelman, D.; Publicover, N. G.; Hunter, K. W., Jr. *Colloids Surf A Physicochem Eng Asp* **2015,** 464, 134-142.

91. Speranskaya, E. S.; Beloglazova, N. V.; Abe, S.; Aubert, T.; Smet, P. F.; Poelman, D.; Goryacheva, I. Y.; De Saeger, S.; Hens, Z. *Langmuir* **2014,** 30, (25), 7567-7575.

92. Cheng, C. Y.; Ou, K. L.; Huang, W. T.; Chen, J. K.; Chang, J. Y.; Yang, C. H. *ACS Appl Mater Interfaces* **2013,** 5, (10), 4389-4400.

93. Permadi, A.; Fahmi, M. Z.; Chen, J.-K.; Chang, J.-Y.; Cheng, C.-Y.; Wang, G.-Q.; Ou, K.-L. *RSC Adv* **2012,** 2, (14), 6018-6022.

94. Kim, Y. s.; Lee, Y.; Kim, Y.; Kim, D.; Choi, H. S.; Park, J. C.; Nam, Y. S.; Jeon, D. Y. *RSC Adv* **2017,** 7, (18), 10675-10682.

95. Yong, K. T.; Roy, I.; Hu, R.; Ding, H.; Cai, H.; Zhu, J.; Zhang, X.; Bergey, E. J.; Prasad, P. N. *Integr Biol* **2010,** 2, (2-3), 121-129.

96. Liu, S. Y.; Shi, F. P.; Chen, L.; Su, X. G. *Microchim Acta* **2014,** 181, (3-4), 339-345.
97. Wang, M.; Liu, X.; Cao, C.; Wang, L. *J Mater Chem* **2012,** 22, (41), 21979-21986.
98. Chetty, S. S.; Praneetha, S.; Basu, S.; Sachidanandan, C.; Murugan, A. V. *Sci Rep* **2016,** 6, 26078.
99. Yu, K.; Ng, P.; Ouyang, J.; Zaman, M. B.; Abulrob, A.; Baral, T. N.; Fatehi, D.; Jakubek, Z. J.; Kingston, D.; Wu, X.; Liu, X.; Hebert, C.; Leek, D. M.; Whitfield, D. M. *ACS Appl Mater Interfaces* **2013,** 5, (8), 2870-2880.
100. Cassette, E.; Pons, T.; Bouet, C.; Helle, M.; Bezdetnaya, L.; Marchal, F.; Dubertret, B. *Chem Mater* **2010,** 22, (22), 6117-6124.
101. Wuister, S. F.; Swart, I.; van Driel, F.; Hickey, S. G.; de Mello Donegá, C. *Nano Lett* **2003,** 3, (4), 503-507.
102. Jara, D. H.; Yoon, S. J.; Stamplecoskie, K. G.; Kamat, P. V. *Chem Mater* **2014,** 26, (24), 7221-7228.
103. Li, T.-L.; Teng, H. *J Mater Chem* **2010,** 20, (18), 3656-3664.
104. Panthani, M. G.; Akhavan, V.; Goodfellow, B.; Schmidtke, J. P.; Dunn, L.; Dodabalapur, A.; Barbara, P. F.; Korgel, B. A. *J Am Chem Soc* **2008,** 130, (49), 16770-16777.
105. Xu, X.; Wan, Q.; Luan, C.; Mei, F.; Zhao, Q.; An, P.; Liang, Z.; Xu, G.; Zapien, J. A. *ACS Appl Mater Interfaces* **2013,** 5, (21), 10605-10613.
106. Santra, P. K.; Nair, P. V.; George Thomas, K.; Kamat, P. V. *J Phys Chem Lett* **2013,** 4, (5), 722-729.
107. Pan, Z.; Mora-Sero, I.; Shen, Q.; Zhang, H.; Li, Y.; Zhao, K.; Wang, J.; Zhong, X.; Bisquert, J. *J Am Chem Soc* **2014,** 136, (25), 9203-9210.
108. Du, J.; Du, Z.; Hu, J. S.; Pan, Z.; Shen, Q.; Sun, J.; Long, D.; Dong, H.; Sun, L.; Zhong, X.; Wan, L. J. *J Am Chem Soc* **2016,** 138, (12), 4201-4209.
109. Meinardi, F.; McDaniel, H.; Carulli, F.; Colombo, A.; Velizhanin, K. A.; Makarov, N. S.; Simonutti, R.; Klimov, V. I.; Brovelli, S. *Nat Nanotechnol* **2015,** 10, (10), 878-885.
110. Smet, P. F.; Parmentier, A. B.; Poelman, D. *J Electrochem Soc* **2011,** 158, (6), R37.
111. Marin, R.; Sponchia, G.; Riello, P.; Sulcis, R.; Enrichi, F. *J Nanopart Res* **2012,** 14, (6), 1-13.
112. Yan, X.; Li, W.; Wang, X.; Sun, K. *J Electrochem Soc* **2012,** 159, (2), H195.
113. Kim, H.; Han, J. Y.; Kang, D. S.; Kim, S. W.; Jang, D. S.; Suh, M.; Kirakosyan, A.; Jeon, D. Y. *J Cryst Growth* **2011,** 326, (1), 90-93.
114. Kim, H.; Jang, H. S.; Kwon, B. H.; Suh, M.; Youngsun, K.; Cheong, S. H.; Jeon, D. Y. *Electrochem Solid State Lett* **2011,** 15, (2), K16-K18.

115. Chen, B.; Zhou, Q.; Li, J.; Zhang, F.; Liu, R.; Zhong, H.; Zou, B. *Opt Express* **2013,** 21, (8), 10105-10110.
116. Peng, L.; Li, D.; Zhang, Z.; Huang, K.; Zhang, Y.; Shi, Z.; Xie, R.; Yang, W. *Nano Res* **2015,** 8, (10), 3316-3331.
117. Al-Ahmadi, A., *Quantum Dots - A Variety of New Applications*. inTech: 2012.
118. Gao, X.; Liu, Z.; Lin, Z.; Su, X. *Analyst* **2014,** 139, (4), 831-836.
119. Chen, C.-W.; Wu, D.-Y.; Chan, Y.-C.; Lin, C. C.; Chung, P.-H.; Hsiao, M.; Liu, R.-S. *J Phys Chem C* **2015,** 119, (5), 2852-2860.
120. Liu, S.; Hu, J.; Su, X. *Analyst* **2012,** 137, (19), 4598-604.
121. Liu, S.; Pang, S.; Na, W.; Su, X. *Biosens Bioelectron* **2014,** 55, 249-254.
122. Liu, Z.; Ma, Q.; Wang, X.; Lin, Z.; Zhang, H.; Liu, L.; Su, X. *Biosens Bioelectron* **2014,** 54, 617-622.
123. Gao, X.; Liu, X.; Lin, Z.; Liu, S.; Su, X. *Analyst* **2012,** 137, (23), 5620-5624.
124. Liu, Z.; Li, G.; Xia, T.; Su, X. *Sensors and Actuators B: Chemical* **2015,** 220, 1205-1211.
125. Liu, Z.; Su, X. *Anal Chim Acta* **2016,** 942, 86-95.
126. Zi, L.; Huang, Y.; Yan, Z.; Liao, S. *J Lumin* **2014,** 148, 359-363.
127. Zhang, Y.; Xie, C.; Su, H.; Liu, J.; Pickering, S.; Wang, Y.; Yu, W. W.; Wang, J.; Wang, Y.; Hahm, J. I.; Dellas, N.; Mohney, S. E.; Xu, J. *Nano Lett* **2011,** 11, (2), 329-332.
128. Fakhri, H.; Mahjoub, A. R.; Khavar, A. H. C. *Appl Surf Sci* **2014,** 318, 65-73.
129. Ye, C.; Regulacio, M. D.; Lim, S. H.; Xu, Q. H.; Han, M. Y. *Chem-Eur J* **2012,** 18, (36), 11258-11263.
130. Cheng, Z.; Wang, Z.; Shifa, T. A.; Wang, F.; Zhan, X.; Xu, K.; Liu, Q.; He, J. *Appl Phys Lett* **2015,** 107, (22), 223902.
131. Tsuji, I.; Kato, H.; Kudo, A. *Chem Mater* **2006,** 18, (7), 1969-1975.
132. Yuan, Y. J.; Chen, D. Q.; Huang, Y. W.; Yu, Z. T.; Zhong, J. S.; Chen, T. T.; Tu, W. G.; Guan, Z. J.; Cao, D. P.; Zou, Z. G. *Chem Sus Chem* **2016,** 9, (9), 1003-1009.
133. Mizutani, U., *Introduction to the Electron Theory of Metals*. Cambridge University Press: 2001.
134. Drude, P. *Annalen der Physik* **1900,** 306, (3), 566-613.
135. Comin, A.; Manna, L. *Chem Soc Rev* **2014,** 43, (11), 3957-3975.
136. Khlebtsov, N. G.; Dykman, L. A. *Journal of Quantitative Spectroscopy and Radiative Transfer* **2010,** 111, (1), 1-35.
137. Gonçalves, M. R. *J Phys D* **2014,** 47, (21), 213001.
138. Maier, S. A., *Plasmonic: Fundamentals and Applications*. Springer US: 2007.

139. Frohlich, H., *Theory of Dielectrics*. Oxford University Press: 1987.
140. Huang, X.; El-Sayed, M. A. *J Adv Res* **2010,** 1, (1), 13-28.
141. Link, S.; El-Sayed, M. A. *Annu Rev Phys Chem* **2003,** 54, 331-366.
142. Pérez-Hernández, M.; del Pino, P.; Mitchell, S. G.; Moros, M.; Stepien, G.; Pelaz, B.; Parak, W. J.; Gálvez, E. M.; Pardo, J.; de la Fuente, J. M. *ACS Nano* **2015,** 9, (1), 52-61.
143. Zou, L.; Wang, H.; He, B.; Zeng, L.; Tan, T.; Cao, H.; He, X.; Zhang, Z.; Guo, S.; Li, Y. *Theranostics* **2016,** 6, (6), 762-772.
144. Liu, B.; Li, C.; Cheng, Z.; Hou, Z.; Huang, S.; Lin, J. *Biomater Sci* **2016,** 4, (6), 890-909.
145. Hemmer, E.; Benayas, A.; Légaré, F.; Vetrone, F. *Nanoscale Horiz* **2016,** 1, (3), 168-184.
146. Hemmer, E.; Venkatachalam, N.; Hyodo, H.; Hattori, A.; Ebina, Y.; Kishimoto, H.; Soga, K. *Nanoscale* **2013,** 5, (23), 11339-11361.
147. Ghosh, P.; Han, G.; De, M.; Kim, C. K.; Rotello, V. M. *Adv Drug Deliv Rev* **2008,** 60, (11), 1307-1315.
148. Vigderman, L.; Khanal, B. P.; Zubarev, E. R. *Adv Mater* **2012,** 24, (36), 4811-4841.
149. Liu, Y.; Yuan, H.; Fales, A. M.; Register, J. K.; Vo-Dinh, T. *Front Chem* **2015,** 3, 51 (1-7).
150. Sebastian, V.; Lee, S. K.; Jensen, K. F. *Nanoscale* **2014,** 6, (21), 13228-13235.
151. Skrabalak, S. E.; Chen, J.; Sun, Y.; Lu, X.; Au, L.; Cobley, C. M.; Xia, Y. *Acc Chem Res* **2008,** 41, (12), 1587-1595.
152. Zhao, J.; Wallace, M.; Melancon, M. P. *Nanomedicine* **2014,** 9, (13), 2041-2057.
153. Ren, Q.-Q.; Bai, L.-Y.; Zhang, X.-S.; Ma, Z.-Y.; Liu, B.; Zhao, Y.-D.; Cao, Y.-C. *J Nanomater* **2015,** 2015, 1-7.
154. http://www.nanoseedz.com/Gold_Nanorods_en.html
155. Yuan, H.; Khoury, C. G.; Hwang, H.; Wilson, C. M.; Grant, G. A.; Vo-Dinh, T. *Nanotechnology* **2012,** 23, (7), 075102.
156. Niu, W.; Chua, Y. A.; Zhang, W.; Huang, H.; Lu, X. *J Am Chem Soc* **2015,** 137, (33), 10460-10463.
157. Zhang, Y. S.; Wang, Y.; Wang, L.; Wang, Y.; Cai, X.; Zhang, C.; Wang, L. V.; Xia, Y. *Theranostics* **2013,** 3, (8), 532-543.
158. Tan, L.; Chen, D.; Liu, H.; Tang, F. *Adv Mater* **2010,** 22, (43), 4885-4889.
159. Priyadarshini, E.; Pradhan, N. *Sens Actuators B: Chemical* **2017,** 238, 888-902.
160. Li, T.; Zhu, K.; He, S.; Xia, X.; Liu, S.; Wang, Z.; Jiang, X. *Analyst* **2011,** 136, (14), 2893-2896.
161. Xu, P.; Li, R.; Tu, Y.; Yan, J. *Talanta* **2015,** 144, 704-709.

162. Liu, A.; Dong, W.; Liu, E.; Tang, W.; Zhu, J.; Han, J. *Electrochim Acta* **2010,** 55, (6), 1971-1977.

163. Nietzold, C.; Lisdat, F. *Analyst* **2012,** 137, (12), 2821-2826.

164. Valentini, P.; Pompa, P. P. *RSC Adv* **2013,** 3, (42), 19181-19190.

165. Fabris, L. *J Opt* **2015,** 17, (11), 114002.

166. Li, X.; Robinson, S. M.; Gupta, A.; Saha, K.; Jiang, Z.; Moyano, D. F.; Sahar, A.; Riley, M. A.; Rotello, V. M. *ACS Nano* **2014,** 8, (10), 10682-10686.

167. Atwater, H. A.; Polman, A. *Nat Mater* **2010,** 9, (3), 205-213.

168. Meyers, J. D.; Cheng, Y.; Broome, A. M.; Agnes, R. S.; Schluchter, M. D.; Margevicius, S.; Wang, X.; Kenney, M. E.; Burda, C.; Basilion, J. P. *Part Part Syst Charact* **2015,** 32, (4), 448-457.

169. Torchilin, V. P. *Handb Exp Pharmacol* **2010**, (197), 3-53.

170. Gamaleia, N. F.; Shton, I. O. *Photodiagnosis Photodyn Ther* **2015,** 12, (2), 221-231.

171. Dolmans, D. E.; Fukumura, D.; Jain, R. K. *Nat Rev Cancer* **2003,** 3, (5), 380-387.

172. Hainfeld, J. F.; Dilmanian, F. A.; Slatkin, D. N.; Smilowitz, H. M. *J Pharm Pharmacol* **2008,** 60, (8), 977-985.

173. Li, W.; Chen, X. *Nanomedicine* **2015,** 10, (2), 299-320.

174. Goble, R. J. *Can Mineral* **1985,** 23, 61-76.

175. Di Benedetto, F.; Borgheresi, M.; Caneschi, A.; Chastanet, G.; Cipriani, C.; Gatteschi, D.; Pratesi, G.; Romanelli, M.; Sessoli, R. *Eur J Mineral* **2006,** 18, (3), 283-287.

176. Mazin, I. I. *Phys Rev B* **2012,** 85, (11), 115133.

177. Douglas, B. *J Chem Educ* **2009,** 86, (8), 980-984.

178. Zhao, Y. X.; Pan, H. C.; Lou, Y. B.; Qiu, X. F.; Zhu, J. J.; Burda, C. *J Am Chem Soc* **2009,** 131, (12), 4253-4261.

179. Luther, J. M.; Jain, P. K.; Ewers, T.; Alivisatos, A. P. *Nat Mater* **2011,** 10, (5), 361-366.

180. Xie, Y.; Carbone, L.; Nobile, C.; Grillo, V.; D'Agostino, S.; Della Sala, F.; Giannini, C.; Altamura, D.; Oelsner, C.; Kryschi, C.; Cozzoli, P. D. *ACS Nano* **2013,** 7, (8), 7352-7369.

181. Wang, S.; Riedinger, A.; Li, H.; Fu, C.; Liu, H.; Li, L.; Liu, T.; Tan, L.; Barthel, M. J.; Pugliese, G.; De Donato, F.; Scotto D'Abbusco, M.; Meng, X.; Manna, L.; Meng, H.; Pellegrino, T. *ACS Nano* **2015,** 9, (2), 1788-1800.

182. Liu, J.; Xue, D. *J Mater Chem* **2011,** 21, (1), 223-228.

183. Ding, C.; Zhong, H.; Zhang, S. *Biosens Bioelectron* **2008,** 23, (8), 1314-1318.

184. Viswanathan, S.; Rani, C.; Ho, J. A. *Talanta* **2012,** 94, 315-319.

185. Blanco, E.; Shen, H.; Ferrari, M. *Nat Biotechnol* **2015,** 33, (9), 941-951.

186. Partain, L. D.; McLeod, P. S.; Duisman, J. A.; Peterson, T. M.; Sawyer, D. E.; Dean, C. S. *J Appl Phys* **1983,** 54, (11), 6708-6720.

187. Li, Y.; Lu, W.; Huang, Q.; Huang, M.; Li, C.; Chen, W. *Nanomedicine* **2010,** 5, (8), 1161-1171.

188. Tian, Q.; Jiang, F.; Zou, R.; Liu, Q.; Chen, Z.; Zhu, M.; Yang, S.; Wang, J.; Wang, J.; Hu, J. *ACS Nano* **2011,** 5, (12), 9761-9771.

189. Tian, Q.; Tang, M.; Sun, Y.; Zou, R.; Chen, Z.; Zhu, M.; Yang, S.; Wang, J.; Wang, J.; Hu, J. *Adv Mater* **2011,** 23, (31), 3542-3547.

190. Tan, L.; Wu, Z.; Wang, X.; Sun, J. *RSC Adv* **2015,** 5, (44), 35317-35324.

191. Wolf, A.; Kodanek, T.; Dorfs, D. *Nanoscale* **2015,** 7, (46), 19519-19527.

192. Ku, G.; Zhou, M.; Song, S. L.; Huang, Q.; Hazle, J.; Li, C. *Acs Nano* **2012,** 6, (8), 7489-7496.

193. Ding, K.; Zeng, J.; Jing, L.; Qiao, R.; Liu, C.; Jiao, M.; Li, Z.; Gao, M. *Nanoscale* **2015,** 7, (25), 11075-11081.

194. Mary, K. A. A.; Unnikrishnan, N. V.; Philip, R. *APL Materials* **2014,** 2, (7), 076104.

195. Huang, Y.; Lai, Y.; Shi, S.; Hao, S.; Wei, J.; Chen, X. *Chem Asian J* **2015,** 10, (2), 370-376.

196. Liu, Z.; Cheng, L.; Zhang, L.; Yang, Z.; Liu, Z.; Fang, J. *Biomaterials* **2014,** 35, (13), 4099-4107.

197. Cole, J. R.; Mirin, N. A.; Knight, M. W.; Goodrich, G. P.; Halas, N. J. *J Phys Chem C* **2009,** 113, (28), 12090-12094.

198. Li, B.; Wang, Q.; Zou, R.; Liu, X.; Xu, K.; Li, W.; Hu, J. *Nanoscale* **2014,** 6, (6), 3274-3282.

199. Pattani, V. P.; Tunnell, J. W. *Lasers Surg Med* **2012,** 44, (8), 675-84.

200. Liu, Y.; Ai, K.; Liu, J.; Deng, M.; He, Y.; Lu, L. *Adv Mater* **2013,** 25, (9), 1353-1359.

201. Huang, P.; Lin, J.; Li, W.; Rong, P.; Wang, Z.; Wang, S.; Wang, X.; Sun, X.; Aronova, M.; Niu, G.; Leapman, R. D.; Nie, Z.; Chen, X. *Angew Chem Int Ed Engl* **2013,** 52, (52), 13958-64.

202. Hessel, C. M.; Pattani, V. P.; Rasch, M.; Panthani, M. G.; Koo, B.; Tunnell, J. W.; Korgel, B. A. *Nano Lett* **2011,** 11, (6), 2560-6.

203. Liu, M.; Xue, X.; Ghosh, C.; Liu, X.; Liu, Y.; Furlani, E. P.; Swihart, M. T.; Prasad, P. N. *Chem Mater* **2015,** 27, (7), 2584-2590.

204. Liu, Z.; Liu, X.; Du, Y.; Ren, J.; Qu, X. *ACS Nano* **2015,** 9, (10), 10335-46.

205. Cheung, T. L.; Hong, L.; Rao, N.; Yang, C.; Wang, L.; Lai, W. J.; Chong, P. H.; Law, W. C.; Yong, K. T. *Nanoscale* **2016,** 8, (12), 6609-6622.

206. Xiao, Q.; Zheng, X.; Bu, W.; Ge, W.; Zhang, S.; Chen, F.; Xing, H.; Ren, Q.; Fan, W.; Zhao, K.; Hua, Y.; Shi, J. *J Am Chem Soc* **2013,** 135, (35), 13041-13048.

207. Lv, R.; Yang, P.; Hu, B.; Xu, J.; Shang, W.; Tian, J. *ACS Nano* **2017,** 11, (1), 1064-1072.

208. Lu, F.; Wang, J.; Yang, L.; Zhu, J. J. *Chem Commun* **2015,** 51, (46), 9447-9450.

209. Han, L.; Zhang, Y.; Chen, X.-W.; Shu, Y.; Wang, J.-H. *J Mater Chem B* **2016,** 4, (1), 105-112.

210. Zhou, D.; Liu, D.; Xu, W.; Yin, Z.; Chen, X.; Zhou, P.; Cui, S.; Chen, Z.; Song, H. *ACS Nano* **2016,** 10, (5), 5169-5179.

# Chapter 2

## *Synthesis of mercaptosilane-passivated CIS QDs*

*The possibility of preparing high quality QDs readily dispersible in a variety of solvents is highly desirable for photovoltaic and LED technologies, to name a few. In particular, the use of CIS QDs in these fields is steadily increasing, due to their appealing heavy-metal free nature and good performances. This fact makes the research about new synthetic protocols a hot topic. In this chapter, I present a synthetic approach to produce CIS QDs easily dispersible in organic polar solvents. 3-mercaptopropyl trimethoxysilane (MPTS) acts at the same time as solvent, sulfur source, and capping agent during the synthesis. Comparing the results of morphological, chemical, and optical characterization, we observed evidences of a growth mechanism involving populations having discrete sizes: a behavior that, to the best of our knowledge, is not yet reported in the literature for CIS QDs. These QDs possess a maximum photoluminescence quantum yield (PLQY) of more than 6 % without any substantial adjustment of the reaction conditions. The possibility of dispersing the QDs in highly polar organic solvents represents a valuable feature of this system in view of the development of new devices: for instance, polymeric films could be produced using matrixes which have not been exploited so far due to the lack of compatibility with the solvents in which the QDs are usually suspended.*

## 2.1 Materials and methods

### 2.1.1 Chemicals

CuBr (98%, Aldrich), In(OAc)$_3$ (99.999%, Sigma-Aldrich), DEG (99.9%, Sigma-Aldrich), MPTS (95%, Aldrich), NH$_3$ (28%, Fluka), ethanol (99.8%, Fluka), acetone (99.5%, Sigma-Aldrich), TEOS (98%, Aldrich) are of chemical grade and were used without further purification.

### 2.1.2 Synthesis of MPTS-passivated CIS QDs

To synthesize CIS QDs, the precursor salts (0.2 mmol of CuBr and 0.2 mmol of In(OAc)$_3$) were mixed with MPTS (5 mL) at room temperature. Then, the temperature was raised to 120 °C and the reaction mixture was kept under stirring for 15 min in order to allow the complete dissolution of the salts under N$_2$. The solution became transparent and slightly yellow. Afterwards, the reaction mixture was heated to the target temperature (180 °C, 190 °C, or 200 °C) within 30 min. The timing was initiated as soon as the temperature inside the flask reached 180 °C. At this temperature the solution started becoming more intense in color. The solution color changed progressively from yellow to orange, then red, and finally brown. Aliquots were removed at predetermined time intervals of 30, 60, 90, 120, 180, 240, and 300 min. After 360 min, the flask was quenched in cold water. The samples were purified by dispersing the QDs in chloroform and subsequently precipitating them with ethanol. After collecting QDs by means of centrifugation, they were re-dispersed in chloroform or in an organic solvent such as acetone, dimethylsulphoxide (DMSO), or tetrahydrofurane (THF) in the presence of small volumes of mercaptoethanol. The samples were named according to their reaction temperatures as C180, C190, and C200.

We further synthesized four additional batches following an analogous approach, which involves the use of 15 mL of diethylene glycol (DEG) as the main solvent along with 2 mL of MPTS. The synthesis was conducted at different temperatures and the samples were again named after their respective reaction temperature as $C_{DEG}190$, $C_{DEG}200$, $C_{DEG}210$, and $C_{DEG}220$.

### 2.1.3 Characterization techniques

**Structure, morphology, and composition.** The microstructure of the samples was investigated by means of X-Ray Powder Diffraction (XRPD) using a Philips diffractometer with a PW 1319 goniometer with a Bragg-Brentano geometry, connected to a highly-stabilized generator (40 kV). A focusing graphite monochromator and a proportional counter with a pulse-height discriminator were used, employing a nickel-filtered Cu $K\alpha$ radiation and a step-by-step technique (steps of 0.05 in 2θ), with a collection time of 10 sec step$^{-1}$. The Fourier Transform Infrared (FTIR) spectra were recorded with a NEXUS-FT-IR instrument implementing a Nicolet AVATAR Diffuse Reflectance accessory, using a resolution of 1 cm$^{-1}$ and averaging the spectrum 56 times. The chemical composition of the samples was studied by means of inductively coupled plasma mass spectroscopy (ICP-MS) measurements, utilizing a PerkinElmer Elan6100 instrument. The samples were weighed and digested with a solution of 3 mL $H_2O$, 3 mL aqua regia ($HNO_3$:HCl = 1:3), and 1.5 mL HF. The mixture was subjected to two microwave digestion cycles (CEM discover SPD): after the first cycle 7.5 mL $H_2BO_4$ was added to neutralize HF. The solution was eventually filtered and diluted to 1:5 with a 2%$_{aq}$ $HNO_3$. Cu+ and $In^{3+}$ were quantified monitoring Cu (63 and 65 m/z) and In (115 m/z) channels. Scanning Transmission Electron Microscopy (STEM) was performed with an FEI Tecnai F20 instrument, equipped with a Schottky emitter and operated at 200 keV in High Angle Annular Dark Field (HAADF) Scanning Transmission (STEM) mode. Energy Dispersive X-ray (EDX) spectrometry analysis was performed by means of a Si-Li EDAX Phoenix spectrometer equipped with an ultra-thin window detector. The surface chemical composition was investigated by means of X-ray Photolectron Spectroscopy (XPS), using a PHI 5600-ci spectrometer (Physical Electronics, Eden Prairie, MN). The main XPS chamber was maintained at a base pressure of < 8*10$^{-9}$ Torr. A standard aluminium X-ray source (Al kα = 1486.6 eV) was used to record survey spectra (1400-0 eV, 10min) and a standard magnesium source was used for high resolution spectra, both without charge neutralization. The detection angle was set at 45º with respect to the normal of the surface and the analysed area was 0.05 cm$^2$.

**Optical properties.** Aliquots sampled during the QD growth were dispersed in acetone without further purification prior to optical analyses. Photoluminescence (PL) and lifetime (LT) measurements were performed on a Horiba-Jobin Yvon Fluorolog 3-

21 spectrofluorimeter. A Xenon arc lamp (450 W) was used as a continuous-spectrum source to record the PL spectra, selecting the excitation wavelength with a double Czerny-Turner monochromator. The spectra were recorded with 1 nm band pass resolution at room temperature, diluting the QDs to an optical density below 0.1 at the excitation wavelength (390 nm) in order to minimize self-absorption phenomena. LT measurements were conducted at room temperature under excitation at 373 nm using a NanoLed light source. The detection system consisted of an iHR300 single grating monochromator coupled to a R928 Hamamatsu photomultiplier tube. We measured the PLQY using an aqueous solution of $Ru(bpy)_3Cl_2$ as a standard (emission peak: 613 nm, PLQY = 0.042 ± 0.002)[1].

## 2.2 Results and discussion

### 2.2.1 Structural, morphological, and chemical characterization

CIS QDs synthesized in this study were characterized from a structural, morphological, and compositional point of view in order to correlate these physical features with their optical properties. We report here the characterization of the sample C200 reacted for 360 min, which is representative of the entire series. The QDs have a tetragonal (*I-42d*) chalcopyrite (PDF #00-047-1372) crystalline structure, as confirmed by their diffractogram (Figure 2.1a). It must be mentioned that the $CuInS_2$ zinc-blende polymorph has an ion arrangement that is identical to the chalcopyrite one. This makes it substantially impossible to unambiguously assign the crystal structure directly from the diffractogram, due to the small difference between the two polymorphs (see Figure 2.1c) and the broad reflections. Nonetheless, the TEM observations provide additional evidence for the assignment of the crystalline phase. Indeed, the QDs are small (2.2 ± 0.3 nm) and have a tetrahedral morphology (Figures 2.1d and 2.1e). This habitus is typical of QDs crystallized in the chalcopyrite polymorph[2], as can be observed in the inset of Figure 2.1e. The EDS measurement (Figure 2.1f), performed on the area of Figure 2.1e, returns all the expected elements (Cu, In, S, and Si). ICP-MS measurements allowed for the accurate determination of the QD composition: the three batches are all Cu-deficient, with a Cu/In ratio of 0.52, 0.47, and 0.49, respectively, for the samples C180, C190, and C200.

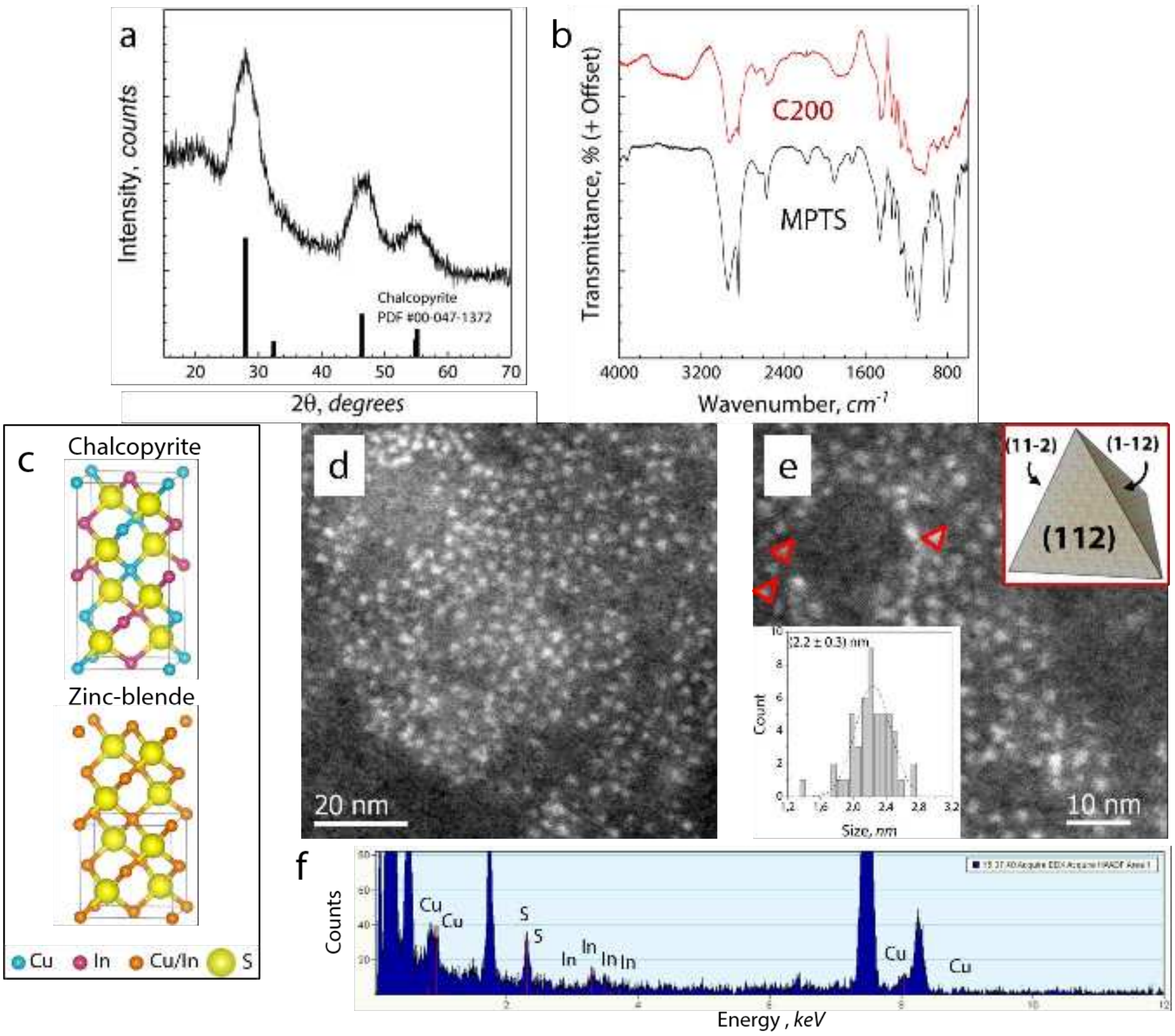

**Figure 2.1.** Synthesized CIS QDs have a tetragonal crystalline structure according to the XRPD patterns (*a*), although the cubic polymorph (*c*) could not be excluded *a priori*. FTIR analysis (*b*) confirms the presence of MPTS molecules on the QD surface. TEM observations performed on the sample synthesized at 200 °C for 360 min show a sample composed of QDs with a mean size of approximately 2.2 nm and a tetragonal habitus, characteristic of the tetragonal chalcopyrite polymorph (*d, e*, and insets). The EDX spectrum recorded for this sample returns the expected elements for the QDs and the molecules on their surface, silicon being the strong signal just below 2 keV (*f*).

---

These results are an indication of the stronger reactivity of $In^{3+}$ in the reaction environment, probably due to the poor affinity of the thiol ligands (soft Lewis bases) with $In^{3+}$ (strong Lewis acid), giving rise to an imbalanced availability of the two cations. These thiolated silica precursor molecules (MPTS) remains bound on the QD surface after the reaction, imparting colloidal stability. We ascertained the presence of MPTS molecules on the QD surface by means of FTIR spectroscopy (Figure 2.1b).

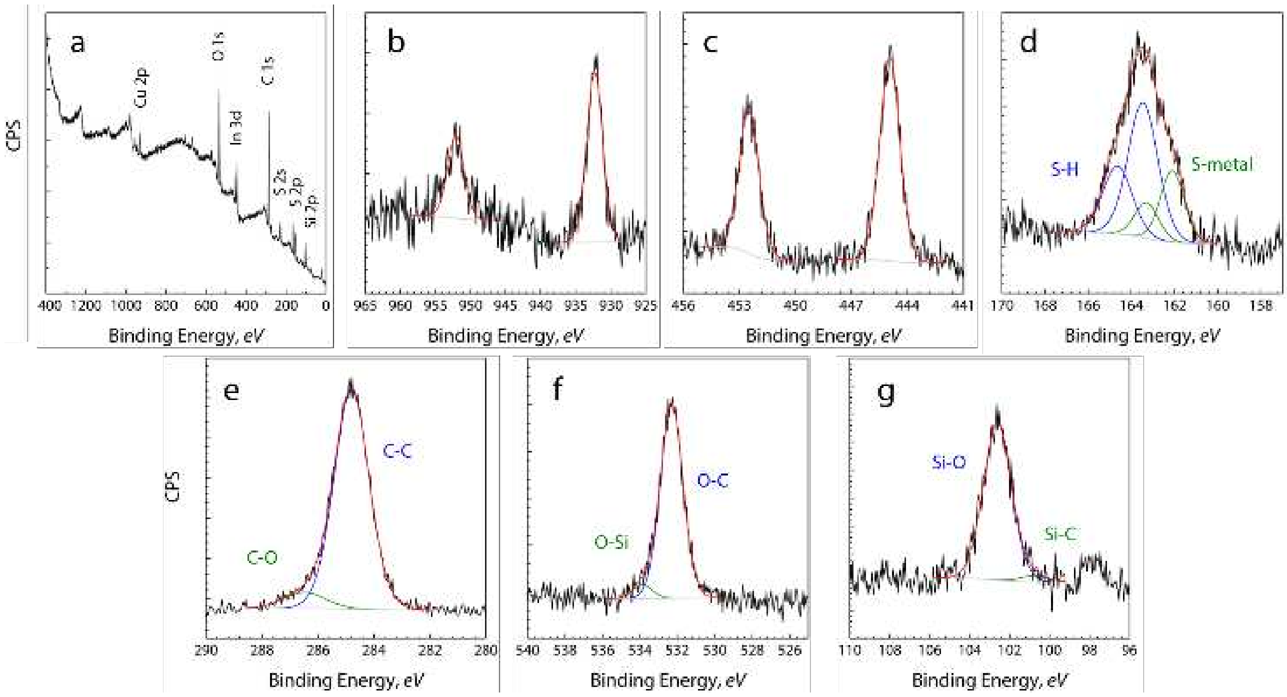

**Figure 2.2.** XPS survey spectrum (*a*) shows all the elements of interest. The high resolution spectra of Cu (*b*), In (*c*), S (*d*), C (*e*), O (*f*), and Si (*g*) were analyzed and the results are reported in Table 2.1. The metal ions are present as a single species, while sulfur is found both as thiol and as metal sulfide. In the spectra of C, O, and Si signal attributable to MPTS molecules are present.

To better investigate the surface chemistry of the sample, XPS measurements were conducted (Figure 2.2). The survey spectrum shows the presence of all the elements of interest. Both Cu$^+$ and In$^{3+}$ signals can be fitted considering a single metal population. More information can be obtained from the spectrum of sulfur, where the fit returns the presence of two populations. The first one, whose S2p$_{1/2}$ peak is centered at 162.1 eV, is ascribed to metal sulfide; the second one, whose S2p$_{1/2}$ peak is centered at 163.5 eV, stems from alkyl thiol groups[3]. The signal from the latter population is 2.6 times more intense than the one from sulfide, suggesting the presence of a considerable amount of MPTS molecules in the sample. In the spectrum of carbon, typical signals of C-C and C-O are observed but their intensity is high enough to stem not only from adventitious carbon. Indeed, MPTS contains both C-containing chemical groups. The oxygen signal has a dominant C-O component, but a minor contribution centered at higher energy results from siloxane bonds. The silicon peak is fitted considering both Si-O and Si-C contributions, the signal originating from the latter population being far weaker than the one arising from siloxane bonds.

**Table 2.1.** Summary of the results obtained from XPS data elaboration.

| ***Signal*** | ***Peak position (eV)*** | ***Peak assignment*** | ***Relative percentage*** | ***Atomic percentage*** |
|---|---|---|---|---|
| C 1s | 284.8 | C-C | 91.9 % | 59.0 % |
| | 286.5 | C-O | 8.1 % | |
| O 1s | 532.3 | O-C | 94.1 % | 20.7 % |
| | 533.9 | Si-O | 5.9 % | |
| Cu 2p | 932.3 | Cu | - | 1.3 % |
| In 3d | 452.5 | In | - | 1.5 % |
| S 2s | 162.1 | S-metal | 29.6 % | 7.8 % |
| | 163.5 | SH thiol | 70.4 % | |
| Si 2p | 100.8 | Si-C | 3.7 % | 9.8 % |
| | 102.6 | Si-O | 96.3 % | |

In general, the atomic composition obtained from this analysis suggests the presence of a large amount of MPTS molecules (composed by the elements C, O, and S) with respect to the metals (In and Cu) (Table 2.1). The presence of silica precursor molecules is even more appreciable in the samples synthesized in the presence of DEG, probably due to condensation phenomena taking place among the molecules during the reaction. In this case, the sample $C_{210}$DEG was selected as representative of the whole series. The FTIR spectrum of the QDs after purification shows the presence of a large quantity of DEG, which remains bound on the surface of the dots (Figure 2.3a). We subjected the sample to two steps of calcination (2 h and 8 h at 300 °C), observing that the glycol DEG is gradually removed during the calcination, and the typical stretches of amorphous silica appear. The diffractogram of the sample (Figure 2.3b) shows a substantially amorphous structure. When $C_{DEG}$210 is subjected to the first calcination step, weak reflections appear in correspondence of the characteristic peaks of the chalcopyrite polymorph. Moreover, the amorphous feature at low angles shifts and broadens resembling the feature usually observed in amorphous silica. This is due to the induced oxidation of silica precursor molecules, which results in the formation of a silica matrix. TEM observations confirm the presence in the sample of a significant amount of glycol and MPTS that remains bound even after the purification step (Figure 2.3c). From the micrograph it is possible to appreciate the formation of a thick polymeric layer on the grid that prevents us to observe the presence of any nanoparticle (whose size is expected to be even smaller than the one of C200 sample, according to XRPD and optical studies).

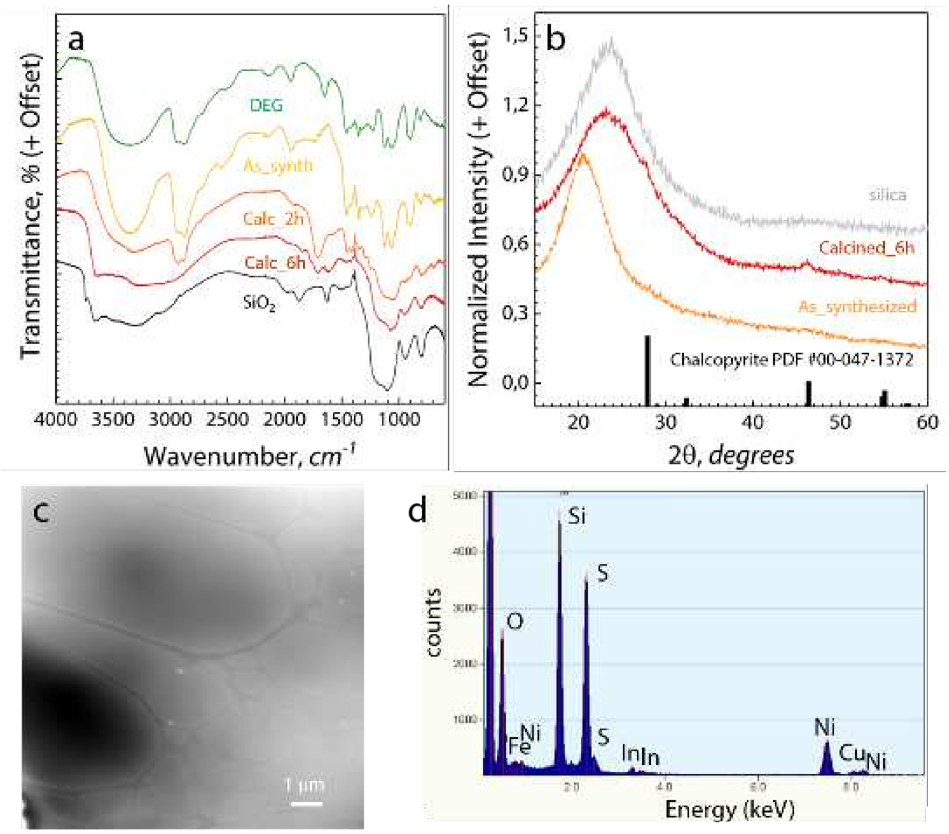

**Figure 2.3.** Structural and morphological characterization of the sample CDEG210. The FTIR spectra (*a*) show that both DEG and MPTS remain bound to the QD surface and after a prolonged calcination step the surface chemistry of the sample closely resembles that of silica. Similar observations can be obtained from XRPD patterns (*b*), the calcination shows to promote the crystallization of the QDs and the formation of a silica matrix. The considerable amount of organic molecule can be observed in the TEM micrograph in *c*, and a EDX analysis (*d*) performed on that area returns the presence of the expected elements (O, Si, In, Cu, S).

The EDX analysis performed on the area of the micrograph shows indeed the presence of a large amount of silicon and sulfur beside oxygen, elements that are found in DEG and MPTS molecules (Figure 2.3d).

### 2.2.2 Optical characterization

The optical behavior of CIS QDs can be interpreted in the light of the results discussed above. Here, the results obtained for the series synthesized in the presence of MPTS are discussed first. The considerations that we will draw for these samples are then used to interpret the very similar behavior displayed by CIS QDs synthesized in the presence of both DEG and MPTS.

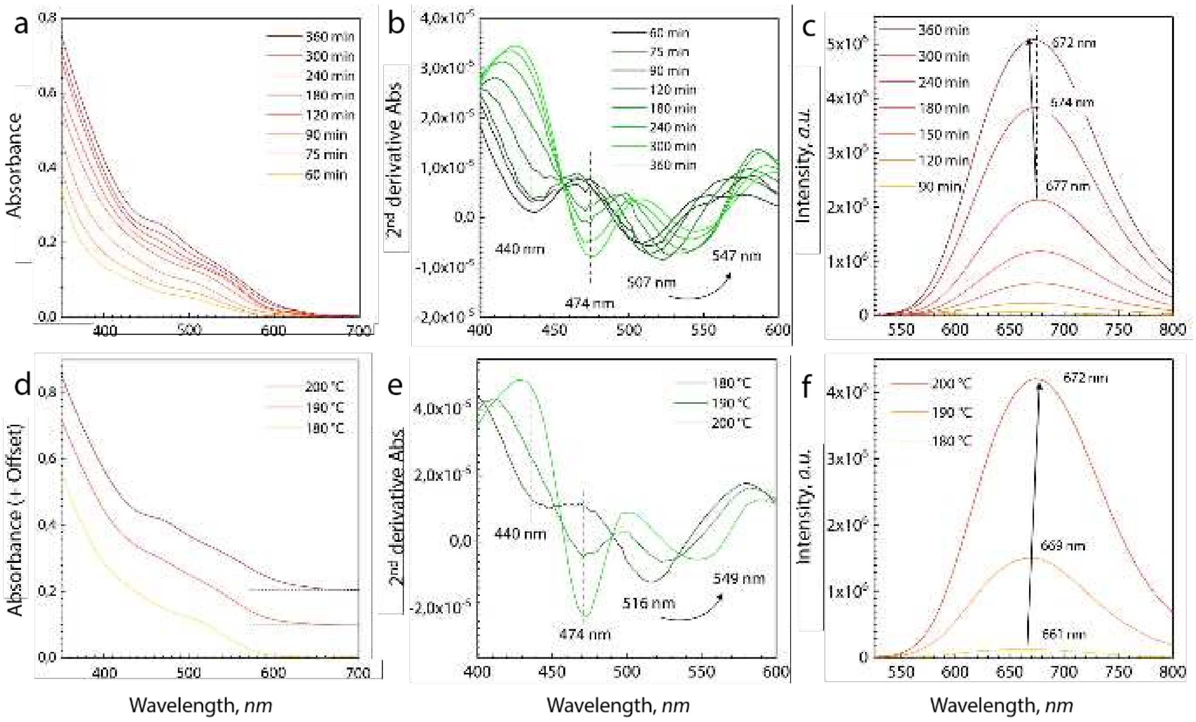

**Figure 2.4.** The absorption onset of the sample C200 shifts to longer wavelengths with increasing reaction time (*a*). Multiple excitonic features are unveiled using the second derivative of the absorption spectra (*b*). Two features have a fixed energy (440 nm and 474 nm), while a third one shifts as the reaction proceeds. The emission profile experiences a slight hypsochromic shift after 180 min of reaction (*c*), a behavior that cannot be explained according to the quantum size effect. The reaction temperature acts in a similar way as the reaction time: the higher the reaction temperature, the more red-shifted the absorption features (*d* and *e*). Analogously, the position of the emission profile follows the trend of the reaction temperature (*f*).

The absorption spectra of the QDs produced using only MPTS show multiple weak features (Figures 2.4a and 2.4d), with a band gap onset far below the tabulated value of 815 nm for the bulk material[4]. This evidence indicates the existence of a strong confinement regime, as expected from the small size of the QDs. The emission profiles are asymmetrical and rather broad, with a full width at half maximum (FWHM) of approximately 120-130 nm (Figures 2.4c and 2.4f). The PL peaks are centered between 650 and 680 nm and the Stokes shift is large (more than 100 nm). Altogether, these features usually characterize this type of QD[5-7]. The effect of the reaction time and temperature on the QD absorption properties is analogous: the absorption edge shifts towards longer wavelengths with longer reaction times due to the growth of the QDs, *i.e.* the band gap narrows. Similarly, the higher the reaction temperature, the faster the reaction kinetics, indicating a faster QD growth and consequently a more red-shifted absorption onset. Although the absorption spectrum of CIS QDs is known to be almost featureless with poorly resolved excitonic peaks[8], the use of the second derivative of the curves discloses the presence of three excitonic features (Figures 2.4b and 2.4e)[9]. The position of the two high-energy features remains unchanged in all the samples (around 440 nm and 474 nm respectively), while the third feature shifts to longer wavelengths with increasing reaction time, moving from 507 to 547 nm. The same trend was observed when varying the reaction temperature. This behavior resembles the one related to the formation of magic-sized clusters, which consists of the presence of clusters that are stable only when they are composed of a specific number of ions, *i.e.* they have a very specific size[10]. According to this interpretation, we ascribed the excitonic features to three populations of QDs simultaneously present in the sample: the features at shorter wavelengths stem from two QD populations having constant size, while the less energetic feature gradually red-shifts and stems from the presence of larger QDs. We estimated the size of these different QD populations using the effective mass approximation[11] according to the absorption properties of the samples. The band gap values were derived at the absorption onset for the population of larger QDs, while for the two other populations, the band gap was obtained extrapolating the linear part of the absorption spectrum on the low energy side of the excitonic features (centered respectively at 440 and 474 nm). From these values, we obtained a mean size of 1.6, 1.9, and 2.3 nm, respectively, for the three QD populations. These values differ at most by 0.7 nm and they all fall in the size distribution range obtained from TEM observations. Thus, unfortunately, it was not possible to obtain direct evidence of the existence of discrete QD populations from TEM micrographs. This is also due to the presence of an inevitable large quantity of molecules on the QD surface. To avoid misinterpretations of the optical features, we recorded the absorption spectra of the solvents and precursors before and after they were heated. In these spectra, no absorption features similar to the ones in the QD spectra were observed, thus corroborating our hypothesis (Figure 2.5a and 2.5b). Moreover, the QD absorption properties were tested before and after the purification step without detecting any appreciable change in the absorption spectrum, thus once more guaranteeing the absence of unreacted precursors or side-product molecules contributing at fixed wavelengths to the optical absorption of the samples (Figure 2.5c). Lifetime (LT) measurements show a PL decay rate in the hundreds of nanoseconds range (Figure 2.6).

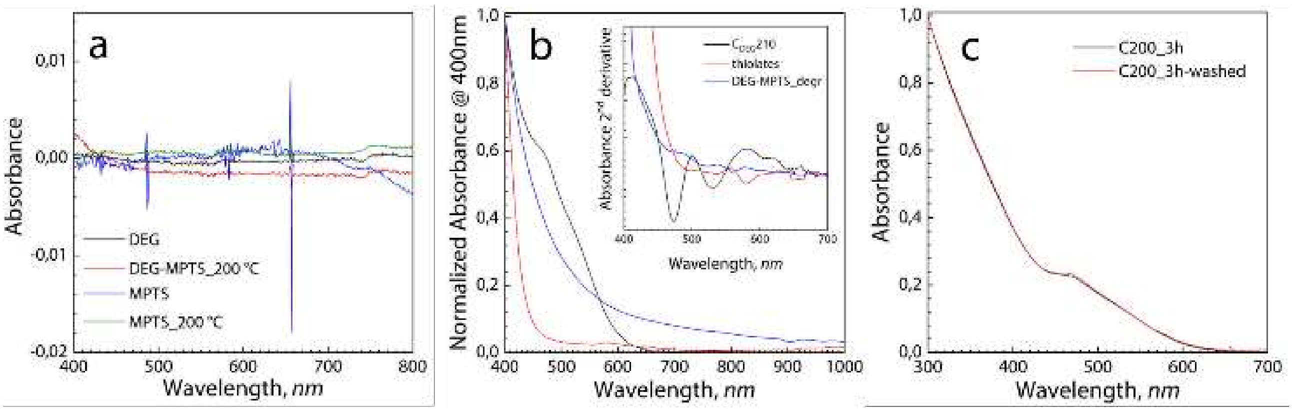

**Figure 2.5** To exclude the interference of the molecules on the observed optical properties of the QDs, the absorption spectra of different solutions containing the molecules and the chemical species involved in the reaction were recorded. In the FT-IR spectra in *a)*, it is observed that untreated MPTS and DEG have no absorption in the UV-Visible region. Moreover, when MPTS is heated in air and a DEG-MPTS mixture under $N_2$, no absorption features are observed. However, the oxidation of a DEG-MPTS mixture at high temperature determines the appearance of an increased absorption at short wavelengths. A MPTS solution of metal (copper and indium) thiolates shows similar optical properties. These spectra are compared with the one of the sample $C_{DEG}$210. The second derivative of these absorption spectra is plotted to appreciate better the difference between the different mixtures (see inset in *b*). Differently from QDs, the oxidized DEG-MPTS mixture and the metal thiolate solution do not display any local minima. Eventually, it was observed that the washing procedure does not influence the absorption properties of the sample (*c*).

The higher the reaction temperature, the longer the observed PL decay time (Figure 2.6a). Usually, LT and PLQY are directly correlated (see Table 2.2)[12]. Here, we observed that when we grew the QDs for a longer time, they possessed higher emission efficiency. This correlation comes from the fact that poorly crystallized and smaller QDs contain higher defect density and larger surface-to-volume ratio, resulting in a large number of trap states for the charge carriers. This characteristic leads to a higher probability of non-radiative decay events, which decrease the mean luminescence LT and quench the PL emission. Furthermore, to properly fit the decay curves, a triple exponential function was necessary. The fact that the exponential decay does not display a single or clear a multiple exponential behavior is an additional evidence of the presence of QDs with slightly different sizes. Nonetheless, it must be mentioned that a surface trap-related emission mechanism might contribute heavily for the faster component[13]. When the PL decay is monitored throughout the emission profile, the longer the monitored wavelength the slower the decay rate displayed (Figure 2.6b).

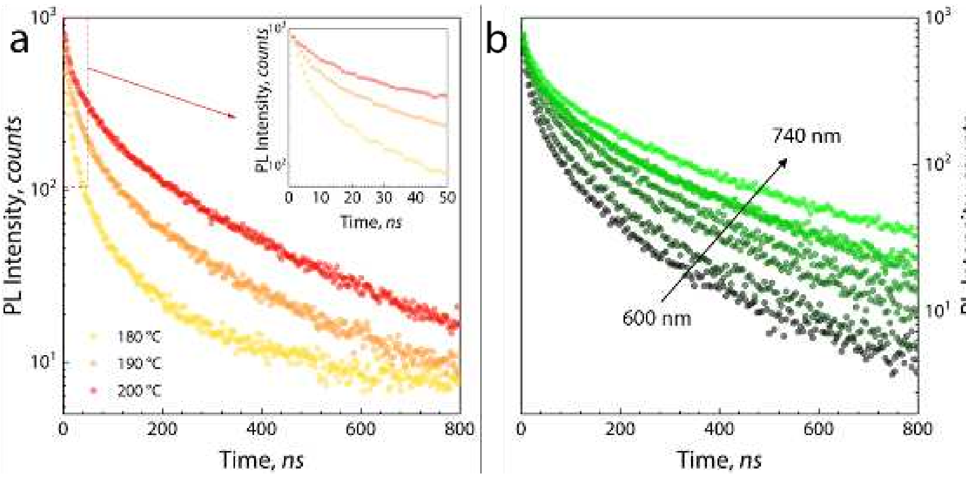

**Figure 2.6.** Lifetime measurements performed on the samples reacted at different temperatures (monitoring the emission at the PL peak maximum) show a decay time of hundreds of nanoseconds, the decay time being longer at higher reaction temperatures ($a$). The PL decay of the sample C200 is monitored throughout the emission profile ($b$): the decay time increases moving to longer wavelengths.

This last observation provides us with more evidence to interpret the optical properties of the QDs as summarized in Figure 2.7, as will become clear in the following text. Here it is useful to recall that, according to recent magneto-optical studies on CIS QDs and $Cu^+$-doped binary chalcogenide QDs[14, 15], the emission in the ternary nano-emitters arises from the creation of a photo-induced exciton. After the creation of this electron-hole couple, the delocalized hole is trapped in a $Cu^+$ level to give a $Cu^{2+}$-like acceptor state just above the VB.

**Table 2.2.** Results of the decay curves fits obtained using a triple exponential function. The decays were monitored at the maximum of the emission profile for the batches synthesized at different temperatures, while the scan of the monitored wavelength was performed on the sample C200. The PLQY was calculated comparing the QD emission with that of the standard $Ru(bpy)_3Cl_2$ (emission peak: 613 nm, PLQY = 0.042 ± 0.002).

| ***Sample Name*** | *$A_1$ (%)* | *$\tau_1$ (ns)* | *$A_2$ (%)* | *$\tau_2$ (ns)* | *$A_3$ (%)* | *$\tau_3$ (ns)* | *$\bar{\tau}$ (ns)* | *PLQY (%)* |
|---|---|---|---|---|---|---|---|---|
| C180 | 16.3 | 3.5 | 35.9 | 24.6 | 47.8 | 154 | 83.0 | 0.34 |
| C190 | 6.5 | 4.0 | 24.8 | 27.3 | 68.8 | 170 | 123.9 | 1.52 |
| C200 | 3.4 | 4.1 | 18.2 | 29.2 | 78.4 | 175 | 142.7 | 6.68 |
| ***Monitored Wavelength*** | *$A_1$ (%)* | *$\tau_1$ (ns)* | *$A_2$ (%)* | *$\tau_2$ (ns)* | *$A_3$ (%)* | *$\tau_3$ (ns)* | *$\bar{\tau}$ (ns)* | |
| 600 nm | 7.9 | 3.7 | 28.5 | 25.5 | 63.6 | 140 | 96.6 | |
| 660 nm | 3.4 | 4.1 | 18.2 | 29.2 | 78.4 | 175 | 142.7 | |
| 740 nm | 2.8 | 6.9 | 14.9 | 41.5 | 82.3 | 251 | 213.0 | |

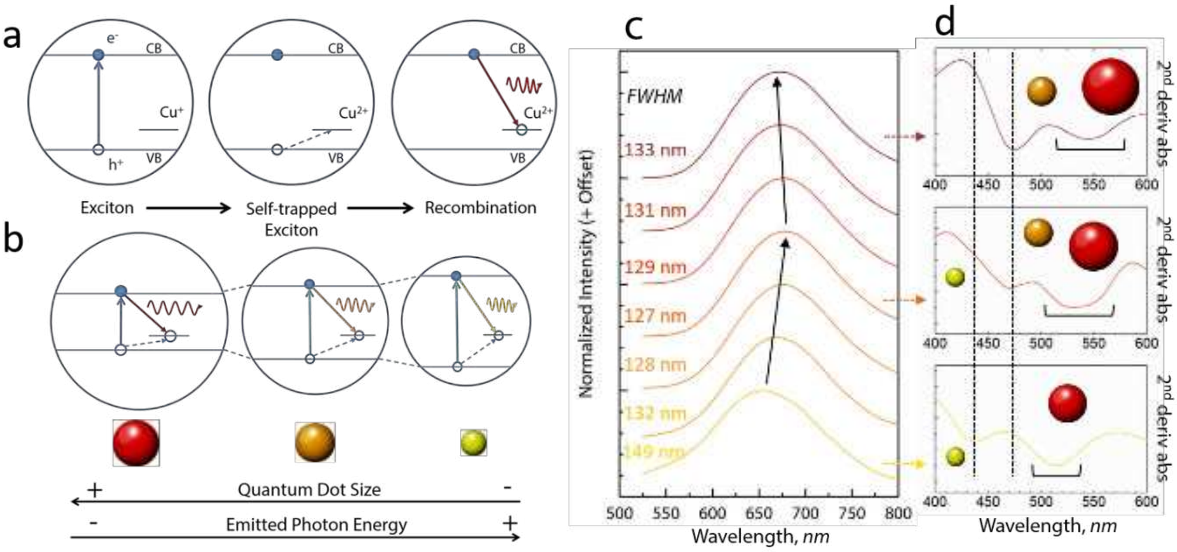

**Figure 2.7.** According to recent magneto-optical studies, the emission mechanism in CIS QDs follows a three-steps pathway (*a*): first an exciton is created by photostimulation; second, a self-trapped exciton is formed due to the trapping of the hole in a Cu$^+$ level to give a Cu$^{2+}$-like level; third, a delocalized electron recombines with the trapped hole. This last event is accompanied by the emission of a photon. Given this mechanism, the emission is size-dependent substantially in the same way as observed for usual binary QDs (*b*). In our system, the initial bathochromic shift of the emission is followed by a hypsochromic shift (*c*). If this behavior is compared with the absorption properties of the aliquots sampled at different reaction times (*d*), we can easily explain the unusual optical properties of our QDs as a consequence of the existence of three different populations. This evidence supports a growth mechanism governed by the formation of QDs having discrete sizes.

---

This trapped hole recombines with a delocalized electron that occupies a low-energy CB state. This process is accompanied by the emission of a photon (Figure 2.7a). In this scheme, the size of the QD determines the energy (*i.e.* the wavelength) of the emitted photon, since the electron-hole recombination involves CB levels (Figure 2.7b) that are affected by the quantum effect. In our samples, we observed an initial bathochromic shift of the QD emission profile followed by a hypsochromic shift (*i.e.* toward higher energies) after 180 min of reaction (Figure 2.7c). The FWHM of the emission profile follows an analogous trend: it reaches a minimum after 180 min of reaction and it broadens further extending the reaction time. Both these observations can be explained in light of the absorption measurements. According to the interpretation given above, each feature in the second derivative plot of the absorption spectra corresponds to a QD population having a slightly different size (Figure 2.7d). In particular, the ultra-small size expected for the smaller QDs (displaying the absorption at 440 nm), thus the large surface-to-volume ratio, implies very low PLQY. For this reason, the emission is dominated by the contribution of the bigger QDs. As the reaction proceeds, the population whose absorption is centered at 474 nm becomes gradually considerable, at the expense of the smaller QDs as can be deduced by the disappearance of the feature at 440 nm. A partial re-dissolution of the bigger QDs providing more building blocks in the reaction environment also cannot be excluded. The “medium-sized” QDs are large enough to have an appreciable PL contribution, which, according to the described emission mechanism, is centered at shorter wavelengths if compared to the one of the large QD population. The increased number of these “medium-sized” QDs in the reaction environment explains both the hypsochromic shift and the FWHM increase after 180 min of reaction and is consistent with the observations derived from the absorption spectra. To further corroborate our hypothesis, the increase of the mean luminescence lifetime moving from shorter to longer wavelengths indicates that the faster contributions are predominant on the high-energy side. This behavior stems from the fact that smaller QDs contribute mainly for the emission at shorter wavelengths. The observations made can be *in toto* extended to the batches of CIS QDs synthesized in the presence of DEG and MPTS at the same time. However, the optical performance of these batches are worse due to a lower crystallinity and an expected smaller size. The absorption spectra are characterized by the same multiple excitonic features observed in the discussion above (Figure 2.8a and 2.8d). Moreover, the position of these features the same observed for the other series of QDs (440 nm and 474 nm) with a third one that shifts continuously as the reaction time and temperature are increased (Figure 2.8b and 2.8e). The effect played by these two reaction parameters on the emission properties of the QDs is, again, the same as observed before, with a hypso-chromic shift of the PL peak of $C_{DEG}210$ when the reaction is allowed to proceed for more than 240 min. This effect is even more pronounced in this sample than in the sample C200. This fact is ascribed to the smaller dimensions (*i.e.* lower PLQY) of the larger population of QDs, so that the emission coming from the “medium-size” QDs (corresponding to the absorption feature centered at 474 nm) becomes more appreciable. It is worth noting that the emission peak is centered at shorter wavelengths when also DEG is present in the reaction environment. This behavior follows from the coordinating capabilities of the glycol that can effectively act as a controlling growth species.

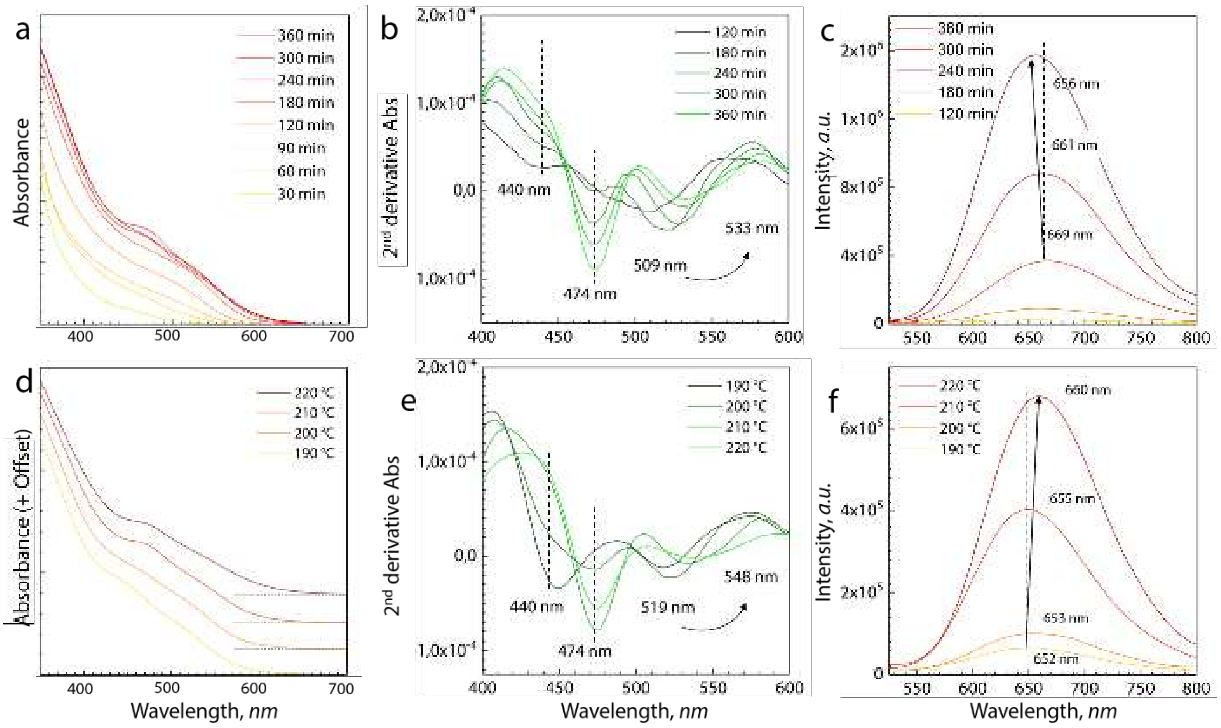

**Figure 2.8.** The optical characterization of $C_{DEG}190$, $C_{DEG}200$, $C_{DEG}210$, and $C_{DEG}220$ show an optical behavior of these samples comparable to that of the series of CIS QDs synthesized in the absence of DEG. Multiple features are present in the absorption spectra (*a* and *d*). The position of these features was revealed with the aid of the second derivative. The two high-energy features are centered at 440 nm and 474 nm respectively, while the third one continuously shifts when the reaction is prolonged for an extended time (*b*) or the reaction temperature is increased (*e*). The emission spectra of the aliquots withdrawn during the growth of the sample $C_{DEG}210$ show a hypsochromic shift after 240 min of reaction (*c*), in accordance with the observations made for the sample C200. Eventually, increasing the reaction temperature, the emission peaks appears to be centered at longer wavelengths (*f*).

The luminescence decay measurements performed on the samples $C_{DEG}190$, $C_{DEG}200$, $C_{DEG}210$, and $C_{DEG}220$ show a trend identical to the one described for the series C180, C190, C200 (Figure 2.9). When we increase the reaction temperature, the LT increases as well (Table 2.3). However, here we can observe that when the reaction temperature is increased to 220 °C, the decay is faster. This behavior derives from the fact that the MPTS boiling point is 215 °C, temperature at which the molecules start degrading. When the reaction is conducted at 220 °C, we expect that the passivating properties of the thiols are compromised, so that more superficial trap states are present. This determines the presence of more non-radiative de-excitation pathways.

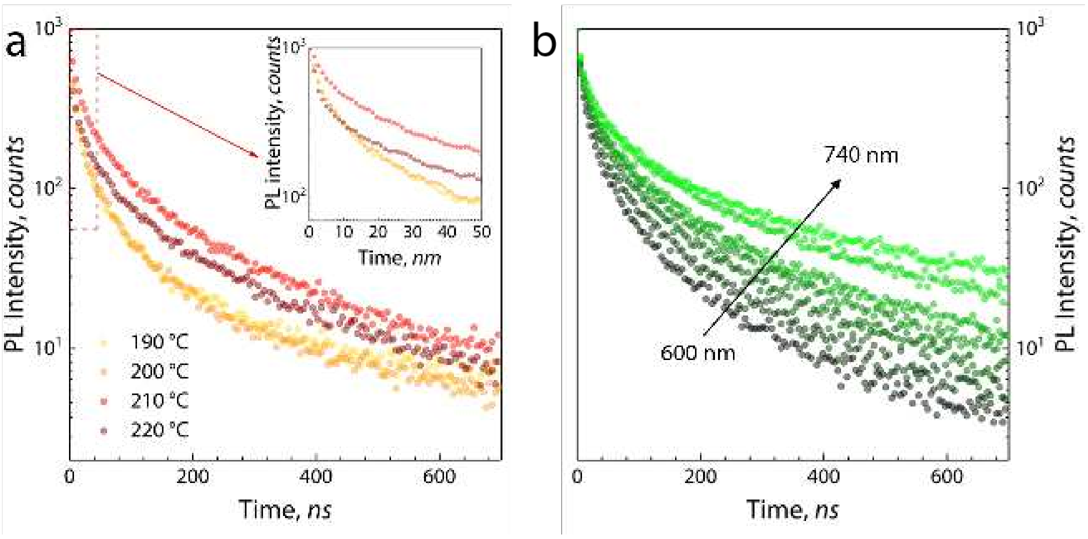

**Figure 2.9.** The characteristic PL LT of these QDs is of hundreds of nanoseconds. The decays in *a)* were recorded at the maximum of the emission peak. The scan in *b)* was performed monitoring different emission wavelengths for the sample $C_{DEG}210$.

This interpretation is supported by the observation that these QDs are not as colloidally stable as the other batches synthesized at lower temperatures, which remain stable in suspension for months after the synthesis. The slower decay observed monitoring the emission at longer wavelengths can be interpreted in the same way as described for the samples C180, C190, and C200, as arising from the presence of QDs with slightly different sizes in the same sample. In this sample even more the contribution arising from trap states on the surface and defects in the structures should heavily contribute for the fast decay component.

This being said, we believe that the reason why we could observe this previously unreported behavior is the rather slow reaction kinetics of the presented system: even after 360 min of reaction, the QDs are rather small. The addition of DEG in the reaction environment further hinders the growth of the QDs, most likely due to the strong coordinating abilities possessed by the glycol due to oxygen electron lone pairs.

### 2.2.3 Solvent effect

An alluring feature of these MPTS-passivated QDs is the possibility of dispersing them in different solvents with very diverse polarity indexes. This characteristic is very appealing when considering their possible application in the framework of device production. After the purification, C200 QDs could be easily suspended in chloroform to obtain an optically clear solution.

**Table 2.3** Results of the decay curves fits obtained using a triple exponential function. The decays were monitored at the maximum of the emission profile for the batches synthesized at different temperatures. The scan of the monitored wavelength was performed on the sample synthesized at 210 °C. The PLQY values was estimated comparing the emission of the QDs with that of the standard $Ru(bpy)_3Cl_2$. The low PLQY of these samples stems from the large surface-to-volume ratio that promotes the quenching of the luminescence.

| ***Sample Name*** | *$A_1$ (%)* | *$\tau_1$ (ns)* | *$A_2$ (%)* | *$\tau_2$ (ns)* | *$A_3$ (%)* | *$\tau_3$ (ns)* | *$\bar{\tau}$ (ns)* | *PLQY (%)* |
|---|---|---|---|---|---|---|---|---|
| $C_{DEG}$190 | 16.2 | 3.5 | 37.3 | 27.6 | 46.5 | 169 | 89.4 | 0.14 |
| $C_{DEG}$200 | 15.8 | 3.5 | 38.4 | 28.4 | 45.8 | 153 | 81.5 | 0.20 |
| $C_{DEG}$210 | 8.5 | 5.3 | 32.7 | 39.8 | 58.9 | 196 | 128.8 | 0.78 |
| $C_{DEG}$220 | 6.4 | 1.2 | 27.3 | 27.0 | 66.3 | 182 | 127.8 | 1.61 |
| ***Monitored wavelength*** | *$A_1$ (%)* | *$\tau_1$ (ns)* | *$A_2$ (%)* | *$\tau_2$ (ns)* | *$A_3$ (%)* | *$\tau_3$ (ns)* | *$\bar{\tau}$ (ns)* | |
| 600 nm | 12.6 | 3.6 | 39.3 | 28.4 | 48.1 | 141 | 79.4 | |
| 660 nm | 8.5 | 5.3 | 32.7 | 39.8 | 58.9 | 196 | 128.8 | |
| 740 nm | 7.5 | 9.8 | 31.5 | 80.1 | 61.0 | 490 | 324.9 | |

This solution can be used to obtain an aqueous dispersion of CTAB-stabilized QDs using a well-established approach[16]. A good colloidal stability to the QD colloids prepared in dimethylsulphoxide (DMSO), tetrahydrofurane (THF), and acetone could be imparted through the addition of mercaptoethanol to a final concentration of 50 mM (Figure 2.10a). These colloids display very different optical emission efficiencies; water and DMSO are the solvents that more markedly quench the emission of the QDs (Figure 2.10b). Nonetheless, the emission in all of the colloids is still clearly observable at naked eye and a test of PL stability shows that an acetone QD colloid retains 90 % of the emission intensity upon continuous irradiation for 180 min with UV light (Figure 2.11). Furthermore, as expected, we observed a solvatochromic effect in the different dispersions. It is known that an increase of the solvent polarity usually leads to a bathochromic shift of the emission of a photoluminescent species in solution[17]. This follows from more efficient solvent-related non-radiative relaxation processes. A parameter that is commonly used to describe the polarity of a solvent is the so-called Reichardt's polarity parameter $E_T(30)$, which is estimated from the outstanding negative solvatochromic properties of the dye 2,6-diphenyl-4-(2,4,6-triphenylpyridinium-1-yl)phenolate (betaine **30**)[18]. Indeed, by plotting the position of the QD PL emission maximum wavelength in the different solvents versus the polarity parameter, we could observe the existence of a linear dependence between the two parameters (Figure 2.10c).

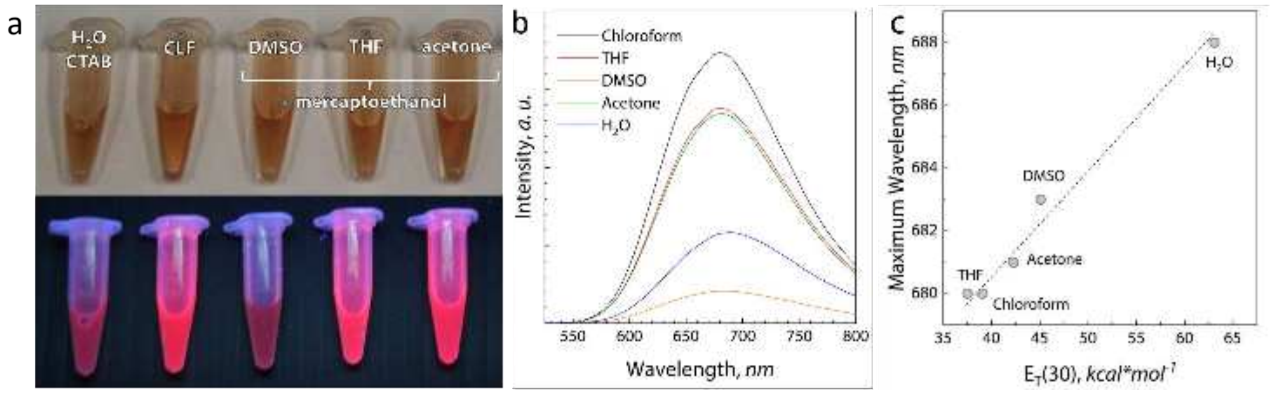

**Figure 2.10.** C200 QDs can be easily dispersed in different solvents. In (*a*) different colloids of purified QDs under day light and under UV light (366 nm) are reported, and the corresponding emission profiles under 440 nm excitation are shown in (*b*). The emission peak maximum red-shifts following the polarity of the solvent as shown in (*c*), where the wavelength of the emission peak versus the solvent Reichardt's empirical parameter is plotted.

To conclude, the observation that the QDs could be dispersed in chloroform but require the presence of an adjuvant molecule to be dispersed in oxygen-containing solvents is, to some extent, surprising. The MPTS molecules should bind to the QD surface through the thiol functional group: if this is the case, the QDs should display a large number of methoxy groups on their surface. The oxygen of these etheric groups can interact with hydroxyl groups and this interaction was recently exploited to create water-dispersible QDs[19]. In our case, QDs are not directly dispersible in water. This is an indication of a more complex surface structure where the QDs have thiol and methoxy groups on their outer surface. Actually, XPS measurements confirmed the presence of a considerable amount of MPTS molecules. This complex surface structure probably arises from both the extended reaction time and the water-sensitive nature of the MPTS molecules. The peculiarity of this reaction consists in the fact that the presence of traces of oxygen and water might promote the formation of siloxane bridges. Moreover, we could disperse these QDs in water only using a cationic surfactant, namely CTAB. This transfer method is well suited for the transfer of hydrophobic QDs. Due to this observation, we infer that the QD surface displays a larger number of thiol groups (known to impart hydrophobicity to nanoparticles[20]) than methoxy functional groups.

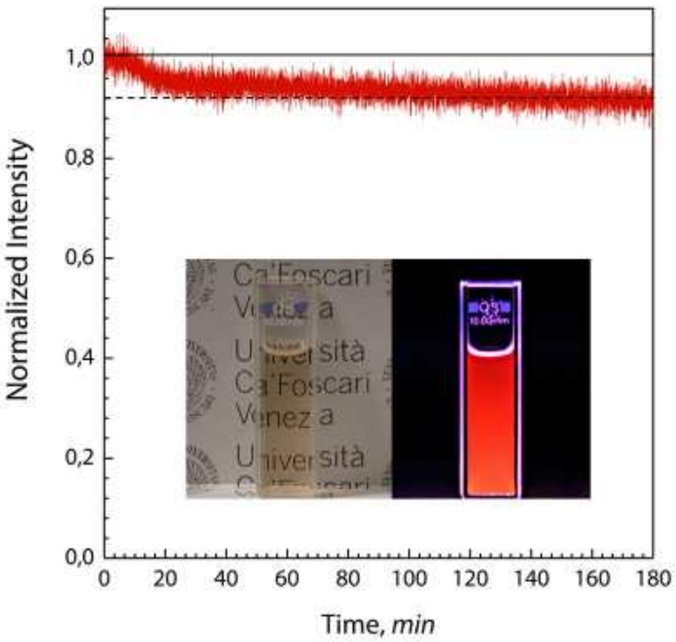

**Figure 2.11.** The PL stability test performed on an acetone colloid of the crude QDs shows a good stability of the emission of our MPTS-passivated QDs, with an overall drop of only 10 % after 3 h of illumination at 390 nm. This result highlights the good passivating capabilities of the MPTS molecules.

## 2.3 Conclusions

We have reported here the synthesis of CIS QDs using a thermal decomposition approach involving the use of MPTS. The mercaptosilane simultaneously plays the role of the chelating agent and the sulfur source. The obtained QDs are dispersible in chloroform and in a number of other oxygen-containing solvents such as acetone, THF, and DMSO retaining their characteristic PL emission. Moreover, we could disperse the QDs in water by means of CTAB passivation, a fact that highlights the hydrophobicity of their surface. The QDs have a maximum PLQY of more than 6 % and a good stability of the emission intensity under UV illumination. These characteristics make these QDs highly flexible in terms of possible applications that require dispersibility in different media and state-of-the-art optical performances (considering core-only CIS QDs). These QDs display a broad emission profile, with a FWHM of more than 100 nm, a large Stokes shift, and a tail extending to the low energy side. The comparison of TEM observations and the trend of the optical properties allowed us to postulate a growth mechanism involving populations of QDs having discrete and fixed sizes. We based this interpretation on the generally accepted emission mechanism for this type of QDs (VB-to-$Cu^+$ level transition) and a trio of experimental evidence. First, using the second derivative of the absorption spectra, we observed the presence of three absorption features: two are fixed at 440 nm and 474 nm and a third one red-shifts with the increase of the reaction time or temperature. Second, the emission profile experiences an unexpected hypsochromic shift and FWHM broadening upon prolonging the reaction time above 180 min. Third, the PL decay is slower at longer monitored wavelengths. Altogether, this evidence corroborates the presence of three populations of QDs with slightly different sizes contributing to the overall emission.

## References

1. Suzuki, K.; Kobayashi, A.; Kaneko, S.; Takehira, K.; Yoshihara, T.; Ishida, H.; Shiina, Y.; Oishi, S.; Tobita, S. *Phys Chem Chem Phys*, **2009**, 11, (42), 9850-9860.
2. Booth, M.; Brown, A. P.; Evans, S. D.; Critchley, K. *Chem Mater*, **2012**, 24, (11), 2064-2070.
3. Castner, D. G., Hinds, K.; Grainger, D. W. *Langmuir*, **1996**, 12, (21), 5083-5086.
4. Kolny-Olesiak, J.; Weller, H. *ACS Appl Mater Interfaces*, **2013**, 5, (23), 12221-12237.
5. Li, L.; Pandey, A.; Werder, D. J.; Khanal, B. P.; Pietryga, J. M.; Klimov, V. I., *J Am Chem Soc*, **2011**, 133, (5), 1176-1179.
6. Nam, D.-E.; Song, W.-S.; Yang, H. *J Mater Chem*, **2011**, 21, (45), 18220.
7. Zhang, R.; Yang, P.; Wang, Y. *J Nanopart Res*, **2013**, 15, (9), 1910.
8. Chen, B.; Zhong, H.; Zhang, W.; Tan, Z.; Li, Y.; Yu, C; Zhai, T; Bando, Y.; Yang, S.; Zou, B. *Adv Funct Mater*, **2012**, 22, (10), 2081-2088.
9. Ellingson, R. J.; Beard, M. C.; Johnson, J. C.; Yu, P.; Micic, O. I.; Nozik, A. J.; Shabaev, A.; Efros, A. L. *Nano Lett*, **2005**, 5, (5), 865-871.
10. Rogach, A. *Semiconductor Nanocrystal Quantum Dots: Synthesis, Assembly, Spectroscopy and Applications*, Springer-Verlag Wien, 2008.
11. Zhong, H.; Zhou, Y.; Ye, M.; He, Y.; Ye, J.; He, C.; Yang, C.; Li, Y. *Chem Mater*, **2008**, 20, (20), 6434-6443.
12. Orfield, N. J.; McBride, J. R.; Wang, F.; Buck, M. R.; Keene, J. D.; Reid, K. R.; Htoon, H.; Hollingsworth, J. A., Rosenthal, S. J. *ACS Nano*, **2016**, 10, (2), 1960-1968.
13. Nirmal, M.; Brus, L. *Acc Chem Res*, **1999**, 32, (5), 407-414.
14. Knowles, K. E.; Nelson, H. D.; Kilburn, T. B.; Gamelin, D. R. *J Am Chem Soc*, **2015**, 137, (40), 13138-13147.
15. Rice, W. D.; McDaniel, H.; Klimov, V. I.; Crooker, S. A. *J Phys Chem Lett*, **2014**, 5, (23), 4105-4109.

16. Kim, J.; Lee, J. E.; Lee, J.; Yu, J. H.; Kim, B. C.; An, K.; Hwang, Y.; Shin, C. H.; Park, J. G.; Kim, J.; Hyeon, T. *J Am Chem Soc*, **2006**, 128, (3), 688-689.
17. Lakowicz, J. R. *Principles of Fluorescence Spectroscopy*, Springer USA, 2006.
18. Cerón-Carrasco, J. P.; Jacquemin, D.; Laurence, C.; Planchat, A.; Reichardt, C.; Sraïdi, K. *J Phys Org Chem*, **2014**, 27, (6), 512-518.
19. Zhang, X.; Shamirian, A.; Jawaid, A. M.; Tyrakowski, C. M.; Page, L. E.; Das, A.; Chen, O.; Isovic, A.; Hassan, A.; Snee, P. T. *Small*, **2015**, 11, (45), 6091-6096.
20. Du, X.; He, J. *Dalton Trans*, **2010**, 39, (38), 9063-9072.

# Chapter 3

## *Effect of halogen ions on the growth and properties of CIS QDs*

*Due to the technological relevance of CIS QDs for a number of applications, a precise control over their optical properties is of paramount importance. The most common approach for the synthesis of high quality CIS QDs is the thermal decomposition. This synthetic method exploits the coordinating capabilities of specific molecules to obtain sulfur-containing metal-organic precursors. These are dissolved in high boiling point organic solvents and heated to temperatures above 200 °C. This leads to their decomposition into species that are the building blocks for the growth of QDs. Although the vast literature about the effect that the reaction parameters have on the growth and final properties of CIS QDs, little has been said about the effect that the type of metal precursor has on the reaction kinetics and optical features of the final product. Here we present a study on the consequence of using different copper sources. Three copper halogenide salts were selected as* $Cu^+$ *source (namely iodine, bromide, and chloride) for the synthesis of CIS QDs via the thermal decomposition approach. The investigation of the QD optical properties, monitored during their growth, combined with the information obtained from the structural and chemical characterization, suggests an effect played by the halogen ions in solution. Observing the trend of the properties displayed by the QDs, it was postulated that the parameter playing a major role is the polarizability of the ions following the behavior predicted by the so-called Hofmeister series.*

## 3.1 Materials and metods

### 3.1.1 Chemicals

Copper iodide (CuI, 99.999%, Aldrich), copper bromide (CuBr, 99.999%, Aldrich), copper chloride (CuCl, 99.999%, Aldrich), indium acetate ($In(OAc)_3$, 99.99%, Aldrich), 1-octadecene (ODE, 90%, Alpha Aesar), oleic acid (OA, 90%, Alpha Aesar), 1-dodecanethiol (DDT, 98%, Aldrich), chloroform (99.8%, Alpha Aesar), hexane (99%, Alpha Aesar), ethanol (100%, Commercial Alcohols), and methanol (99.9%, Fisher Scientific) were all used as received without further purification.

### 3.1.2 Synthesis of CIS QDs

CIS QDs have been synthesized according to a simple thermal decomposition method. The samples were named after the copper source used for the synthesis: CIS-Cl, CIS-Br, and CIS-I when CuCl, CuBr, and CuI were used respectively. Briefly 0.2 mmol of copper halogenide, 0.2 mmol of $In(OAc)_3$, 10 mL of ODE, 3.9 mL (16 mmol) of DDT, and 0.708 mL (2 mmol) of OA were introduced in a 50 mL three-necked round bottom flask. The solution was stirred at 100 °C under vacuum for 1 hour and backfilled with Ar. Then the temperature was raised to 120 °C and maintained at this stage for 5 min. The temperature was further raised to 150 °C and maintained for 5 min. Eventually, the temperature was set to 230 °C. Upon heating, the solution becomes completely clear and slightly yellow. Then the color changes from deep yellow to orange, then red, and eventually dark brown indicating the nucleation and subsequent growth of the QDs. Aliquots were sampled at different time intervals after reaching 230 °C (5 min, 10 min, 20 min, 30 min, 45 min, 60 min, 90 min) and after 120 min the flask was quenched in cold water. Each aliquot (approximately 400 μL) was quenched in 100 μL of cold hexane and precipitated by the addition of 1 mL of ethanol. The QDs were centrifuged (20 min at 6000*g*) and the supernatant discarded. The QDs were further dispersed in 200 μL of hexane and washed twice with ethanol, before being re-dispersed in hexane for the optical characterization.

For XPS, XRPD, and TEM analyses the QDs were further washed thoroughly using a mixture of chloroform:methanol (1:1) to precipitate the QDs out from hexane. This process was repeated at least three times to ensure the removal of unreacted precursors.

### 3.1.3 Characterization techniques

**Optical Properties.** Absorption spectra were acquired on a Varian Cary 5000 Spectrophotometer. The sols were diluted in hexane to an optical density below 1 throughout the whole measurement range. QD PL emission spectra were recorded on a Varian Cary Eclipse Fluorescence Spectrophotometer equipped with a Xenon flash lamp. For the PL emission studies, the optical density of the samples was kept below 0.1 at the excitation wavelength (455 nm). To compare the emission intensity of the samples reacted for 30 min we adjusted the optical density of the sols to 0.1 at the excitation wavelength.

**Structure, morphology, and composition.** The crystalline structure of the samples was probed by means of XRPD with a Bruker D8 Advance Diffractometer using a CuKα radiation. The diffractograms were fitted using the Rietveld refinement procedure with the software GSAS®[1, 2] in order to obtain information about the lattice parameters. The composition of the samples was investigated by means of XPS, recording the spectra with a VG ESCALAB 200i XL using an Al Kα monochromatic source. The spectra were analyzed using CasaXPS® software. For both XRPD and XPS measurements the samples were prepared depositing few drops of the hexane solutions of purified QDs on a glass slide and letting the solvent slowly evaporate in air. The morphology was analyzed by means of TEM and HREM using a JEOL JEM 3010 microscope (1.7 Å point to point resolution at Scherzer defocus). Before TEM measurements, each sample was further diluted in hexane to an approximate concentration of 0.1 mg/mL and sonicated for 2 min. One drop of the solution was deposited on a holey carbon-coated nickel grid and the solvent was allowed to slowly evaporate in air.

## 3.2 Results and discussion

The CIS QDs prepared using different $Cu^+$ salts show different behaviors depending on the nature of the chosen precursor. We selected halogenide precursor salts, namely chloride, bromide, and iodide, being among the most exploited copper precursors in the synthesis of CIS-based QDs.

### 3.2.1 Optical properties

The absorption spectra of the samples show a shift of the absorption edge towards longer wavelengths with increasing reaction time (Figure 3.1a, b, c). This behavior is in accordance with what is predicted by the quantum confinement effect.

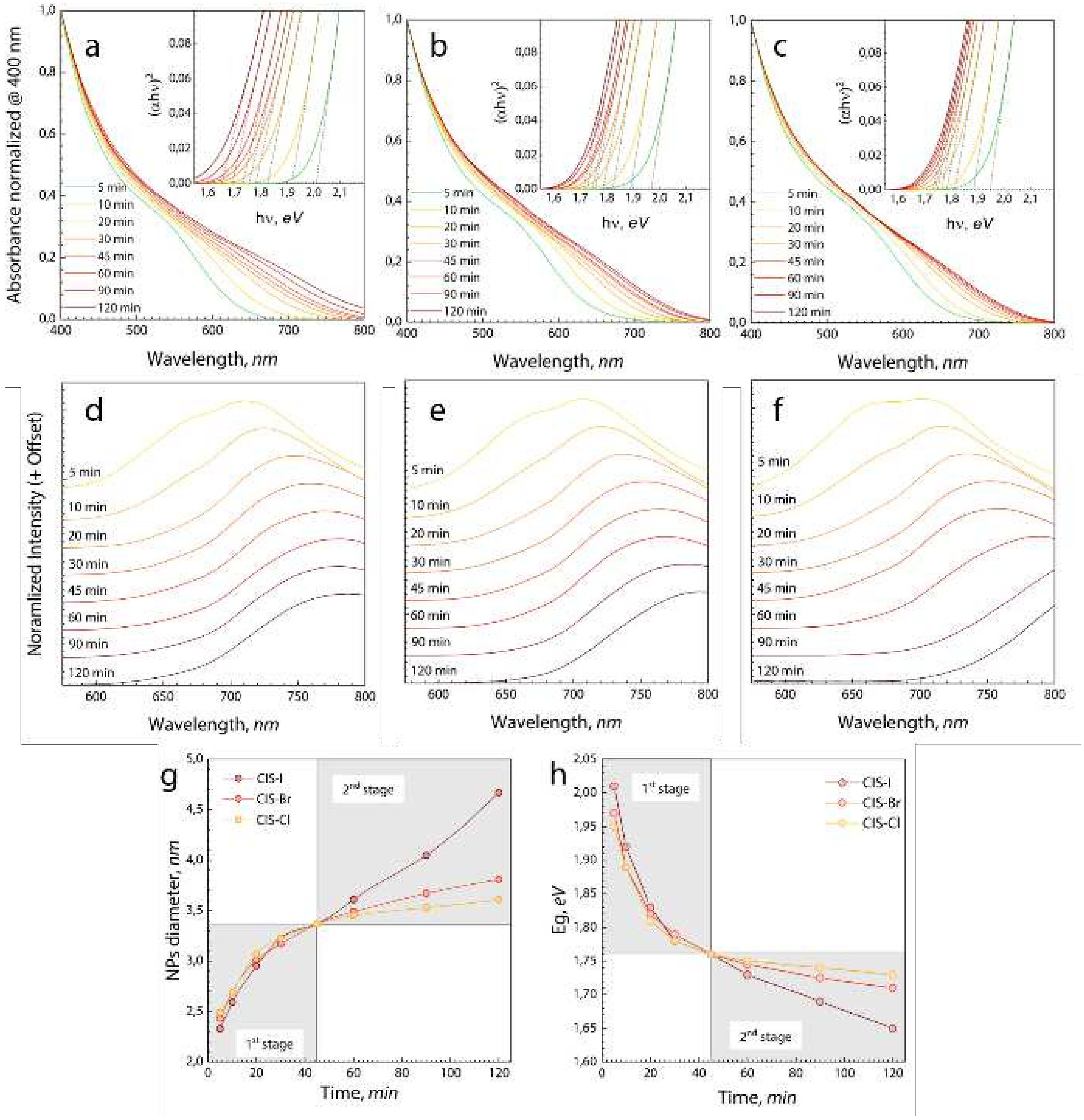

**Figure 3.1**. Results of the optical characterization of the samples CIS-Cl, CIS-Br, and CIS-I. From the absorption spectra reported in *a, b,* and *c* we obtained the correspondent Tauc plots (see respective insets). The fit of the linear part of these plots allow to obtain information about the actual band gap of the QDs (*h*), thus indirectly about their size (*g*). Two stages of the reaction can be individuated from this elaboration: in the first stage, the QD size follows the same trend for all the samples; in the second stage, the QD size varies significantly from batch to batch, following the trend I>Br>Cl. The same trend is observed also in the QD emission (*d*, *e*, and *f*). The emission profiles have been normalized to their maximum for the sake of clarity.

The absorption spectra have been analyzed according to the Tauc interpretation[3] in order to obtain information about the dimension of the nanosized semiconductors. Since $CuInS_2$ is a direct band gap material, $(\alpha h\upsilon)^2$ was plotted versus the photon energy $h\upsilon$ and the linear part of the plot was extrapolated: the point at which the linear fit intersects the *x*-axis returns the band gap value. We observed a decrease of the band gap energy ($E_g$) with increasing reaction time (Figure 3.1h). We related the $E_g$ to the size of the particles using the effective mass approximation[4], according to the equation:

$$E_g = E_{g,bulk} + \frac{h^2}{8R^2}\left(\frac{1}{m_e^*} + \frac{1}{m_h^*}\right) - \frac{1.786e^2}{4\pi\varepsilon_0\varepsilon_r R^2} \tag{3.1}$$

Where *h* is the Planck's constant, *R* is the QDs radius, $m^*_e$ and $m^*_h$ are the reduced electron and hole mass respectively, *e* is the electron charge, and $\varepsilon_0$ and $\varepsilon_r$ are the dielectric permittivity in vacuum and in the material respectively. From the absorption analysis we can already observe a difference in the behavior of the QDs synthesized in the presence of different anions. In particular it is known that, according to the Hofmeister interpretation, the three halogen ions possess different interacting properties with hydrophobic molecules[5]. The charge distribution of the electronic cloud is rather diffuse in heavier halogen ions, so the polarizability decreases according to the series I>Br>Cl, going from the more *chaotropic* ion to the more *kosmothropic* one[6]. This classification is based on the respective soft or hard character of the ions, considering their capability of stabilizing the biological molecules and their interaction with the water molecules. The water molecules can be rigidly organized around the ion in an ordered fashion (*kosmos*) or they can be less tightly bound to the ion surface forming a diffuse and dynamic layer (*chaos*). This behavior descends directly from the polarizability of the ion. For the very same reason, the chloride anion (the smaller halogen under study), having a high surface charge, interacts weakly with hydrophobic surfaces[6]. In this view, we give an interpretation of the different behavior observed in the presence of the different anions in the reaction environment. In particular, we can divide the growth regime into two stages (Figure 3.1g). In the early stage the growth kinetics are very similar in the presence of the different anions. A small difference is still appreciable, with CIS-I being composed of smaller QDs if compared to CIS-Br and CIS-Cl respectively. In the second stage, after 40 min of reaction, the growth rate in the presence of iodide anions becomes significantly faster than the one observed in the presence of the less polarizable halogen anions, *i.e.* bromide and chloride. Indeed, in the presence of iodide anions the QD absorption can be extended above 800 nm. Instead, when copper salts with smaller counterions are used, the growth appears to be hindered preventing the QD absorption onset to effectively be shifted towards the NIR region.

The same trend is confirmed by the photoluminescence analyses (Figure 3.1d, e, f). The emission peak shifts upon increasing the reaction time: although not being excitonic in nature, the emission in this kind of QDs is known to be size-related[7, 8]. Due to the involvement of the CB in the electronic transitions, as the diameter of the quantum dots increases, *i.e.* the band gap widens, the emission experiences a bathochromic (*i.e.* towards shorter wavelengths) shift accordingly. We also noted that the emission intensity is dependent upon the copper source used in the synthesis (Figure 3.2). Comparing the PL profiles of the samples reacted for 30 min it is possible to observe that CIS-I displays a higher photoluminescence efficiency with respect to that of CIS-Br and CIS-Cl. In particular, the PLQY follows the order I>Br>Cl, reacching a maximum of 4.5 % in CIS-I. The reason for this behavior will be discussed in the following of the text at the light of the structural analyses.

### 3.2.2 Structural and morphological characterization

The XRPD analysis allows to assign the crystalline phase of the samples be tetragonal chalcopyrite (PDF #00-047-1372) (Figure 3.3).

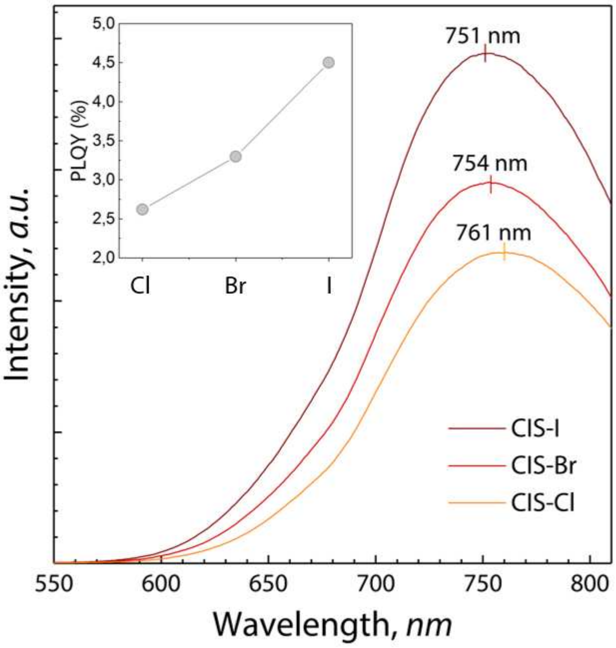

**Figure 3.2**. Comparison of the PL emission of the three samples synthesized in this study after 30 min of growth, when the optical properties, when the emission of the QDs reaches its maximum efficiency. In the inset the PLQY values of the three samples are compared (CIS-Cl – 2.6 %, CIS-Br – 3.3 %, CIS-I – 4.5 %).

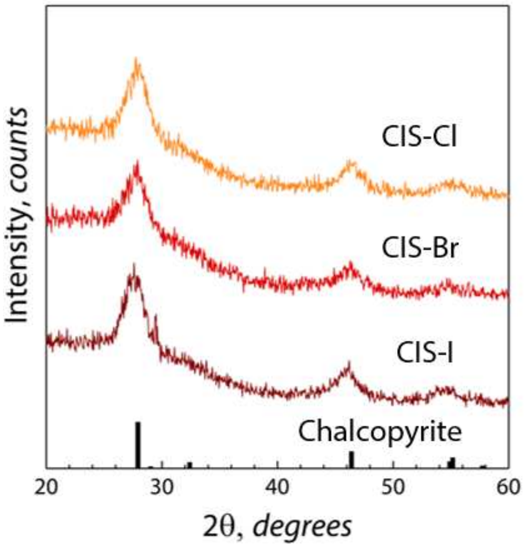

**Figure 3.3.** The diffractograms of the samples reacted for 120 min all show the presence of pure phase chalcopyrite polymorph. The peaks experiences a weak shift towards smaller angles following the order Cl-Br-I.

Although this approach has been demonstrated to lead to the formation of tetragonal phase QDs[7], it is to be mentioned that a zinc blende structure cannot be ruled put only in the basis of X-ray diffraction measurements when considering small NPs[9]. Actually, the difference among these two structures is so small that it is usually hard to discern between them in QDs, owing to their XRPD broad reflections. The (112) reflection between 25° and 30° is used to obtain qualitative information about the crystallite size in the samples using the Scherrer equation[10].[1] Upon fitting the peak using a Lorentz function (since the use of a pseudo-Voigt profile returns a negligible Gaussian contribution) and assuming QDs as single crystalline domains, we obtain a mean size of 3.3 nm, 3.6 nm, and 3.9 nm for CIS-Cl, CIS-Br, and CIS-I respectively. This trend is in accordance with the results found using the effective mass approximation. The Rietveld refinements performed on the XRPD patterns returns a cell volume for the different samples which follows the trend I>Br>Cl. This is consistent with the interpretation of the halogen ions incorporation in the QDs lattice, iodide (216 pm) being larger than bromide (195 pm) and chloride (181 pm).

---

[1] Extensive discussions in the past years have highlighted that the results coming from this approach are by no means an absolute indication of the size of the crystallites. This is mainly due to the heavy restrictions imposed *a priori*, *i.e.* a perfectly monodisperse sample composed of cubic crystallites. The values obtained from the Scherrer equation can only be used to compare in a relative way the size of different samples

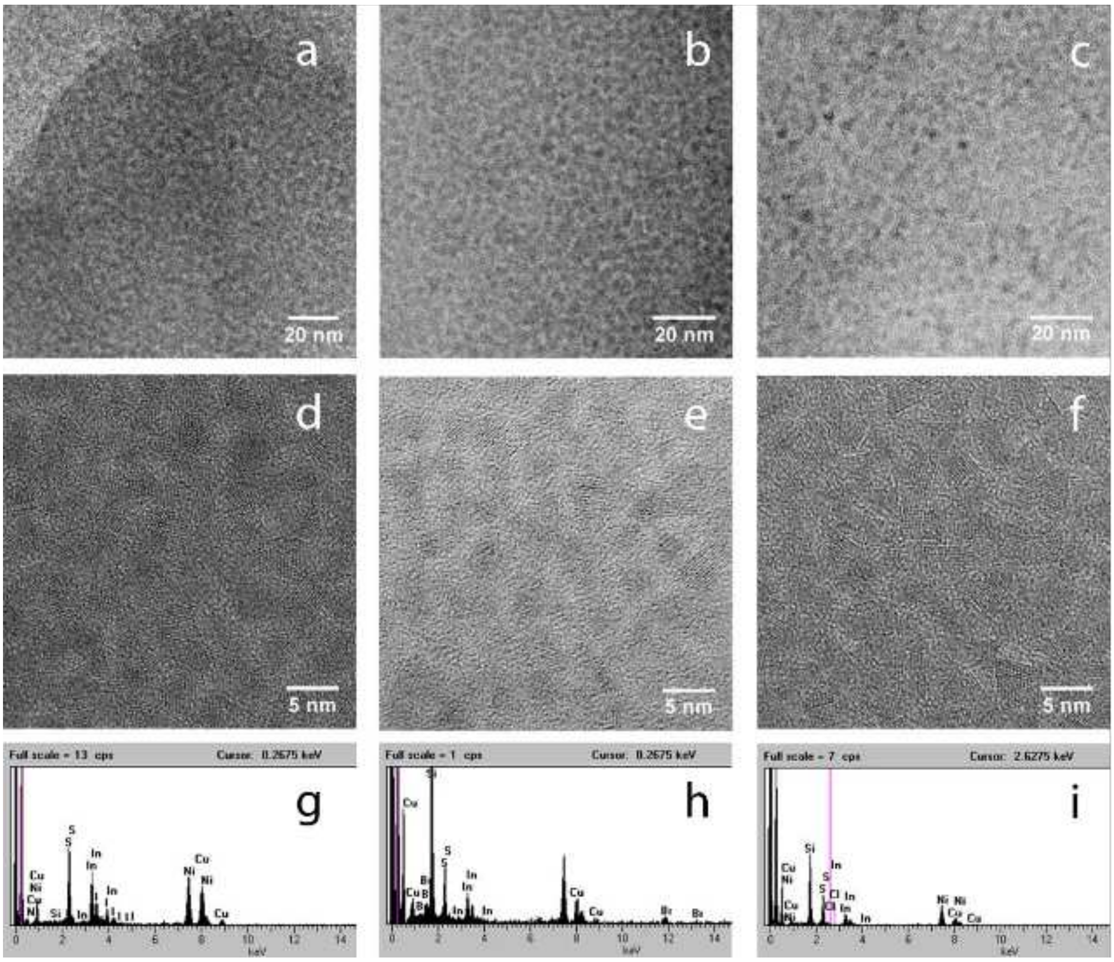

**Figure 3.4.** The TEM micrographs of CIS-Cl (*b* and *e*), CIS-Br (*c* and *f*), and CIS-I (*d* and *g*) show QDs with a polygonal shape. The corresponding EDX spectra (*h*, *i*, and *j*) highlight the presence of Cu, In, and S. I and Br are also observed in the spectra, while the signal coming from Cl is too weak to be observed.

Moreover, iodide is more effectively retained in the samples than bromide and chloride (see XPS results below and EDX measurements), thus further corroborating the interpretation suggested by the cell volume difference between the three samples. To support this interpretation we analyzed the samples by means of TEM and XPS. From TEM observations (Figure 3.4 a-f), the nanoparticles appear to have a good crystallinity after 120 min of reaction. The morphology is polygonal, with a crystalline habitus typical of a tetragonal structure, supporting the attribution of the phase to the chalcopyrite polymorph[7, 11]. It is hard to determine the actual size of the QDs in each sample due to the rather irregular shape, so no comparison between the three batches can be made given that the expected size difference is of the order of magnitude of 1 nm or less. The EDX analyses (Figure 3.4 g-i) return the expected elements in the samples, with Cu, In, and S being the most abundant ones. Beside them, iodine and bromine lines can be observed in the spectra of the samples CIS-I and CIS-Br, while no chlorine is detectable in the sample CIS-Cl. These results are in accordance with the XPS observations reported below. The typical lines of Si and Ni, arise respectively from contaminations in the TEM column and from the grid.

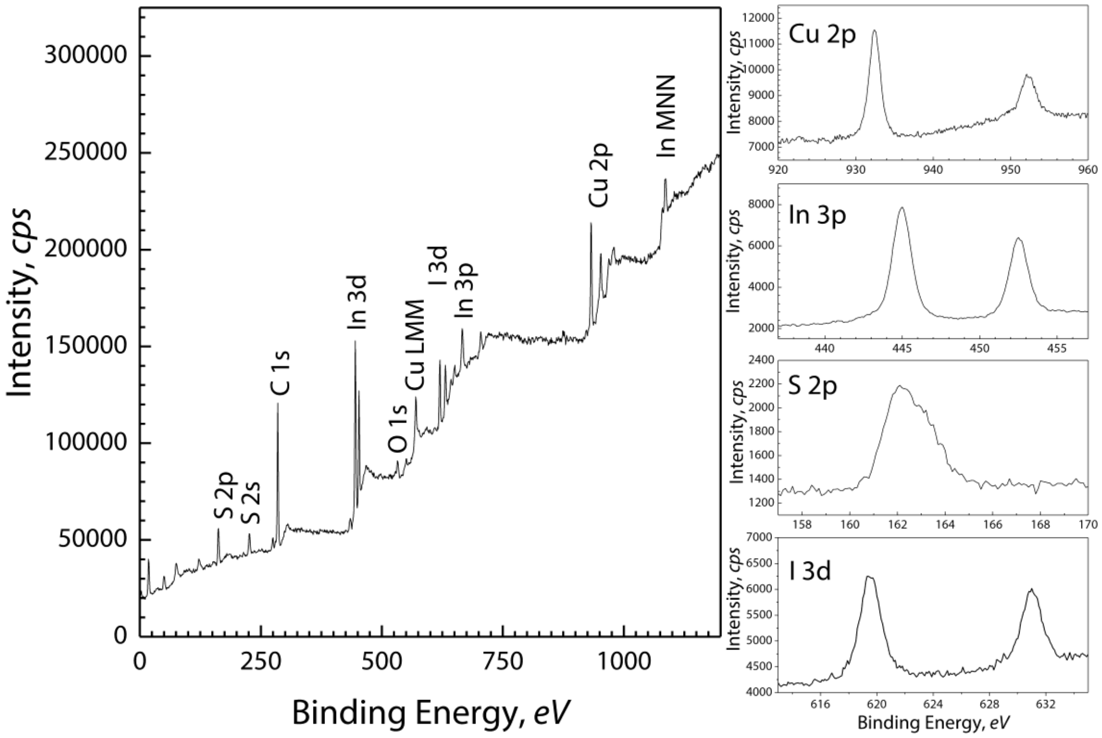

**Figure 3.5.** XPS survey and high-resolution spectra of the sample CIS-I. The signal of the halogen ion is visible along with those of the main components of CIS QDs.

**Table 3.1.** Attribution of the XPS signals for the samples CIS-I.

| | **Calibrated BE, *eV*** | **Peak assignment** |
|---|---|---|
| C 1s | 284.4 | Graphitic/adventitious carbon |
| O 1s | 531.35 | C=O |
| I 3d | 619.9 | Metal iodide |
| Cu 2p | 932.0 | Cu(I)-S (also Cu-I) |
| In 3d | 444.5 | $In_2O_3$, $CuInS_2$ or $In_2S_3$. |
| S 2p | 161.55 | Metal sulfide |

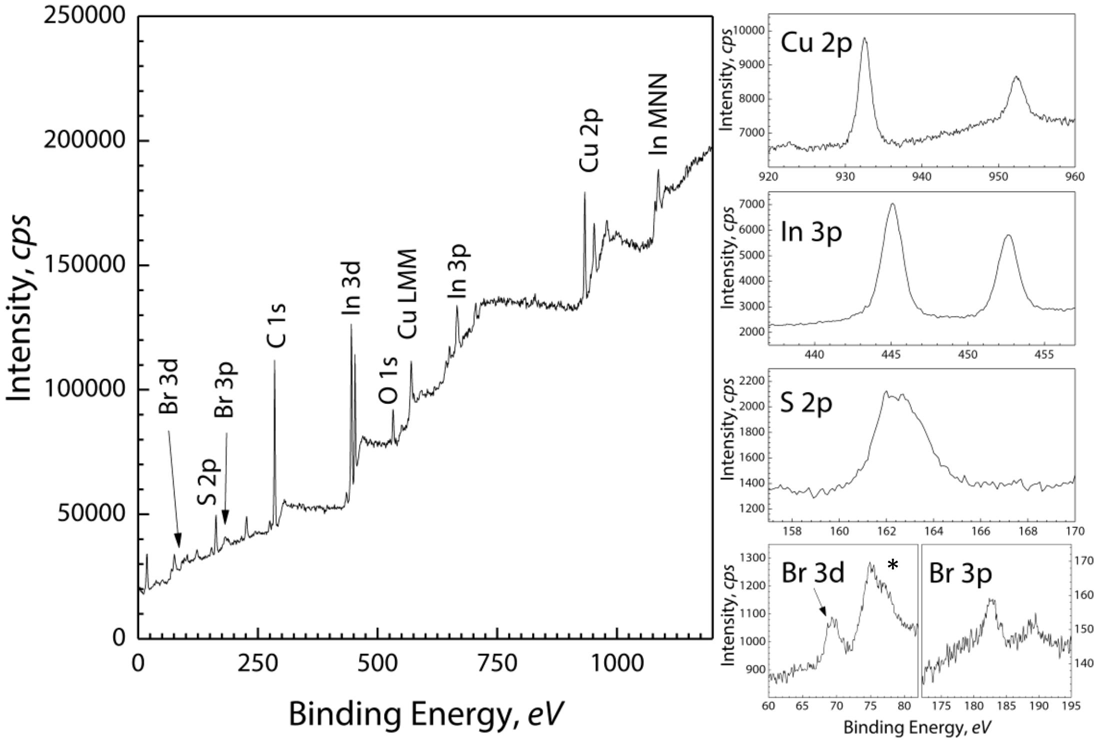

**Figure 3.6.** XPS survey and high-resolution spectra of the sample CIS-I. The signal of the halogen ion is visible along with those of the main components of CIS QDs.

**Table 3.2.** Attribution of the XPS signals for the samples CIS-Br.

| | **Calibrated BE, *eV*** | **Peak assignment** |
|---|---|---|
| C 1s | 284.4 | Graphitic/adventitious carbon |
| O 1s | 531.8 | C=O |
| Br 3d | 68.45 | Metal bromide |
| | *74.25** | *Cu 3p peak ** |
| Br 3p | 182.05 | Metal bromide |
| Cu 2p | 932.05 | Cu(I)-S (also Cu-Br) |
| In 3d | 444.55 | $In_2O_3$, $CuInS_2$ or $In_2S_3$. |
| S 2p | 161.7 | Metal sulfide |

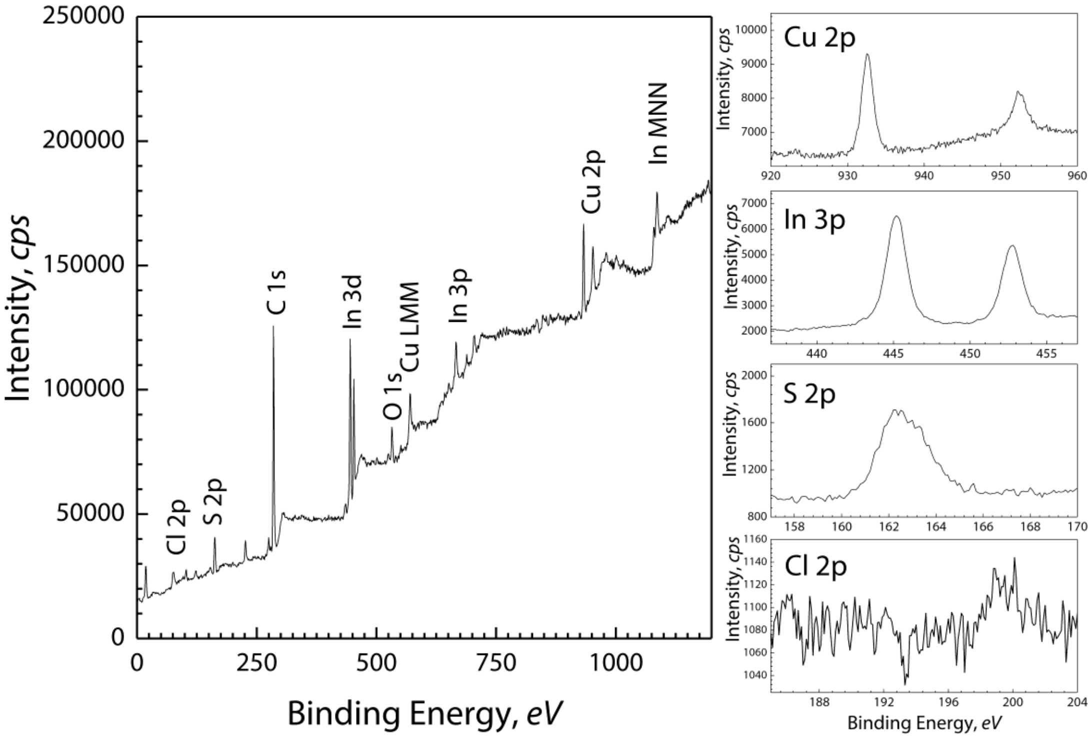

**Figure 3.7.** XPS survey and high-resolution spectra of the sample CIS-Cl. The signal of the halogen ion is very weak but still visible along with those of the main components of CIS QDs.

**Table 3.3.** Attribution of the XPS signals for the samples CIS-Cl.

| | **Calibrated BE, *eV*** | **Peak assignment** |
|---|---|---|
| C 1s | 284.4 | Graphitic/adventitious carbon |
| O 1s | 531.8 | C=O |
| Cl 2p | 198.4 | Metal chloride |
| Cu 2p | 932.0 | Cu(I)-S (also Cu-Cl) |
| In 3d | 444.55 | $In_2O_3$, $CuInS_2$ or $In_2S_3$ |
| S 2p | 161.6 | Metal sulfide |

The XPS measurements give more insights about the QD composition. In all the spectra the characteristic peaks of each halogen ion are present along with the expected signals of Cu, In, and S (Figure 3.5, 3.6, 3.7 and Table 3.1, 3.2, 3.3). Copper and indium signals arise from single populations of $Cu^+$ and $In^{3+}$ ions respectively. In Cu 2p region no satellite peaks are present (which usually appear around 942 eV), indicating the absence of $Cu^{2+}$. Since no metal oxide peak is observed in O 1s, the presence of $Cu_2O$ and $In_2O_3$ is excluded. It is not possible to distinguish between metal sulfide and metal halogenide (if any) signal, due to the small energy difference expected for these two species. However, the signal of iodide, bromide, and chloride is found in correspondence of the typical binding energy of the respective metal halogenides. For each sample the composition normalized to the $In^{3+}$ content was evaluated together with the halogen ion atomic percentage (Table 3.4). It is to be reminded that these samples were thoroughly washed with mixtures of ethanol:hexanes and extracted with methanol:chloroform at least three more times, so that we can exclude the presence of unreacted salts in the purified samples. The atomic percentage of halogen ions in the QDs follows the order I>Br>Cl. This trend is in accordance with the EDX analyses performed during the TEM observations. This difference in halogen ion content makes it even more unlikely that the recorded signals arise from unreacted precursors. Actually all the $Cu^+$ salts are equally sparingly soluble in the used solvents. Due to this fact, if the chloride ions in excess are removed efficiently, also bromide and iodide salts are expected to be washed away during the purification steps. Further evidence supporting the interpretation of the halogen ion incorporation is the presence of a lesser amount of sulfur in the CIS-I and CIS-Br samples. Actually, the presence of halogen ions in the lattice is expected to the presence of sulfur vacancies in order to maintain the charge neutrality of the structure.

**Table 3.4.** Summary of the results obtained from the Rietveld refinements of the diffractograms and the analyses of the XPS spectra of the three samples reacted for 120 min. The samples have been thoroughly washed before analyses in order to avoid the presence of unreacted salts. The percentage of halogen ions (X) is given with respect to the total amount of Cu, In, and S. The cell volume, as obtained from the Rietveld refinements, increases accordingly to the increase of the halogen content which has been estimated from the XPS spectra.

| Sample | a, *Å* | c, *Å* | Volume, *Å³* | Cu : In : S | X %$_{atomic}$ |
|---|---|---|---|---|---|
| CIS-I | 5.6(2) | 11.0(0) | 347.(4) | 1.20 : 1.00 : 1.68 | 6.4 |
| CIS-Br | 5.5(1) | 11.2(7) | 342.(2) | 1.17 : 1.00 : 1.77 | 5.7 |
| CIS-Cl | 5.4(9) | 11.2(5) | 339.(1) | 1.32 : 1.00 : 2.31 | 1.1 |

### 3.2.3 Interpretation of the anion effect

At the light of the results reported above, we postulate a mechanism through which the anions could affect the QD features. In order to avoid natural fluctuations occurring in the properties of the synthesized samples to affect the conclusions drawn in this study, we synthesized the series from different $Cu^+$ salts twice, obtaining in both cases the trend described in the sections above.

We observed that the trend of anions incorporation efficiency (I>Br>Cl) follows that of the anions polarizability, suggesting an interpretation based on the different interaction of the three halogen ions with the hydrophobic molecules in solution. Actually, the thermal decomposition method utilized in this work relies on the creation of metal-thiolate precursors (Cu-DDT and In-DDT) which are decomposed at high temperature. The halogen ions interact to different extents with the hydrophobic alkyl chains of the thiolates, depending on their polarizability. Since iodine is the larger ion (*i.e.* more polarizable), it interacts more strongly with these chains, thus having more chances to be incorporated in the crystalline lattice during the formation of the QDs. Moreover, this stronger interaction among DDT and iodine ions is expected to play a role in controlling the QD growth: due to electrostatic interaction, the anions can slow down the nucleation and growth stages. This should lead to less defective QDs that have lesser defect levels responsible for the quenching of the PL emission.

With this being said, it is not possible to completely exclude that part of the anions could be attached on the surface of the QDs even after the extensive washing steps to which the samples have been subjected. Moreover, the actual presence of anions in the lattice might have a direct effect too on the optical properties of the QDs. These anions could perturb the chemical surrounding of the metal ions in such a way that the PL emission is enhanced.

It is clear that the identification of the process through which the anions influence the synthesis and the properties of the nanoparticles remains challenging. This is mainly due to the lack of literature about the subject: not even the actual effect of the anions interacting with molecules in aqueous solutions, a subject far more studied than the organic case, has received a conclusive explanation (the review from Salis and Ninham[12] gives a deep insight about the subject). Nonetheless, it is undoubted that the use of different precursors leads to QDs with different properties, and that the trend follows that of the polarizability (*Hofmeister series*) of the copper counterions.

### 3.2.4 Ongoing analyses

In order to confirm the incorporation of the halogen ions in the QD lattice, Extended X-ray Absorption Fine Structure (EXAFS) studies have been performed and are currently planned at the National Synchrotron Radiation Research Center in Taiwan. First measurements performed on the samples grown for 2 h show trends that might be a decisive evidence of the presence of Cl, Be, and I in the crystal structure (Figure 3.8). In particular, copper *K*-edge experience a gradual shift towards lower energy following the order CIS-Cl, CIS-Br, CIS-I (Figure 3.8a). Moreover, copper coordination number seems to slightly decrease in the order just mentioned (Figure 3.8b, feature marked with an asterisk). Eventually, sulfur EXAFS *K*-edge signal shows two features whose trend is the opposite along the series, suggesting the change of sulfur valence (Figure 3.8c). Also sulfur coordination number changes (feature marked with an asterisk in Figure 3.8d). Altogether this information might provide a further insight about the arrangement of the ions in the crystalline lattice. However, measurements performed in correspondence of the absorption edge of the halogen ions are needed to confirm speculations about different arrangements in the lattice of the QDs depending on the copper counterion that has been used for the synthesis.

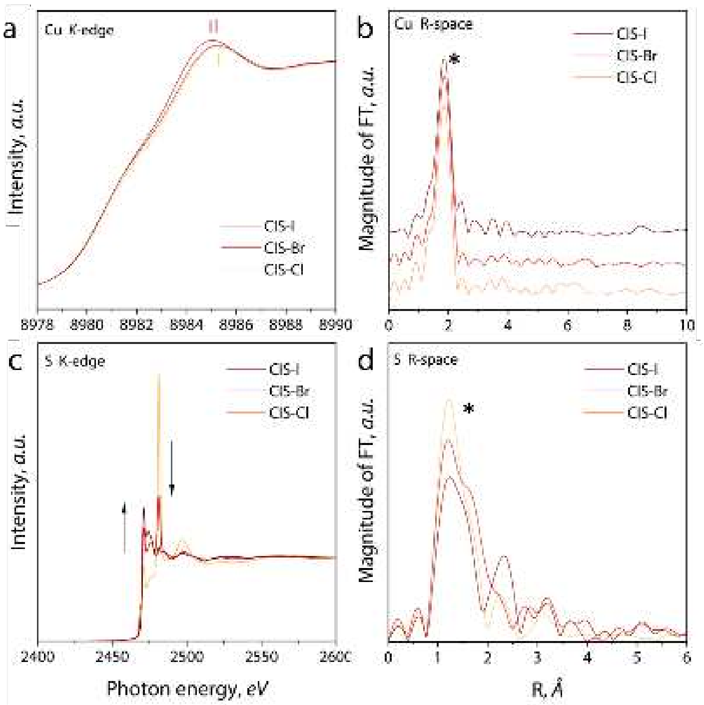

**Figure 3.8.** Copper (*a* and *b*) and sulfur (*c* and *d*) EXAFS measurements performed in correspondence of these element *K*-edge. Although some changes in the position and intensity of the features can be observed in both cases, a definitive interpretation will be possible only after the analysis of the spectra of the halogen ions.

## 3.3 Conclusions

CIS QDs have been synthesized according to a well-established thermal decomposition approach in organic solvents. Three batches of QDs have been produced starting from different halogenide $Cu^+$ sources namely iodide, bromide, and chloride. Experimental evidences show that the presence of halogen anions in the growth solution affects the QD properties. The effect on the QDs structural and optical features follows the same trend as of the halogen ion polarizability (I>Br>Cl). In particular, it was observed that CuI is the best copper precursor, among the halogenide salts, in terms of QD quality and optical properties tunability: the higher the anion polarizability, the more the QD size can be controlled and their PL emission is efficient. The comparison of the optical results with the results of XRPD, EDX, and XPS measurements allows postulating a major role played by the interaction of the halogen anions with the metal-thiolates alkyl chains. According to the Hofmeister interpretation, the larger the anion (*i.e.* the more it is polarizable) the stronger the interaction with hydrophobic moieties. Indeed we found that the possibility of controlling the QD features and the incorporation of the anions in the $CuInS_2$ tetragonal lattice follow the I>Br>Cl trend, matching that of the anions polarizability. EXAFS studies are currently being performed in order to corroborate the interpretation of anion inclusion in the lattice of QDs. The observation that the anions in the growth solution play an important role in determining the final properties of QDs constitutes a fundamental disclosure for the synthesis of high quality CIS QDs. Indeed, a better rationalization of the effect of synthetic parameters in the preparation of copper-based chalcogenide QDs would pave the way for a more accurate choice of the starting materials, with the possibility of finely tuning the properties of the final product,

## References

1. Larson, A. C.; Von Dreele, R. B. *General Structure Analysis System (GSAS), Los Alamos National Laboratory Report LAUR*, Los Alamos National Laboratory, 2000.
2. Toby, B. H. *J Appl Crystallogr*, **2001**, 34, (2), 210-213.
3. Wherrett, B. S. *Optica Acta: International Journal of Optics*, **1973**, 20, (3), 250-250.
4. Zhong, H.; Zhou, Y.; Ye, M.; He, Y.; Ye, J.; He, C.; Yang, C.; Li, Y. *Chem Mater*, **2008**, 20, (20), 6434-6443.
5. Lo Nostro, P.; Ninham, B. W. *Chem Rev*, **2012**, 112, (4), 2286-2322.

6. Pfeiffer, C.; Rehbock, C.; Huhn, D.; Carrillo-Carrion, C.; de Aberasturi, D. J.; Merk, V.; Barcikowski, S.; Parak, W. J. *J R Soc Interface*, **2014**, 11, (96), 20130931.
7. Booth, M.; Brown, A. P.; Evans, S. D.; Critchley, K. *Chem Mater*, **2012**, 24, (11), 2064-2070.
8. Cichy, B.; Bednarkiewicz, A.; Strek, W. *J Opt*, **2013**, 15, (41), 085303.
9. Huang, W. C.; Tseng, C. H.; Chang, S. H.; Tuan, H. Y.; Chiang, C. C.; Lyu, L. M.; Huang, M. H. *Langmuir*, **2012**, 28, (22), 8496-8501.
10. Scardi, P.; Leoni, M.; Delhez, R. *J Appl Crystallogr*, **2004**, 37, (3), 381-390.
11. Michalska, M.; Aboulaich, A.; Medjahdi, G.; Mahiou, R.; Jurga, S.; Schneider, R. *J Alloys Compd*, **2015**, 645, 184-192.
12. Salis, A.; Ninham, B. W. *Chem Soc Rev*, **2014**, 43, (21), 7358-7377.

# Chapter 4

## *Study of the energy transfer between upconverting nanoparticles and CIS QDs*

*Förster resonance energy transfer (FRET)[1] is a physical phenomenon that has a great importance from an applicative point of view. It involves the non-radiative transfer of absorbed energy from a donor to an acceptor moiety in close proximity, with the consequent quenching of the donor emission. Many bio-assays have been developed that imply the use of FRET optical probes, due to the relative simplicity of the detection process. Most of these systems rely on the use of organic dyes as acceptors and, while QDs have been extensively used as donors, only recently their use as FRET acceptors has been proposed. Here we investigate the ET mechanism that takes place between upconverting nanoparticles (UCNPs) and QDs upon irradiation with NIR light (980 nm). $LiYF_4$:Yb,Tm and CIS QDs were respectively chosen as donors and acceptors because of the good spectral overlap that this combination provides. The nature of the ET was observed to be radiative in the case of sols where the UCNPs and QDs were dispersed together, meaning that the random motion of the particles in the medium is not sufficient to bring them in close proximity. Instead, when donors and acceptors were deposited and let dry on a glass slide, evidences of FRET were clearly observed. In particular, a strong QD PL signal was detected along with a decrease of the upconversion luminescence (UCL) LT upon NIR excitation of the donors. Although further tests are currently being conducted on the proposed systems, these preliminary results are valuable information that can be used to improve the design of robust all-inorganic optical probes for FRET-based assays.*

## 4.1 Materials and metods

### 4.1.1 Chemicals

Copper iodide (CuI, 99.999%, Aldrich), indium acetate ($In(OAc)_3$, 99.99%, Alfa Aeasar), 1-octadecene (ODE, 90%, Alfa Aesar), oleic acid (OA, 90%, Alfa Aesar), 1-dodecanethiol (DDT, 98%, Aldrich), yttrium oxide ($Y_2O_3$, 99.999%, Alfa Aesar), ytterbium oxide ($Yb_2O_3$ ,99.999%, Alfa Aesar), thulium oxide ($Tm_2O_3$ ,99.999%, Alfa Aesar), lithium trifluoroacetate (98%, Alfa Aesar), trifluoroacetic acid (TFA, 95%, Alfa Aesar), hexane (99%, Alfa Aesar), toluene (Aldrich), ethanol (100%, Commercial Alcohols), and methanol (99.9%, Fisher Scientific) were all used as received without further purification.

### 4.1.2 Synthesis of nanoparticles

**CIS QDs**. CIS QDs have been synthesized according to a simple thermal decomposition method. Briefly, 9.5 mg of CuI (0.05 mmol), 58.4 mg of $In(OAc)_3$ (0.2 mmol), 10 mL of ODE, 3.9 mL (16 mmol) of DDT, and 0.708 mL (2 mmol) of OA were introduced in a 50 mL three-necked round bottom flask. The solution was stirred at 100 °C under vacuum for 45 min and backfilled with Ar. Then, the temperature was raised to 120 °C and maintained at this stage for 5 min. The temperature was further raised to 150 °C and maintained for 5 min more. Eventually, the temperature was set to 230 °C. Upon heating, the solution became completely clear and slightly yellow. Then the color changed from deep yellow to orange, then red, and eventually dark red indicating the nucleation and subsequent growth of the QDs. After 45 min the flask was quenched in cold water. The QDs were transferred to a centrifuge tube and precipitated by the addition of acetone. They were centrifuged (20 min at 6000*g*) and the supernatant was discarded. The QDs were dispersed in toluene and washed twice with acetone, before being re-dispersed in toluene for further characterization. The final concentration of the stock sol was 11.0 mg/mL approximately corresponding to a concentration range between 0.11-0.26 mM.

**$LiYF_4$:Yb(25%),Tm(0.5%) (LYFYT).** The UCNPs were synthesized according to a well-established thermal decomposition method starting from trifluoroacetates of the corresponding RE ions[2]. The trifluoroacetates were prepared by mixing 219.3 mg of $Y_2O_3$ (0.931 mmol), 123.2 mg of $Yb_2O_3$ (0.3125 mmol), and 2.4 mg of $Tm_2O_3$ (0.00625mmol) with 5 mL of TFA and 5 mL of water in a 100 mL three-necked round bottom flask. After complete dissolution of the oxides under stirring at 80 °C, water was evaporated overnight at 60 °C. Then, to the dried RE trifluoroacetates 310 mg of lithium trifluoroacetate (2.5 mmol) were added along with 20 mL of OA and 20 mL of ODE. The mixture was degassed at 110 °C for 30 min and backfilled with Ar. The temperature was then raised to 330 °C and the reaction was allowed to proceed for 1 h. After this time, the heating was stopped and the flask was allowed to naturally cool down to 60 °C. The reaction product was split in two centrifuge tubes and the UCNPs were precipitated by the addition of ethanol. They were centrifuged (20 min at 6000*g*) and the supernatant was discarded. The UCNPs were then dispersed in hexane and washed three times with ethanol before being re-dispersed in toluene for further characterization. The final concentration of the stock sol was 52.0 mg/mL corresponding to a molar concentration of approximately 0.027 μM.

**$LiYF_4$:Yb(25%)/$LiYF_4$:Yb(25%),Tm(0.5%) (LYFY/LYFYT).** For the synthesis of core/shell UCNPs RE trifluoroacetates were synthesized following the same procedure described above and mixing respectively:

- *LYFY (core)* - 220.8 mg of $Y_2O_3$ (0.9375 mmol) and 123.2 mg of $Yb_2O_3$ (0.3125 mmol) with 5 mL of TFA and 5 mL of water in a 100 mL three-necked round bottom flask.
- *LYFYT (shell)* - 219.3 mg of $Y_2O_3$ (0.931 mmol), 123.2 mg of $Yb_2O_3$ (0.3125 mmol), and 2.4 mg of $Tm_2O_3$ (0.00625mmol) with 5 mL of TFA and 5 mL of water in a 50 mL three-necked round bottom flask.

The precursors were allowed to dissolve and dry overnight. Core UCNPs were synthesized following the approach described for core-only LYFYT UCNPs. After 30 min of reaction, to the dried shell precursors 310 mg of lithium trifluoroacetate, 7.5 mL of OA, and 7.5 mL of ODE were added and the mixture was heated stepwise to 125 °C in 30 min under vacuum. After 1 h of core growth, 5 mL of the reaction mixture were taken and the shell solution was injected at a flow rate of 1.5 mL min$^{-1}$. Once the injection was completed, the reaction was allowed to proceed for 1 h more. The heating was then stopped and the UCNPs were purified following the procedure described in the previous paragraph. Eventually, the UCNPs were dispersed in toluene for further characterization. The final concentration of the stock sol was 57.6 mg/mL corresponding to an estimated molar concentration of 0.012 μM.

### 4.1.3 Characterization techniques

**Optical Properties.** Absorption spectra were acquired on a Varian Cary 5000 spectrophotometer, diluting the QD sol in toluene to an optical density below 1 throughout the whole measurement range. QD PL and UCL spectra were collected at room temperature using a lens at 90 ° angle from the excitation beam and recorded with an Avaspec-ULS2048L spectrometer (Avantes, Netherlands). UCL and QD emission were obtained under laser diode excitation at 980 nm (BTW, China) and LED excitation at 450 nm (Thorlabs, USA), respectively. In order to remove any stray light from the excitation sources a short pass 785 nm filter and long pass 500 nm filter (Semrock, Inc., USA) were used in the two cases. The optical density of QD sol was kept below 0.1 at the excitation wavelength. The UCL spectra were recorded using sols of UCNPs at a concentration of 0.1 mg/mL. The PLQY of QDs was calculated using an aqueous solution of $Ru(bpy)_3Cl_2$ as a standard (emission peak: 613 nm, PLQY = 0.042 ± 0.002). For the optical measurements of dried samples, a home-made confocal fluorescence microscope was employed. A single-mode fiber coupled laser diode (980 nm) was used as the excitation source and focused on the sample by using a microscope objective. Power densities on target varied between $1.4 \cdot 10^4$ W/cm$^2$ and $7.7 \cdot 10^4$ W/cm$^2$. The sample emission was collected with the same microscope objective. Emission and excitation light were discriminated by means of a dichroic mirror and a short-pass filter (FES0900, Thorlabs). The luminescence of the sample was collimated into the entrance of a high-resolution spectrometer and the signal was detected by a CCD detector (Synapse, Horiba). For lifetime (LT) measurements, the sample was excited by an optical parametric oscillator source (Spectra Physics) at 960 nm (corresponding to the maximum absorption of $Yb^{3+}$ ions in $LiYF_4$). The UCL signal at 450 nm was spectrally filtered (FESH0750, Thorlabs) and collimated into the entrance of a high-resolution spectrometer. The emission was amplified by a photomultiplier tube (R2949, Hamamatsu) and the UCL decay curves were recorded by means of a digital oscilloscope (LT372, LeCroy).

**Structure, morphology, and composition.** The crystalline structure of the samples was probed by means of XRPD with a Bruker D8 Advance Diffractometer using a CuKα radiation. The samples were prepared depositing few drops of the toluene solution of purified QDs or UCNPs on a glass slide and letting the solvent slowly evaporate in air. The morphology of the two structures was analyzed by means of TEM and HREM using a JEOL JEM 3010 microscope (1.7 Å point to point resolution at Scherzer defocus). Before the imaging, each sample was further diluted in hexane to an approximate concentration of 0.1 mg/mL and sonicated for 2 min. One drop of the solution was deposited on a carbon-coated nickel grid and the solvent was allowed to slowly evaporate in air.

## 4.2 Results and discussion

### 4.2.1. Material characterization

The QDs and UCNPs were characterized independently to obtain the information for the analysis of the energy transfer (ET) mechanism between them. The QDs have been synthesized intentionally introducing in the reaction environment a sub-stoichiometric amount of Cu$^+$. Actually, although it is not yet clear how the presence of Cu vacancies plays a role in the emission mechanism, the production of Cu-deficient QDs leads to an increased PLQY, as already discussed in Section 1.2. In this case, QDs display a PLQY of 11.5 % as obtained from the optical characterization (Figure 4.1a), which is in line with the state of the art CIS QDs[3]. Their crystalline structure is the typical tetragonal chalcopyrite (PDF #00-047-1372, Figure 4.1b). The morphology of the sample cannot be clearly distinguished from TEM observations, due to the poor contrast that this material gives rise to under the electronic beam (Figure 4.1c). However, crystalline fringes are clearly observed from the micrograph, confirming the good crystallinity of the sample. From these images the diameter of the QDs could only be estimated to fall between 3 and 4 nm. Both LYFYT and LYFY/LYFYT UCNPs have a tetragonal crystalline lattice (PDF #01-078-2179), as confirmed from the XRPD patterns (Figure 4.2a and 4.2d). They have a bi-pyramidal habitus, which is characteristic of LiYF$_4$ (Figure 4.2b and 4.2e)[4] and are well crystallized as can be inferred by the presence of extended crystalline fringes in TEM micrographs and strong diffraction spots in their electron diffraction patterns (Figure 4.2c, 4.2f and insets).

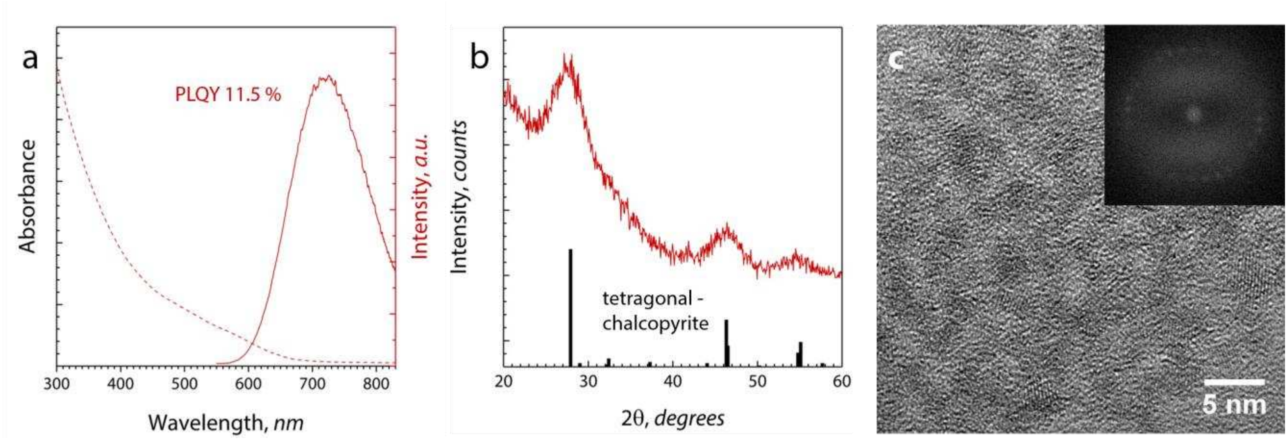

**Figure 4.1**. The optical absorption and emission of CIS are characterized by the typical features of CuInS$_2$ QDs: poorly resolved excitonic absorption features, large Stokes shift, and broad emission (*a*). The crystalline structure of these QDs was assigned to the tetragonal polymorph (*b*). TEM observations show small crystals with a characteristic size estimated to fall between 3 and 4 nm. The crystallinity of the sample is confirmed by the presence of lattice fringes and the diffraction spots in the Fourier transform of the image (inset).

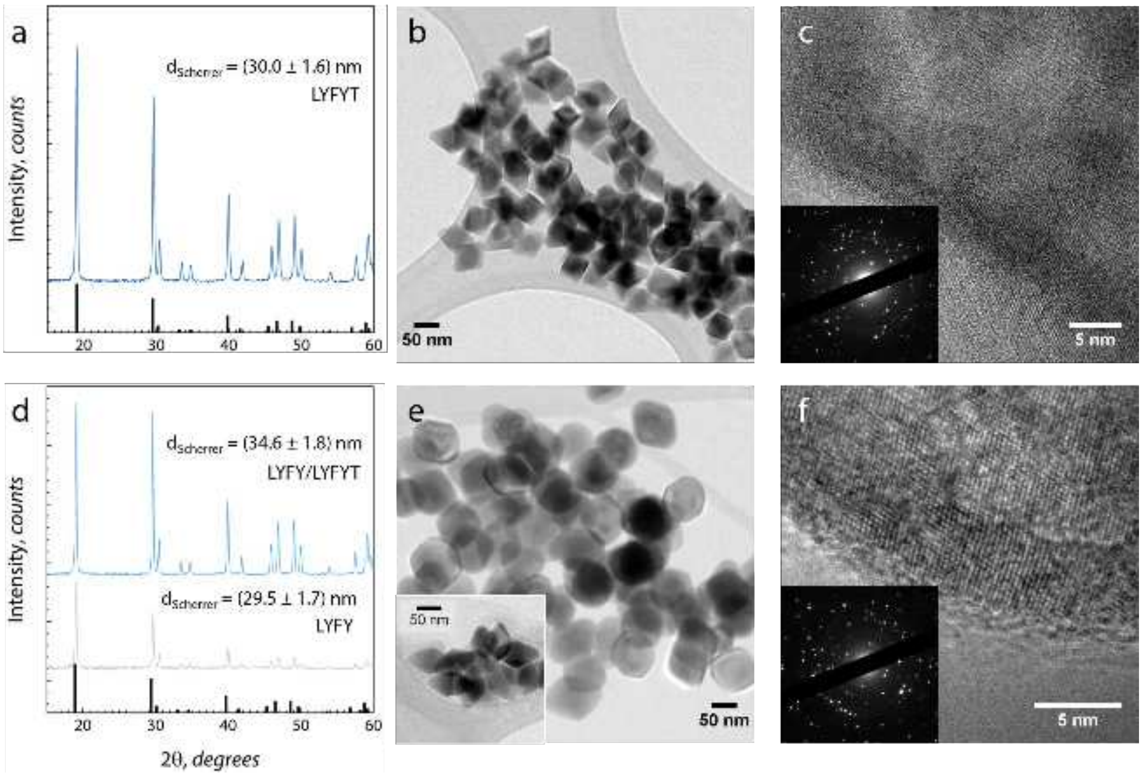

**Figure 4.2**. LYFYT, LYFY, and LYFY/LYFYT have a tetragonal crystalline structure (PDF #01-078-2179) (*a* and *d*). The crystallite size was estimated using the Scherrer equation to be approximately 30 nm for the core UCNPs and 35 nm for the final core/shell sample. From TEM images (*b* and *e*) a characteristic bi-pyramidal habitus is observable for both core and core/shell architectures (inset in *e* shows the core LYFY). The good crystallinity of the samples is confirmed by the presence of extended crystal fringes and diffraction spots in the electron diffractions (*c*, *f* and respective insets).

The core/shell structure of LYFY/LYFYT is confirmed by the comparison of the final sample with its core parent (Figure 4.2e and inset, respectively). Indeed, the final core/shell structure is bigger than the core itself and a single population of UCNPs can be observed from TEM images. The UCNPs were modeled as perfect square-based bi-pyramids and their characteristic lengths were obtained from TEM micrographs (Figure 4.3). The statistical analysis conducted considering 150 UCNPs per sample shows that the growth of the shell takes place preferentially along the *A* axis rather than longitudinally along *L* (Table 4.1). For the ease of the study, the shape of the sample LYFY/LYFYT has been considered to be a bi-pyramid with sharp vertexes. Nonetheless, it has to be noted that the TEM images show more rounded shapes, sometimes even truncated bi-pyramids. The approximation we are making does not affect the conclusions that will be made in this study.

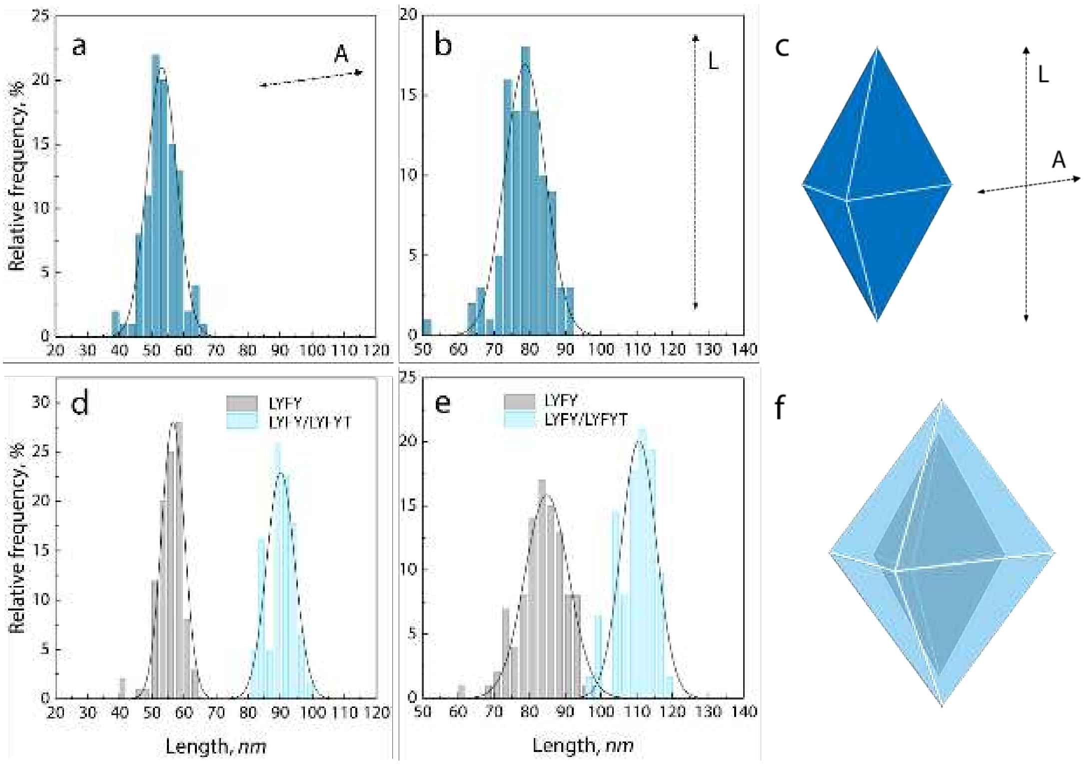

**Figure 4.3**. The size distribution was obtained for both samples modeling the UCNPs as perfect square-based bi-pyramids (*c* and *f*). The base edge (A – *a, d*) and total height (L – *b, e*) were measured from TEM images for LYFYT, LYFY, and LYFY/LYFYT. The growth of the shell leads to an increased size of both dimensions, with a more pronounced increase of the A edge.

The UCNPs have been designed in order to maximize the overlap of their emission with the absorption of the QDs, so to promote the ET. For this reason, $LiYF_4$ and $Tm^{3+}$ were selected respectively as the host material and the dopant ion. This combination gives a strong UCL in the UV-blue spectral range[2], which is perfectly suited for the excitation of QDs. The different emission of the two upconverting systems under 980 nm excitation is another indirect evidence of the presence of a core/shell system in the sample LYFY/LYFYT (Figure 4.4a and 4.4b). Both UCL spectra show the characteristic emission lines of $Tm^{3+}$ in $LiYF_4$, but the relative intensities of the bands vary considerably.

**Table 4.1.** A and L lengths obtained for LYFYT, LYFY, and LYFY/LYFYT from the measurements of 150 UNCPs.

| **Sample** | **A,** ***nm*** | **L,** ***nm*** |
|---|---|---|
| LYFYT | 53.3 ± 5.2 | 78.0 ± 7.1 |
| LYFY | 56.1 ± 3.9 | 84.0 ± 6.5 |
| LYFY/LYFYT | 89.6 ± 4.1 | 109.4 ± 5.0 |

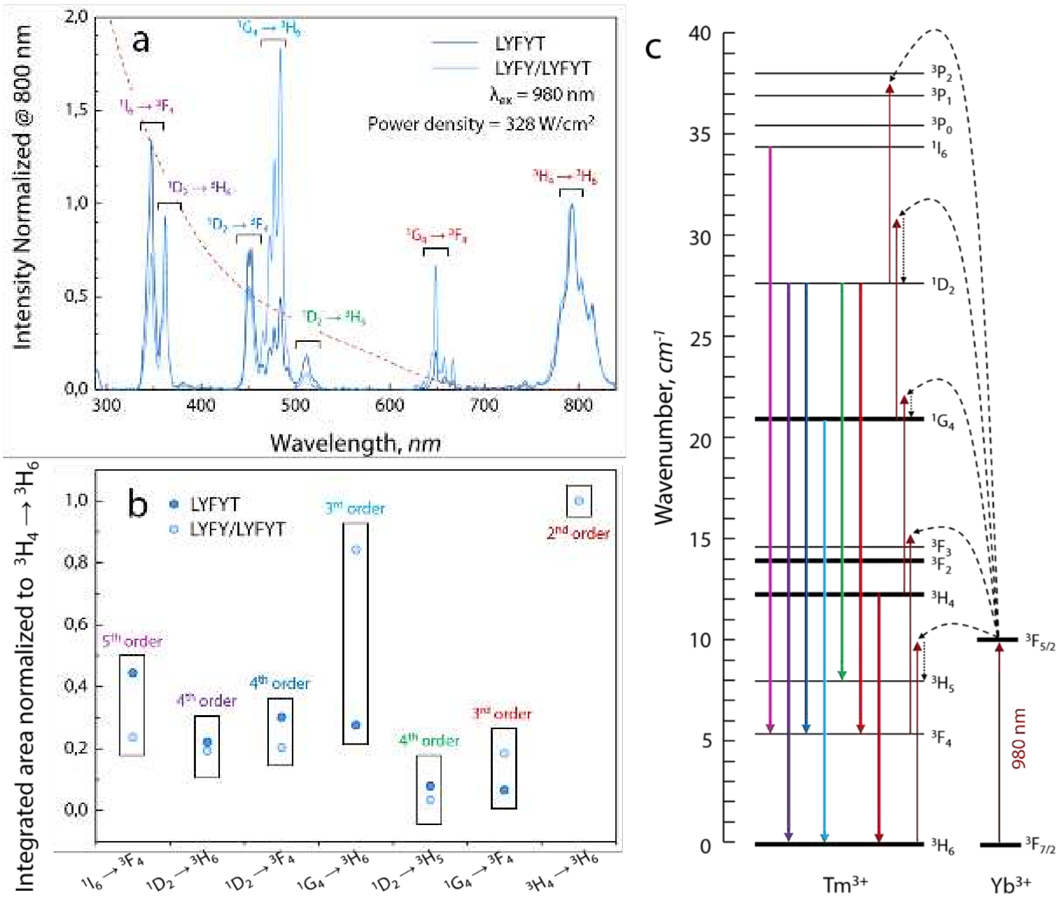

**Figure 4.4**. The UCL spectra of LYFYT and LYFY/LYFYT show the presence of the characteristic emissions stemming from the electronic transitions in $Tm^{3+}$ ions (*a* and *c*). The relative intensity of the bands is different depending on the architecture of the UCNPs (*b*). Higher photon order transitions (5th and 4th) have a lower intensity in the core/shell UCNPs with respect to the 3rd photon order ones due to efficient phonon-assisted de-excitation events taking place when the optically active ions of $Tm^{3+}$ are basically located at the UCNP surface. QD absorption is reported in *a* (red dashed line) for comparison with the UCL of the two UCNPs.

In particular the higher photon order emissions[2] (5th: $^1I_6 \rightarrow {}^3F_4$ - 4th: $^1D_2 \rightarrow {}^3H_6$, $^1D_2 \rightarrow {}^3F_4$, $^1G_4 \rightarrow {}^3F_4$) are effectively quenched in LYFY/LYFYT if compared with the 2nd ($^3H_4 \rightarrow {}^3H_6$) and 3rd photon order transitions ($^1G_4 \rightarrow {}^3H_6$, $^1G_4 \rightarrow {}^3F_4$) (Figure 4.4c). This behavior stems from the different distribution of $Tm^{3+}$ ions throughout the particle volume. In LYFYT these optically active centers are randomly distributed over the entire crystal, while in LYFY/LYFYT they occupy more superficial sites. This makes more likely electron trapping in surface states and it also promotes the interaction with solvent molecules, whose phonons promote non-radiative

---

[2] The UCL signal intensity, upconversion being a non-linear process, is dependent on the power of the excitation light, more precisely on the power density (*P*), according to a power law of the type $I \propto P^n$. Here, $n$ is the photon order of the transition and represents the minimum number of photons that should be absorbed by the material to observe that particular transition.

electron de-excitation events from higher energy levels[5, 6]. Nevertheless, the core/shell architecture is expected to lead to a major advantage: a larger fraction of $Tm^{3+}$ ions would be located at the UCNP surface with respect to the total amount of ions in the crystal. This, as we will see in the continuation of the discussion, increases the possibility of observing evidence of FRET.

### 4.2.2 Mathematical modelling of FRET

FRET is a mechanism through which energy is first absorbed by a donor species (UCNPs in this case) and it is transferred to an energy acceptor (here QDs). The distinctive feature of this ET mechanism is the non-radiative nature, meaning that there is no emission of photons from the donor but rather the energy is transferred according to a dipole-dipole type interaction between the two species[7]. One major requirement in order for this resonant transfer to take place is that donor and acceptor should be in close proximity. Donor-acceptor distance in FRET, the general expression to determine the Förster distance (*i.e.* the interparticle separation at which the transfer efficiency is 50%) is the following:

$$R_0^6 = \frac{9ln10\ PLQY_D k^2 J}{128\pi^5 n^4 N_A} \tag{4.6}$$

Where $N_a$ is the Avogadro constant ($6.2 \cdot 10^{23}$), $k^2$ is the dipole orientation factor, $PLQY_D$ is the photoluminescence quantum yield of the donor, $n$ is the refractive index of the medium, and $J$ is the spectral overlap integral. This last value is obtained from:

$$J = \frac{\int f_D(\lambda)\epsilon_A(\lambda)\lambda^4 d\lambda}{\int f_D(\lambda) d\lambda} \tag{4.7}$$

Where $f_D$ is the spectral profile of the donor emission and $\epsilon_A$ is the molar extinction coefficient of the acceptor. The presented NPs have been carefully designed in order to maximize the value of this last parameter, using UCNPs whose emission largely overlaps with the acceptors' (QDs) absorption (see Figure 4.4a). Given this, for the comprehension of the following discussion, it is useful to estimate the value of $R_0$ when using LYFYT or LYFY/LYFYT as donors. In these systems this distance could only be estimated considering approximate numerical values of some parameters. For instance, while the spectral profiles of both LYFYT and LYFY/LYFYT emission and QD absorption can be experimentally obtained, the actual extinction coefficient of the latter can only be estimated considering an approximate value of QD sol concentration (Figure 4.5a and 4.5d). From these assumptions, the role of donor PLQY, dipole orientation factor, and refractive index was explored (Figure 4.5b, c, e, f).

The determination of UCNP PLQY is a controversial subject[8, 9]; however, according to the literature, it is possible to consider PLQY values between 0.001% and 0.1% for UCNPs[8, 10], while higher values are obtainable with more sophisticated core/shell structures[11-14]. The low PLQY displayed by UCNPs in general makes the Förster radius very small in systems where these particles act the role of donors[15, 16]. The other parameter greatly affecting value of $R_0$ is $k^2$, which can take values $0 \leq k^2 \leq 4$. A value of 0.67 is used when the re-orientation of the dipoles are fast, so the acceptor's dipole can be considered isotropically oriented with respect to the donor (*i.e.* it is freely moving). In the case of rigidly fixed moieties, a value of 0.475 is generally accepted. In these simulations, particular $k^2$ values were taken into account (0.67, 1, 2, 4) to compare the results with those obtained by Bednarkiewicz et al. on a similar system[15].

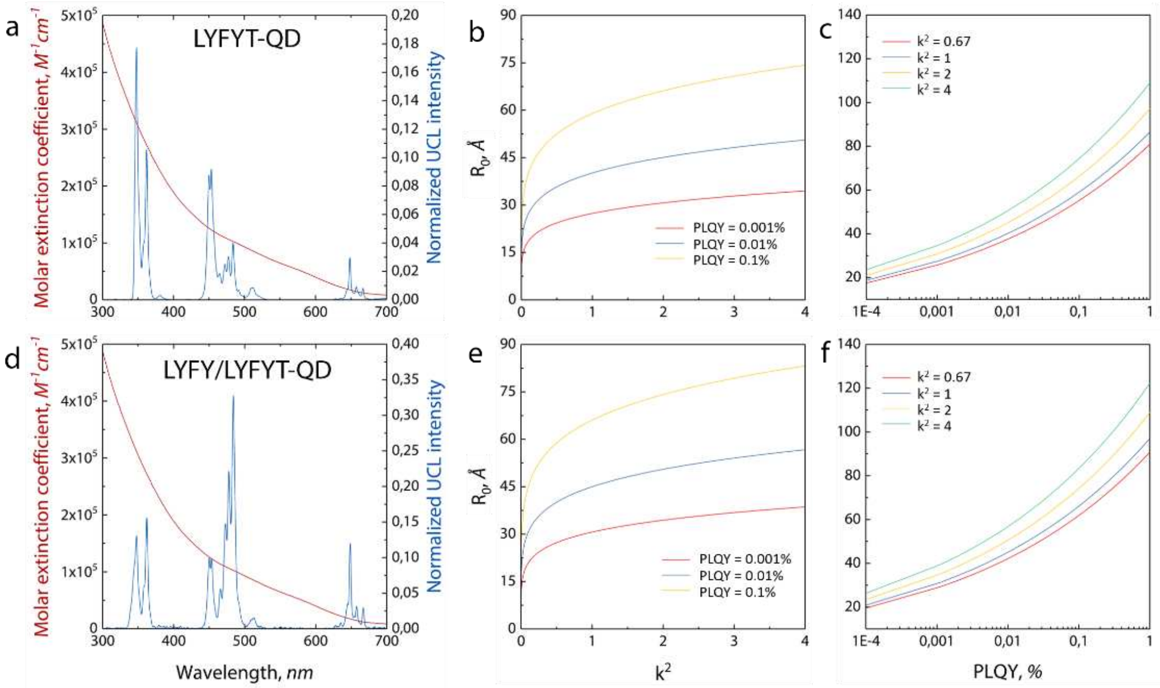

**Figure 4.5**. The spectral overlap between UCNP emission and QD absorption is large thanks to the presence of multiple UV-blue UCL bands that can effectively excite the QDs (*a* and *d*). The simulations of the $R_0$ varying the dipole orientation parameter ($k^2$ – *b* and *e*) and the PLQY of the donors (PLQY – *c* and *f*) return a Förster radius ranging between approximately 20 and 100 Å in both combinations.

However, it has to be observed that, due to the long LT of the UCL (hundreds of microseconds), the re-orientation of the dipoles can be considered fast enough to justify the use of a value of $k^2$ = 0.67. With respect to the aforementioned work, where the authors used $NaYF_4$:Yb,Er UCNPs and CdSe QDs, the better spectral overlap in our samples explains the larger $R_0$ values obtained in this study. With both LYFYT and LYFY/LYFYT the values are in the expected range for FRET (1-10 nm). It is worth noting that due to a larger spectral overlap integral, LYFY/LYFYT theoretically gives a larger $R_0$ than LYFYT (Figure 4.5), when the other parameters are fixed. However, the presence of a larger number of superficial $Tm^{3+}$ ions is expected to lead to a slightly lower PLQY in core/shell UCNPs or, more precisely, to a different distribution of the radiative energy among the different bands. As already pointed out, this stems from a higher probability of quenching phenomena taking place because of the proximity of the optically active centers to solvent molecules and trap sites. In these simulations the refractive index was assumed to be equal to that of toluene (n = 1.497), the solvent used to carry out the measurements in sol. Nonetheless, the effective refractive index is modulated by the presence of ligand molecules on the surface of QDs (DDT, *n* = 1.459) and UCNPs (OA, *n* = 1.459)[15]. This is particularly true considering the short distance at which FRET takes place, which is of the same order of magnitude of the ligands' chain length. The effect of the variation of the refractive index was investigated in the case of LYFYT considering a PLQY = 0.01% and $k^2$ = 0.67 (Figure 4.6). The results show that the variation of the Förster radius $R_0$ due to a refractive index change is of the order of less than 0.5 Å in the considered range, a value far smaller compared to the error made considering the aforementioned approximations.

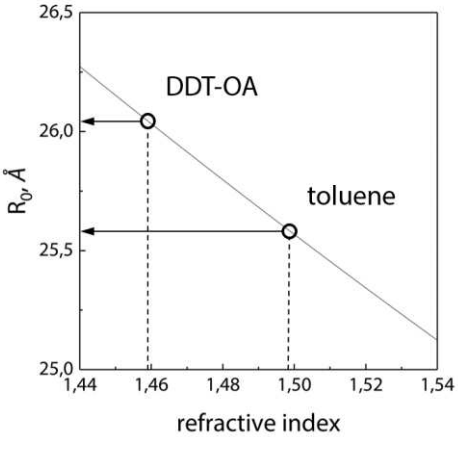

**Figure 4.6**. The refractive index of the medium separating the donor and the acceptor plays only a minor role in determining the Forster radius, in particular considering the relatively small difference of refractive index value displayed by the ligand molecules (DDT and OA) and the solvent (toluene).

The information obtained from these simulations will be also used below to interpret the results of the ET observed in dried samples.

### 4.2.3 Energy transfer in solution

**Effect of acceptor concentration.** In the literature only few reports can be found regarding the energy transfer from UCNPs to QDs in solutions. In particular silica was used by Li et al. to couple CdSe QDs and UCNPs[17] and Yan et al. synthesized OLAm-capped QDs in the presence of OA-capped UCNPs observing a sort of electrostatic interaction between the species[18]. Recently, Hong et al. observed that core/shell $NaYF_4$:Yb,Er/$NaYF_4$ can excite CIS/ZnS QDs when mixed together in the same sol[19]. However, none of these studies provided evidence of FRET. Eventually, Mattsson et al. in 2015 coupled Er-doped streptavidin-capped UCNPs and biotin-capped CdSe QDs, and studied the interaction of the two NPs in water[16]. The authors observed a slight decrease of UCL LT in the presence of QDs and the appearance of a weak emission feature ascribed to the acceptors, eventually using the nano-composite as a Vitamin H sensor.

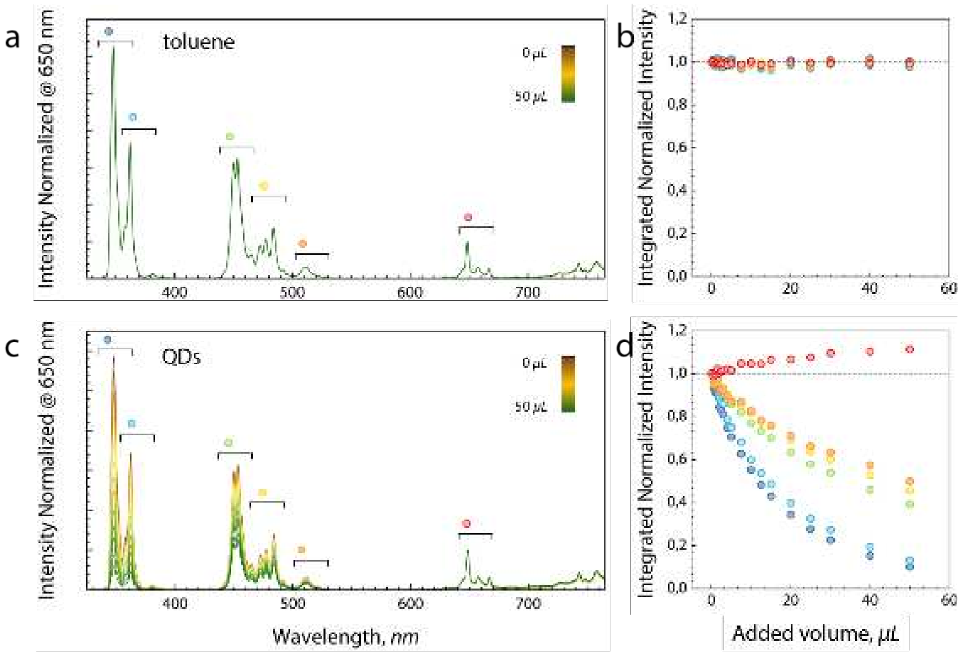

**Figure 4.7**. Upon addition of increasing volumes of QD stock sol, the emission of LYFYT is heavily quenched below 600 nm (*c*) while the dilution with toluene does not lead to appreciable changes in the UCL signal (*a*). The trend of the bands' integrated emission returns an intensity increase above 600 nm due to the appearance of QD emission in that wavelength range (*b* and *d*).

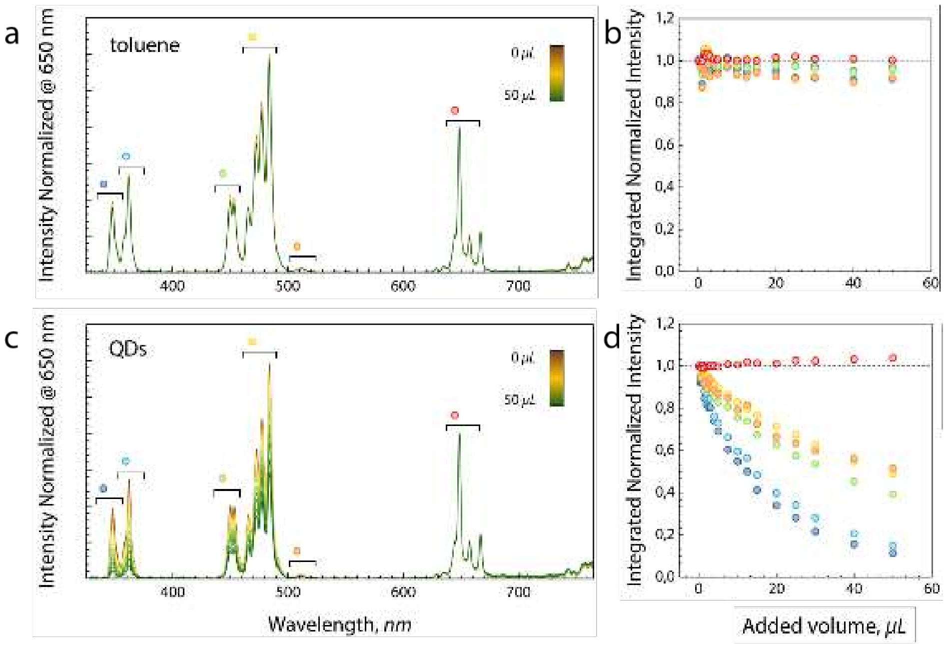

**Figure 4.8**. Similarly to what observed for LYFYT, upon titration with QD stock sol, the emission of LYFY/LYFYT is heavily quenched below 600 nm (*c*) while the dilution with toluene does not lead to appreciable changes in the UCL signal (*a*). In this case, the integration of the band intensity allows to clearly appreciate the quenching of the UCL signal, but the intensity increase above 600 nm is not as pronounced as in the case of LYFYT (*b* and *d*).

Following these observations, we first studied the ET mechanism in solution, with the aim of testing whether it is possible to observe the phenomenon of FRET from UCNPs (donors) to QDs (acceptors) when they are randomly distributed and free to move in a medium.

In fact, FRET is known to take place at very short distances, typically less than 10 nm, so the two moieties have to be in close proximity in order for the transfer to take place. For these experiments, working sols of the two UCNPs were diluted in toluene to a concentration of approximately 0.1 nM, a concentration also used in other studies on UCNP-QD FRET[16]. 2 mL of these sols were poured in a cuvette and the UCL signal was recorded upon titration with QD stock sol. As a control experiment, the UCL signal was monitored adding same volumes of pure toluene (Figures 4.7 and 4.8). As it can be observed, the relative intensity of $Tm^{3+}$ emission bands does not change when diluting the UCNPs with toluene, whereas there is a steep intensity decrease of the higher energy bands in the presence of increasing concentration of QDs.

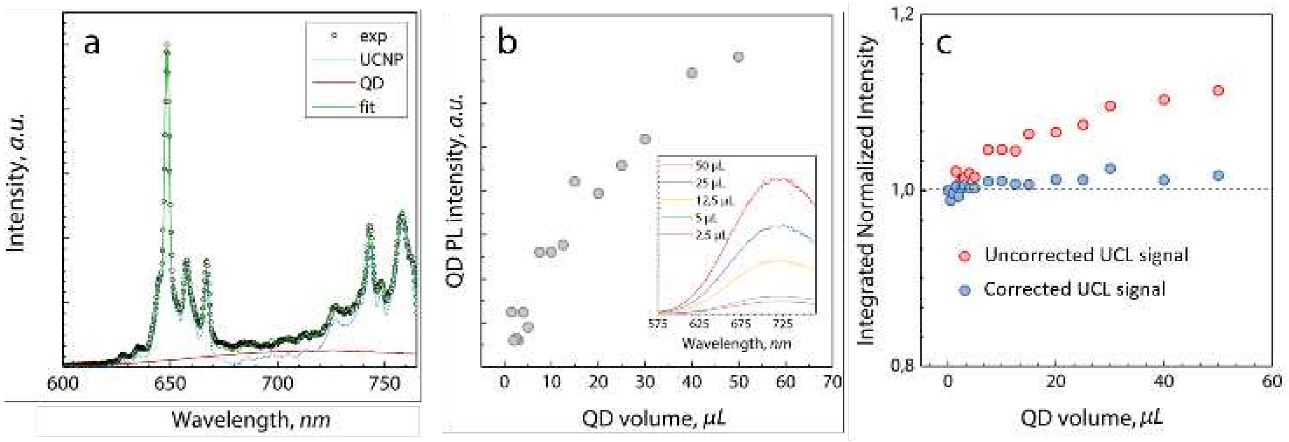

**Figure 4.9**. Using a linear combination of pure QDs and UCNPs it is possible to fit the emission signal coming from the mixture of these moieties (*a*). The information obtained from this fitting procedure can be used to have a quantitative estimation of the QD emission increasing the amount of these acceptors in the sol (*b*). The integrated signal of the QD emission was subtracted from the overall signal of the LYFYT-CIS mixture recorded in the $^1G_4 \rightarrow {}^3F_4$ range. Correcting the emission for the QD contribution, the UCL signal regains an expected constant value regardless of the amount of QDs introduced in the sol (*c*).

---

The information that can be obtained from the emission bands integration is two-fold and depends on the UCL band spectral position either below or above 600 nm, where CIS absorption and emission dominates respectively (see Figure 4.4a). First, the bands $^1I_6 \rightarrow {}^3F_4$ ($\lambda_{max}$ = 348 nm), $^1D_2 \rightarrow {}^3H_6$ ($\lambda_{max}$ = 362 nm), $^1D_2 \rightarrow {}^3F_4$ ($\lambda_{max}$ = 450 nm), $^1G_4 \rightarrow {}^3H_6$ ($\lambda_{max}$ = 484 nm), and $^1D_2 \rightarrow {}^3H_5$ ($\lambda_{max}$ = 513 nm) are progressively quenched increasing the QD content in the sol, the intensity of the higher energy transitions being more quenched due to the better overlap with QD absorption. The integrated intensity of $^1G_4 \rightarrow {}^3F_4$ ($\lambda_{max}$ = 648 nm) shows an opposite behavior: since the emission of QDs is centered in this spectral range, its contribution becomes steadily more appreciable upon addition of larger volumes of stock CIS sol. It has to be noted that the extent of UCL signal quenching is identical using both LYFYT and LYFY/LYFYT, instead CIS emission is far less appreciable using UCNPs with the core/shell architecture. This is a result of the lower PLQY expected for this sample with respect to that of LYFYT that determines a less efficient UCL emission in the ultraviolet (UV) region, thus a less effective excitation of CIS QDs. Due to this difference in the behavior of LYFYT-QD and LYFY/LYFYT-QD combinations, the signal in the region that goes from 600 to 750 nm was more thoroughly analyzed only for the former UCNP-CIS combination. The overall emission spectrum of the mixed UCNPs and QDs sol can be deconvolved using a linear combination of pure LYFYT and CIS spectra respectively (Figure 4.7a). The method relies on determining the weighting coefficients for the spectra of the two species that minimize the squared residuals $S$[20]:

$$S = \sum_i (I_{i,obs} - I_i)^2 = \sum_i \left[(I_{i,obs} - (aU_i + bQ_i)]^2\right] \tag{4.1}$$

Where $I_{obs}$, $U$, and $Q$ are respectively the observed intensities of the mixed sol, the UCNPs alone, and pure QDs. The subscript $i$ stands for the $i$-th wavelength, whereas $a$ and $b$ are the weighting coefficients for the UCNP and QD emission spectra respectively. The linear combination of these spectra gives the calculated spectrum $I$. The condition to be imposed in order to minimize $S$ is that the first derivative of this quantity with respect to the weighting coefficients is equal to zero:

$$\frac{\partial S}{\partial a} = \frac{\partial S}{\partial b} = 0 \tag{4.2}$$

This condition leads to the homogeneous system:

$$\begin{pmatrix} \sum_i U_i^2 & \sum_i U_i Q_i \\ \sum_i Q_i U_i & \sum_i Q_i^2 \end{pmatrix} \begin{pmatrix} a \\ b \end{pmatrix} = \begin{pmatrix} \sum_i U_i I_{i,obs} \\ \sum_i Q_i I_{i,obs} \end{pmatrix} \tag{4.3}$$

And, rearranging:

$$\begin{pmatrix} a \\ b \end{pmatrix} = \begin{pmatrix} \sum_i U_i^2 & \sum_i U_i Q_i \\ \sum_i Q_i U_i & \sum_i Q_i^2 \end{pmatrix}^{-1} \begin{pmatrix} \sum_i U_i I_{i,obs} \\ \sum_i Q_i I_{i,obs} \end{pmatrix} \tag{4.4}$$

Using this approach, it is possible to separate the contribution to the total emission coming from CIS QDs (Figure 4.7b). This data was used to correct the integrated signal observed in the region characteristic of the $^1G_4 \rightarrow {}^3F_4$ electronic transition ($\lambda_{max}$ = 648 nm). As expected, it was observed that, upon subtraction of the QDs' contribution, the integrated area of this band remains constant when increasing CIS QD concentration (Figure 4.7c). The QD integrated emission was also used to interpret the nature of the ET mechanism. Actually, in the framework of ET phenomena, one can have an indication of the type of ET that is taking place between the two moieties by plotting the acceptor emission intensity versus the mean interparticle distance ($R$).

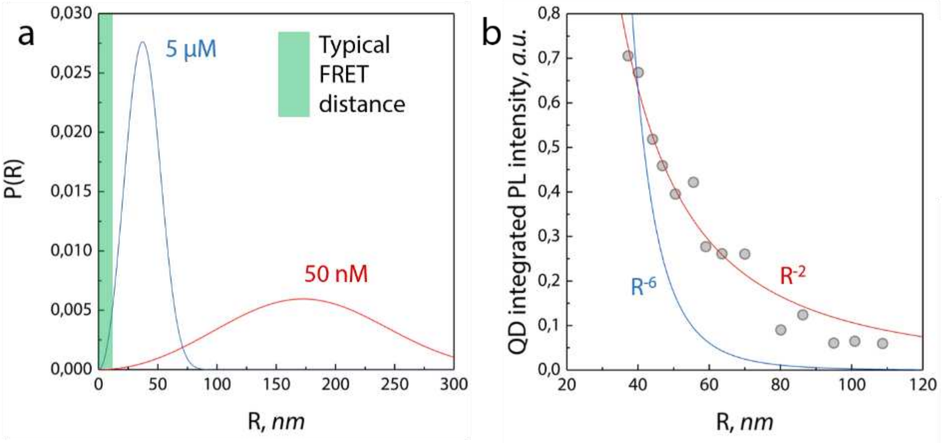

**Figure 4.10**. The calculation of the nearest neighbor interparticle distance in the two cases of minimum and maximum QD concentration returns respectively a mean value of 110 and 40 nm ($a$). These values are large compared to the usual distances observed for systems that can give rise to FRET (green area in $a$ from 1 to 10 nm). The fit of the QD integrated intensity versus the mean interparticle distance is reasonable only considering a $R^{-2}$ dependence rather than $R^{-6}$.

---

A $R^{-2}$ dependence is characteristic of radiative phenomena, while a dependence upon $R^{-6}$ is typical of non-radiative (FRET-like) mechanism, due to the dipole-dipole nature of the interaction between the moieties characterizing this latter phenomenon. In the case under study, the mean interparticle distance distribution ($P$) between donors and acceptors in the sol was estimated utilizing the formula:

$$P(R) = \frac{3}{a}\left(\frac{R}{a}\right)^2 e^{-\left(R/a\right)^{1/3}} \tag{4.5}$$

Where $R$ is the mean interparticle distance of the nearest neighbors and $a$ is the so-called Weigner-Seitz radius (Figure 4.10a). This parameter is a function of the particle density $n$, according to the following relation:

$$a = \left(\frac{3}{4\pi n}\right)^{\frac{1}{3}} \tag{4.5}$$

This parameter corresponds to the mean volume per particle in the system. In our particular case, the particle density corresponds to the concentration of UCNPs and QDs together, with the largest contribution to this value coming from CIS QDs.

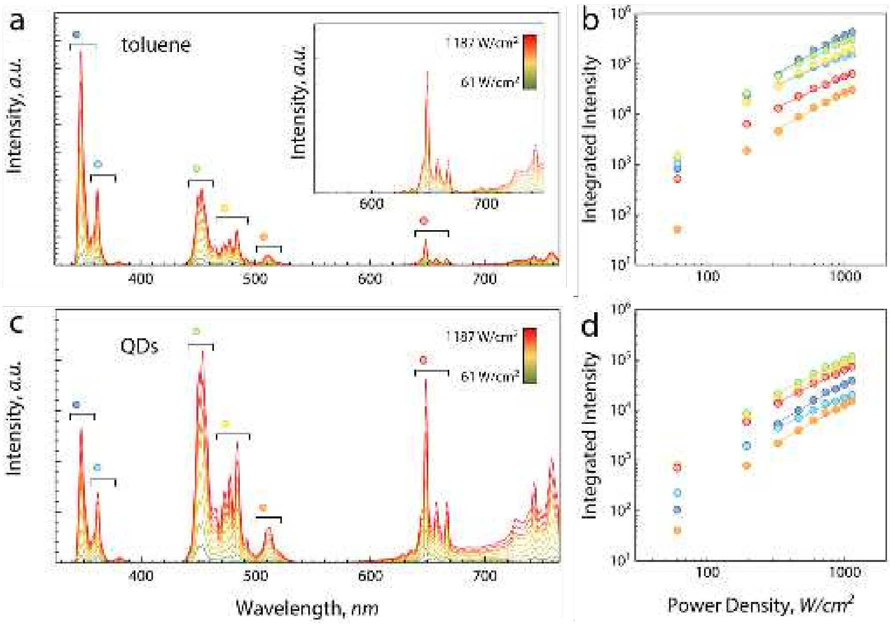

**Figure 4.11**. The overall LYFYT UCL intensity of the higher order transitions is lower in the presence of CIS QDs (50 μL of the stock solution) than that of UCNPs alone (*a* and *c*). In both cases the log-log plot (intensity vs. power density) for the bands evidenced in the UCL spectra follow a linear trend (*b* and *d*). The fit has been performed considering the values obtained starting from a power density of 328 W/cm$^2$, where the signal-to-noise ratio is high enough to have an integrated intensity value not affected by considerable uncertainty.

---

The distribution peak in this approximation is given by $R_{max}$ = 0.874$a$ and the QD PL intensity was plotted against these values. In our case, the experimental data is conveniently described with a $R^{-2}$ dependence rather than using $R^{-6}$ (Figure 4.10b), thus suggesting a radiative mechanism taking place in the sol. This observation could be anticipated by observing the interparticle distance distribution curves. Even at the highest concentration tested, only a small fraction of the particles falls in the range where FRET usually takes place (*i.e.* below 10 nm).

**Effect of excitation power density.** As previously pointed out in the text, the characteristic of the upconversion process is its sensitivity to the excitation power, because of its non-linear nature. Due to this characteristic, it was tested whether a variation of the power density led to differences in the optical behavior of UCNPs and the intensity of QD emission (Figure 4.11 and 4.12). In this view, Tm$^{3+}$ emission bands were integrated and their intensity plotted versus the excitation power density in a log-log graph, which usually returns a linear trend due to the aforementioned power law governing these phenomena. In particular, the slope of the fitting lines should match the photon order of that particular transition.

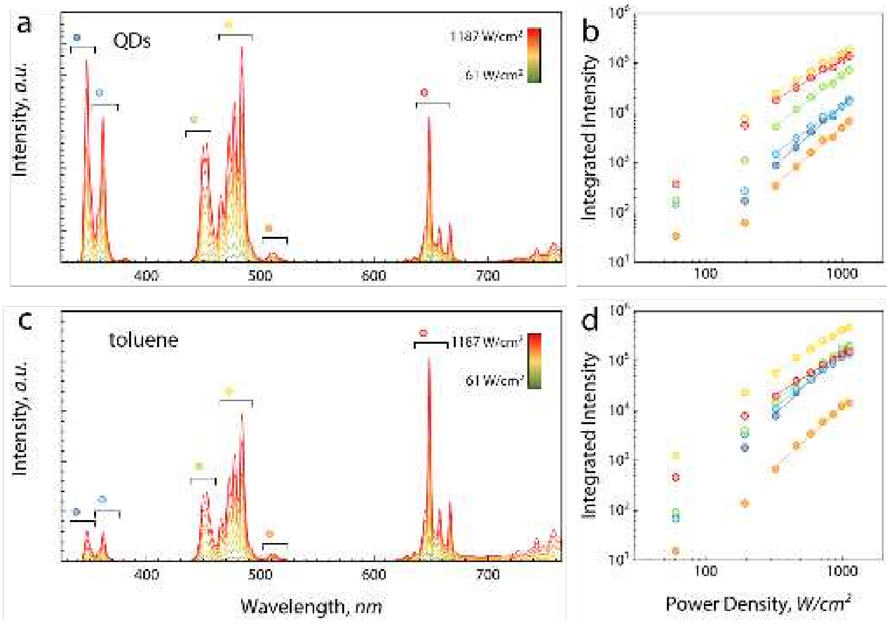

**Figure 4.12**. The overall LYFY/LYFYT UCL intensity of the higher order transitions is lower in the presence of CIS QDs (50 μL of the stock solution) than that of UCNPs alone (*a* and *c*). In both cases the log-log plot (intensity vs. power density) for the bands evidenced in the UCL spectra follow a linear trend (*b* and *d*). The fit has been performed considering the values obtained starting from a power density of 328 W/cm$^2$, where the signal-to-noise ratio is high enough to have an integrated intensity value dot affected by considerable uncertainty.

---

Here, the data was linearly fitted and the results obtained from this procedure were compared in the presence or absence of 50 μL of CIS QDs (Figure 4.11 and 4.12). The absolute intensity of the bands absorbed by QDs is always lower when these acceptors are present in the sol compared to pure LYFYT or LYFY/LYFYT sols. However, the slope of the fitting curves does not change in the two cases, indicating that the presence of energy acceptors in solution does not affect the optical properties of UCNPs (Figure 4.13). It is worth noting that for LYFYT the slope values are lower than expected, since in the chosen experimental conditions we are in the saturation regime, where the slope is approximately equal to the unity. In the case of LYFY/LYFYT the values are higher than in LYFYT but still lower than the theoretical values. However, their trend somehow follows the one of the transitions' order (see Figure 4.4). To have a more precise description of the effect of the excitation power density, the linear combination presented in Equation 4.4 was used to obtain the relative intensities of QD and LYFYT emission by taking the ratio between the weighting coefficients $b/a$ (Figure 4.14a). The increase of this ratio is a consequence of the different dependence of the bands' intensity on the excitation light power (Figure 4.9b).

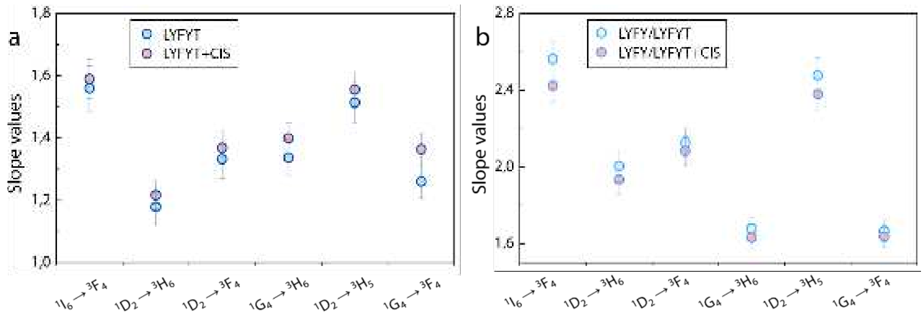

**Figure 4.13**. The slopes of the curves used to fit the data in Figure 4.11 and 4.12 does not match the photon order of the transitions. This is particularly true for LYFYT, where a saturation regime is already reached throughout the entire measurement range (*a*). LYFY/LYFYT shows instead a trend somehow following the one of the transition photon order (*b*). The presence of QDs does not influence the dependence upon the power of $Tm^{3+}$ transitions.

---

The $^1I_6 \rightarrow ^3F_4$ band ($\lambda_{max}$ = 348 nm) has the strongest dependence on the excitation power and, since it is the band that better overlaps with QDs' absorption, it has the greatest influence on their emission. Actually, the intensity ratio among this transition and the lower order $^1I_6 \rightarrow ^3F_4$ and $^1I_6 \rightarrow ^3F_4$ has a trend which is analogous to that displayed by the $b/a$ ratio (Figure 4.14b). This observation makes reasonable the use of high energy densities to investigate the transfer mechanisms: even if one is working in the UCNP saturation regime, the stronger UV-blue emission from LYFYT and LYFY/LYFYT increases the likeliness of FRET to be observed.

### 4.2.4 Energy transfer on dried samples

Due to the short interaction range that is required to observe FRET, the behavior of samples in their dried form was investigated. A first study of ET between UCNPs and QDs in powder form was conducted by Nguyen et al., who coupled commercially available upconverters and QDs of different sizes[21]. Later, Hong et al. designed a photodetector based on UCNPs and CIS/ZnS QDs[19]. Nonethelss, only Bednarkiewicz et al. studied the ET mechanism taking place between the two species, observing FRET evidence[15]. In their study they used $NaYF_4$:Yb,Er as donors and CdSe QDs as acceptors. The present study differs in the improved design of the two moieties, which should provide greater FRET efficiency thanks to three major differences that have been already mentioned in the discussion. First, the UV-blue emission of $LiYF_4$:Yb,Tm is more suitable for the excitation of QDs than $Er^{3+}$ green emission because of the larger spectral overlap with the QD absorption spectrum.

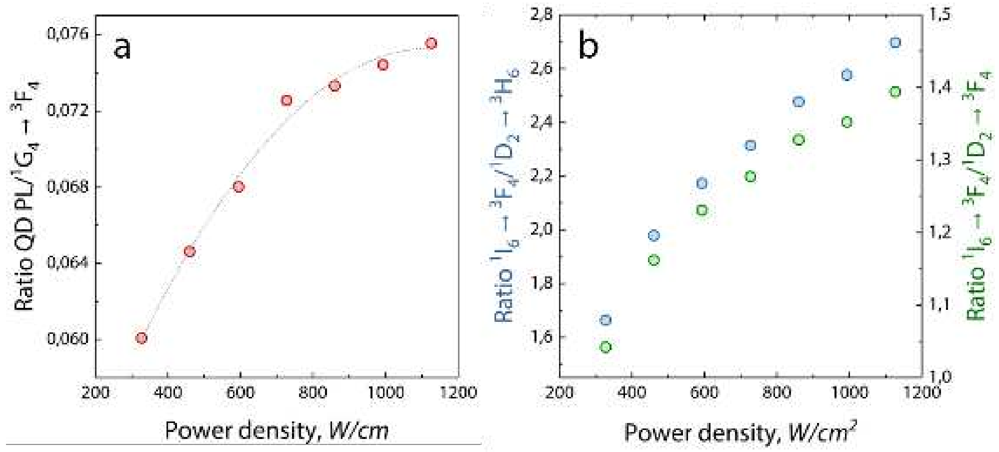

**Figure 4.14**. The emission intensity of the QDs indirectly excited through LYFYT UCNPs increases with the power density (*a*). This behavior is a consequence of the same trend displayed by the higher photon order emission bands of LYFYT with respect to the lower order ones. For instance, this is the case of the 5th order $^1I_6 \rightarrow {}^3F_4$ with respect to the 4th order $^1D_2 \rightarrow {}^3H_6$ and $^1D_2 \rightarrow {}^3F_4$ transitions (*b*).

---

Second, it has to be reminded that strictly speaking the donors are the emitting ions in the UCNPs and not the UCNPs themselves. In this regard, the core/shell architecture of LYFY/LYFYT UCNPs is expected to increase the number of emitting centers on the surface of the UCNPs with respect to those in the core of the structure. Actually, the emission of the ions located at the crystal surface would experience a LT shortening, unlike the emission of the ions in the core of the UCNP. Thus, an increased fraction of superficial ions ultimately leads to a more noticeable overall UCL LT shortening. Third, the relatively large Stokes shift that characterizes CIS QDs reduces self re-absorption phenomena, thus the acceptor emission is expected to be poorly quenched by the presence of even large amounts of acceptors themselves. Given this, the behavior of the same UCNPs-QDs combinations tested in sols was also investigated drying the samples on a solid substrate. Specifically, 10 µL of LYFYT and LYFY/LYFYT sols were cast on a glass slide and they were allowed to dry out at room temperature. At the same time, UCNPs and QDs in toluene were mixed and sonicated for few seconds before depositing 10 µL of the mixture on a glass slide. In this configuration donors and acceptors are in close contact, the ligand molecules on their surface being the only spacers among the moieties. The UCL signal was recorded both from dried UCNPs and mixtures of UCNPs and QDs (Figure 4.15a and 4.15c). In the presence of the QDs the UCNP emission below 600 nm is heavily quenched and the QD PL signal appears both with LYFYT and LYFY/LYFYT.

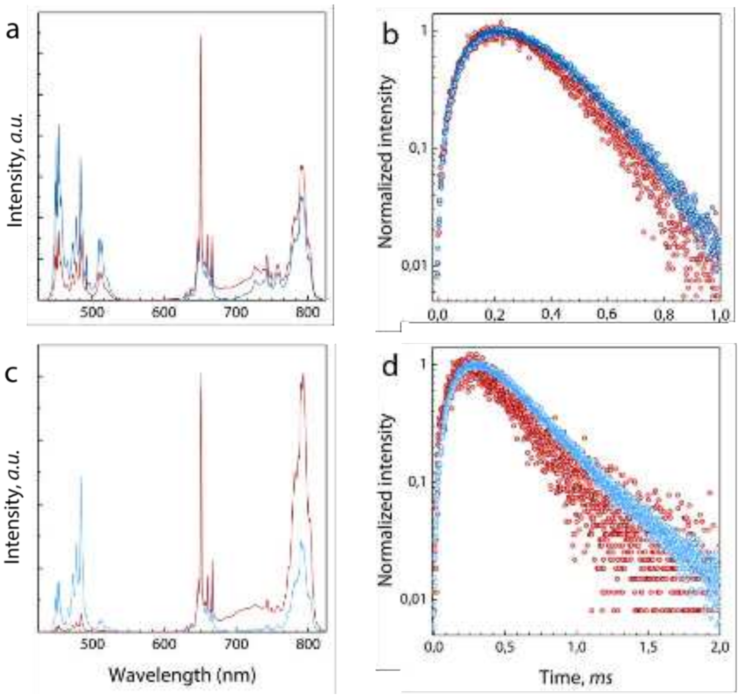

**Figure 4.15.** When UCNPs and QDs are mixed in solution and then dried on a glass slide, the emission under 960 nm excitation shows quenching of the high photon order transitions and the appearance of the QD PL emission band (*a* and *c*). The PL decay of $^1D_2 \rightarrow {}^3F_4$ $Tm^{3+}$ transition in the presence of the QDs experiences a shortening of the characteristic LT, due to FRET taking place between UCNP donors and the acceptors (*b* and *d*). LYFY/LYFYT LT is longer than LYFYT LT: this is explained in light of a more extended crystalline structure in the former architecture. The presence of $Yb^{3+}$ ions distributed both in UCNP core and shell promotes energy migration among these ions on a longer time scale before the energy could be transfer to a $Tm^{3+}$ ion in the shell.

These same samples were used to conduct time-resolved PL studies, in order to assess whether the UCL LT of UCNPs is reduced when the donors and acceptors are in intimate contact. This evidence would provide the final proof of FRET taking place, since radiative ET does not involve a decrease of the donor LT instead. The LT of the emission stemming from the transition $^1D_2 \rightarrow {}^3F_4$ of $Tm^{3+}$ ions was analyzed ($\lambda_{max}$ = 520 nm), since this is one of the emission bands affected the most by the quenching in the presence of QDs. Indeed, when the QDs are present together with the UCNPs, the decay curves show a shorter PL LT of this transition in both LYFYT and LYFY/LYFYT indicating the existence of a non-radiative transfer process (Figure 4.15b, 4.15d and Table 4.2). It is interesting to note that the LT decrease is more pronounced in core/shell UCNPs. This evidence confirms the hypothesis that an increased fraction of active centers located at the UCNP surface (*i.e.* close to the acceptors) allows for a better observation of the LT decrease. It is also worth noticing that the LT of LYFY/LYFYT is longer than that of LYFYT.

**Table 4.2.** LT values obtained from the fit of UCL decay curves in Figure 4.15 and the corresponding values of FRET efficiency, Förster radius, and donor-acceptor distance.

| Sample | τ, $\mu s$ | FRET efficiency, % | $R_0$, $\AA$ | R, $\AA$ |
|---|---|---|---|---|
| LYFYT | 411 ± 11 | - | - | - |
| LYFYT+QDs | 368 ± 7 | 10.5 | 26.0 | 37.2 |
| LYFY/LYFYT | 634 ± 14 | - | - | - |
| LYFY/LYFYT+QDs | 515 ± 6 | 18.8 | 29,2 | 37.3 |

In fact, although non-radiative de-excitation events are more likely in the former architecture, the presence of $Yb^{3+}$ ions in the core of the structure promotes energy migration on a longer time scale (*i.e.* longer LT). This can be understood in light of the fact that these energy migration events taking place in the core are only terminated by ET to $Tm^{3+}$ ions or electron trap in defect –surface- states, and both these species are located in the shell. The LT values obtained in the two combinations were used to estimate the FRET efficiency and, from that, the actual distance at which the two moieties are interacting according to the equation:

$$\eta = 1 - \frac{\tau'_D}{\tau_D} = \frac{R_0^6}{R_0^6 + R^6} \tag{4.8}$$

The FRET efficiency is 10.5 % and 18.8 % for LYFYT and LYFY/LYFYT respectively. Considering for both UCNPs a PLQY of approximately 0.01 %, a $k^2$ value of 0.67, and a refractive index of 1.459 (that of OA and DDT), values of Förster radius $R_0$ of 26.0 Å and 29.2 Å are obtained for LYFYT and LYFY/LYFYT respectively. These values return a distance between the moieties of 37.2 Å and 37.3 Å. The values obtained here are slightly larger than the results obtained from Bednarkiewicz et al., who found a value of approximately 15 Å for the Förster radius and a distance between the moieties of approximately 20 Å. A distance of approximately 37 Å suggests that FRET takes place to the QDs from $Tm^{3+}$ ions occupying the very first few nanometers of the crystal surface. Although the improved design of the system, the transfer efficiency we observed in this study is of the same order of magnitude of that observed in the system composed of $NaYF_4$:Yb,Er and CdSe QDs (14.8 %). This fact can be interpreted in light of the higher dilution of the ions in the crystalline lattice in the case of $Tm^{3+}$. This ion is characterized by the presence of a number of closely spaced electronic levels that can easily give rise to cross relaxation phenomena, thus depopulating high photon order levels[22]. For this reason, the optimized doping level for observing UCL from this ion is 0.5 %, which is a value 4 times lower than that of $Er^{3+}$ (2 %), in order to avoid the presence of $Tm^{3+}$ in close proximity. Considering the case of LYFYT it is possible to estimate the fraction of $Tm^{3+}$ ions that can take part in the FRET mechanism. $LiYF_4$ has a tetragonal lattice where the ratio between the long and short edges of the unit cell ($c/a$) is close to 2 and each unit cell contains four formula units (*i.e.* 4 Li, 4 Y, 16 F). So it is possible to consider the unit cell as composed of two cubic sub-cells of edge $a$, each containing two formula units. Taking a cell edge $a$ = 5.2 Å (according to PDF #01-078-2179) it is possible to estimate the number of sub-cells in a single UCNP using the dimensions determined from TEM micrographs (Table 4.1). The volume of a single UCNP is $7.39 \cdot 10^7$ Å$^3$ which gives $5.25 \cdot 10^5$ sub-cells per UCNP, corresponding to 5253 $Tm^{3+}$ ions. Now, taking into account a Förster radius of 24.6 Å, it turns out that approximately 26 % of these ions can effectively contribute to the FRET (*i.e.* their LT would experience a shortening). This means that the majority of $Tm^{3+}$ ions (74 %) will not experience a LT shortening in the presence of QDs and their emission will display the usual decay rate. This observation explains the difficulty in observing a considerable decrease of the UCL LT. Moreover, the use of QDs as acceptors pose another problematic in that they are bulkier than commonly used organic dyes. This means that using QDs one can accommodate less acceptors on the surface of the UCNP even in a close packing arrangement; an issue that is overcome by the large absorption cross section of QDs.

### 4.2.5 Ongoing experiments

Moving from the considerations just made, more UCNPs samples have been synthesized to promote a better interaction between a larger fraction of $Tm^{3+}$ ions and the QDs. In particular smaller $LiYF_4$:Yb,Tm UCNPs (Figure 4.16) and core/shell $LiYF_4$:Yb/$LiYF_4$:Yb,Tm having a thinner shell have been synthesized. These architectures are expected to allow for a more pronounced UCL LT shortening even though the low PLQY, due to the large surface to volume ratio, might make the FRET observation challenging. The time-resolved measurements will be repeated varying the relative amount of donors and acceptors, and using the new UCNPs, in order to determine the best parameters in terms of UCNPs coverage with QDs. The information obtained from these experiments will be used to select the optimized UCNPs-QDs combination to give rise to FRET.

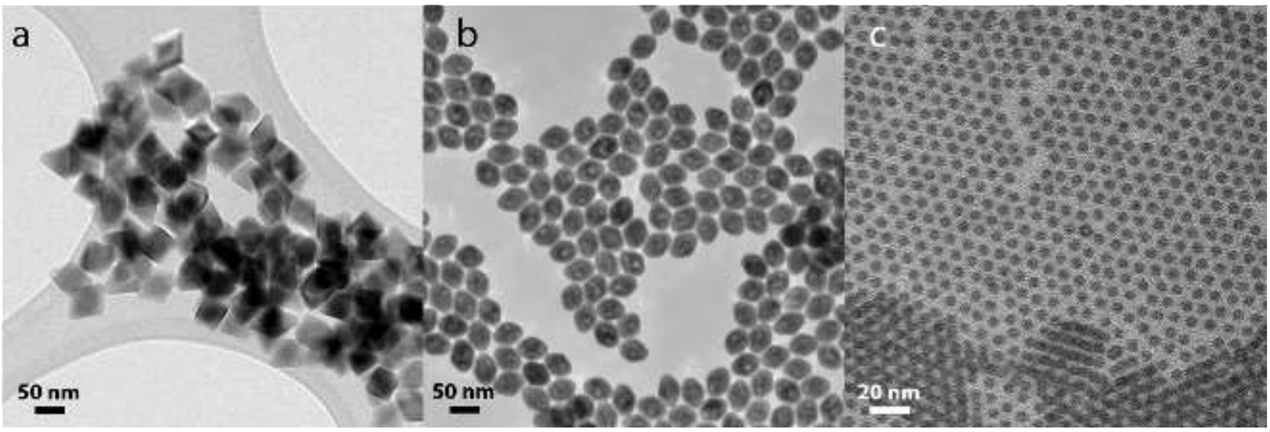

**Figure 4.16.** LYFYT (*a*) and smaller $LiYF_4$:Yb,Tm UCNPs (*b* and *c*) synthesized to increase the fraction of $Tm^{3+}$ ions on the UNCP surface. The increased surface to volume ratio is expected to increase the number of $Tm^{3+}$ ions whose emission would be affected by LT shortening due to FRET taking place to QDs.

---

In this way, it will be possible to build a nano-composite where, upon proper surface modification of the moieties, UCNPs and QDs are bound together and dispersed in water. Once properly tailored, such a system could potentially be used as a robust all-inorganic luminescent sensor in FRET-based bio-assays.

## 4.3 Conclusions

In this work the energy transfer (ET) mechanism between UCNPs (energy donors) and CIS QDs (energy acceptors) has been investigated. The two moieties have been designed in order to increase the chance of ET to take place. For this reason, $LiYF_4$ and $Yb^{3+}$-$Tm^{3+}$ have been respectively selected as the UCNP host and doping ions. This combination allows for a strong UV-blue UCL that can effectively excite CIS QDs. Moreover, a UCNP core/shell architecture was conceived in order to increase the fraction of $Tm^{3+}$ ions on the surface of the donor. This structure increases the number of $Tm^{3+}$ that can transfer the energy to QDs close to the UCNP surface. Eventually, the use of CIS QDs reduces the acceptor self-absorption phenomena due to the large Stokes shift that characterizes these QDs. The study of the ET phenomenon in sols showed that the random motion of the two moieties in the medium does not allow for a sufficiently close proximity between donors and acceptors to observe non-radiative (FRET-like) energy transfer even at high concentrations of QDs. The QD PL signal that can be observed upon irradiation with a 980 nm laser stems from the re-absorption of UCL emission, as can be deducted from the dependence of this signal intensity on the square power of the mean interparticle distance. More interestingly, evidences of FRET were observed when UCNPs and QDs were dried on a substrate, thus forced to closely pack. In this configuration, the proximity of the two moieties allows for FRET to take place, as confirmed by time-resolved UCL studies. The relatively low transfer efficiency (10.5 % and 18.8 % respectively for core and core/shell UCNP architectures) can be explained in light of the small fraction of optically active ions present in the first few superficial nanometers of the UCNPs and the presence of an unquenched signal coming from the ions in the core of the donor. The results obtained from these analyses have been used to improve the design of the system: in particular, UCNPs with an increased surface to volume ratio have been synthesized in order to further investigate FRET from these particles to QDs.

## References

1. Förster, T. *Annalen der Physik* **1948,** 437, (1-2), 55-75.
2. Mahalingam, V.; Vetrone, F.; Naccache, R.; Speghini, A.; Capobianco, J. A. *Adv Mater* **2009,** 21, (40), 4025-4028.
3. Chen, B.; Zhong, H.; Zhang, W.; Tan, Z. a.; Li, Y.; Yu, C.; Zhai, T.; Bando, Y.; Yang, S.; Zou, B. *Adv Funct Mater* **2012,** 22, (10), 2081-2088.
4. Kim, S. Y.; Won, Y. H.; Jang, H. S. *Sci Rep* **2015,** 5, 7866.
5. Johnson, N. J.; He, S.; Diao, S.; Chan, E. M.; Dai, H.; Almutairi, A. *J Am Chem Soc* **2017,** 139, (8), 3275-3282.
6. Shen, B.; Cheng, S.; Gu, Y.; Ni, D.; Gao, Y.; Su, Q.; Feng, W.; Li, F. *Nanoscale* **2017,** 9, (5), 1964-1971.
7. Demchenko, A. P., *Introduction to Fluorescence Sensing*. Springer Science: 2009.
8. Boyer, J. C.; van Veggel, F. C. *Nanoscale* **2010,** 2, (8), 1417-1419.
9. Liu, Q.; Sun, Y.; Yang, T.; Feng, W.; Li, C.; Li, F. *J Am Chem Soc* **2011,** 133, (43), 17122-17125.
10. Wisser, M. D.; Fischer, S.; Maurer, P. C.; Bronstein, N. D.; Chu, S.; Alivisatos, A. P.; Salleo, A.; Dionne, J. A. *ACS Photonics* **2016,** 3, (8), 1523-1530.
11. Bagheri, A.; Arandiyan, H.; Boyer, C.; Lim, M. *Adv Sci* **2016,** 3, (7), 1500437.
12. Chen, G.; Damasco, J.; Qiu, H.; Shao, W.; Ohulchanskyy, T. Y.; Valiev, R. R.; Wu, X.; Han, G.; Wang, Y.; Yang, C.; Agren, H.; Prasad, P. N. *Nano Lett* **2015,** 15, (11), 7400-7407.
13. Zhou, B.; Shi, B.; Jin, D.; Liu, X. *Nat Nanotechnol* **2015,** 10, (11), 924-936.

14. Huang, P.; Zheng, W.; Zhou, S.; Tu, D.; Chen, Z.; Zhu, H.; Li, R.; Ma, E.; Huang, M.; Chen, X. *Angew Chem Int Ed Engl* **2014,** 53, (5), 1252-1257.

15. Bednarkiewicz, A.; Nyk, M.; Samoc, M.; Strek, W. *J Phys Chemy C* **2010,** 114, (41), 17535-17541.

16. Mattsson, L.; Wegner, K. D.; Hildebrandt, N.; Soukka, T. *RSC Adv* **2015,** 5, (18), 13270-13277.

17. Li, Z.; Zhang, Y.; Jiang, S. *Adv Mater* **2008,** 20, (24), 4765-4769.

18. Yan, C.; Dadvand, A.; Rosei, F.; Perepichka, D. F. *J Am Chem Soc* **2010,** 132, (26), 8868-8869.

19. Hong, A. R.; Kim, J.; Kim, S. Y.; Kim, S. I.; Lee, K.; Jang, H. S. *Opt Lett* **2015,** 40, (21), 4959-4962.

20. Marin, R.; Sponchia, G.; Zucchetta, E.; Riello, P.; Enrichi, F.; De Portu, G.; Benedetti, A.; Rohrer, G. *J Am Cer Soc* **2013,** 96, (8), 2628-2635.

21. Nguyen, T. L.; Spizzirri, P.; Wilson, G.; Mulvaney, P. *Chem Commun* **2009**, (2), 174-6.

22. Ganem, J.; Bowman, S. R. *Nanoscale Res Lett* **2013,** 8, (1), 455.

# Chapter 5

## *Green synthesis of highly PEGylated CuS plasmonic nanoparticles*

*The research in the field of non-metallic plasmonic materials has led to the production of high quality chalcogenide PNPs. Specifically, the family of $Cu_{2-x}S$ has proven to possess superior properties in terms of strong NIR light absorption due to a broadband LSPR feature arising from the motion of free holes in the VB. In view of effectively employing $Cu_{2-x}S$ PNPs as theranostic agents, high values of HCE should be achieved, so to make these systems competitive with respect to the noble metal-based ones. Here we present the synthesis of small covellite (CuS) PNPs via a green and rapid method that relies on the use of PEG monomethyl ether (m-PEG) as the growth controlling agent. After the synthesis, the polymer molecules remain attached to the PNP surface imparting colloidal stability to the system. The variation of synthetic parameters such as reaction temperature, pH, sulfur-to-copper ratio, and m-PEG amount leads to different optical, morphological, and structural properties of the PNPs. The evaluation of the HCE efficiency of the sample synthesized with the optimized reaction conditions returned a value of 44.2 %, which makes this system one of the most efficient $Cu_{2-x}S$-based heat converters reported so far. Additionally, the Drude theory was used to model the plasmonic response of these PNPs, obtaining a value of free carrier density of approximately $10^{21}cm^{-3}$, which falls in the range of values reported in literature for $Cu_{2-x}S$ materials.*

## 5.1 Materials and Methods

### 5.1.1 Chemicals

Copper chloride dihydrate ($CuCl_2·2H_2O$, Alfa Aesar, +98 %), polyethylene glycol mono-methyl ether MW 5000 (m-PEG, Aldrich, 99 %), sodium sulfide nonahydrate ($Na_2S·9H_2O$, Aldrich, 98 %), and ethanol (Commercial Alcohols, 100 %) were all used as received without further purification. The working solutions were freshly prepared with de-ionized water and used within one week from their preparation. $Na_2S·9H_2O$ solution was stored at 2-4 °C.

### 5.1.2 Synthesis of CuS PNPs

Copper sulfide PNPs were synthesized via a simple and newly developed one-pot approach. In a typical procedure, 8 mL of a $CuCl_2·2H_2O$ aqueous solution (12.5 mM) were introduced in a 50 mL three necked round bottom flask along with 4 g of m-PEG and a magnetic bar. After the complete dissolution of the polymer under stirring at room temperature, the flask was put in a pre-heated oil bath at 80 °C. After 3 min, 100 µL of a 1 M $Na_2S·9H_2O$ aqueous solution (S/Cu = 1.00) were injected in the reaction mixture. This step was followed by a fast darkening of the solution that eventually becomes dark green. The reaction was allowed to proceed for 5 min. The reaction flask was then quenched in cold water, and the reaction mixture was transferred in a 50 mL centrifuge tube. Then 20 mL of isopropyl alcohol were added and the synthesized PNPs were collected by means of centrifugation (20 min, 6000 *g*). Eventually, the PNPs were re-dispersed in 5 mL of de-ionized water and stored at 4 °C for further characterization.

We investigated the effect of the different reaction parameters on the properties of copper sulfide PNPs. Specifically it was studied the effect of sulfur-to-copper ratio (S/Cu), m-PEG amount, reaction temperature, and pH. Table 5.1 summarizes the different parameters explored throughout this study for the synthesis of CuS PNPs.

### 5.1.3 Characterization techniques

**Optical properties.** The absorption spectra were acquired with a Varian Cary 5000 spectrophotometer using a double beam configuration and 1 cm optical path length quartz cuvettes. A scan speed of 600 nm/min with 1 nm of spectral resolution was used to record the spectra over the 300 – 1100 nm range.

**Table 5.1.** Summary of the synthetic parameter investigated in this work. The parameters whose value has been varied for each series of samples are in bold italic. The sample with gray background is the reference for all the series.

| $Cu^{2+}$, *mmol* | Temperature, *°C* | pH | S/Cu | m-PEG, *g* |
|---|---|---|---|---|
| 0.1 | 80 | 4.6 | ***0.75*** | 4.00 |
| 0.1 | 80 | 4.6 | ***1.00*** | 4.00 |
| 0.1 | 80 | 4.6 | ***2.00*** | 4.00 |
| 0.1 | 80 | 4.6 | ***4.00*** | 4.00 |
| 0.1 | ***40*** | 4.6 | 1.00 | 4.00 |
| 0.1 | ***60*** | 4.6 | 1.00 | 4.00 |
| 0.1 | ***90*** | 4.6 | 1.00 | 4.00 |
| 0.1 | ***100*** | 4.6 | 1.00 | 4.00 |
| 0.1 | 80 | ***2*** | 1.00 | 4.00 |
| 0.1 | 80 | ***3*** | 1.00 | 4.00 |
| 0.1 | 80 | ***6*** | 1.00 | 4.00 |
| 0.1 | 80 | ***8*** | 1.00 | 4.00 |
| 0.1 | 80 | ***10*** | 1.00 | 4.00 |
| 0.1 | 80 | 4.6 | 1.00 | ***0.25*** |
| 0.1 | 80 | 4.6 | 1.00 | ***0.50*** |
| 0.1 | 80 | 4.6 | 1.00 | ***1.00*** |
| 0.1 | 80 | 4.6 | 1.00 | ***2.00*** |
| 0.1 | 80 | 4.6 | 1.00 | ***8.00*** |

**Structure, morphology, and composition.** Copper sulfide PNP crystalline structure was probed by means of XRPD with a Bruker D8 Advance Diffractometer using CuKα monochromatic radiation with a Bragg-Brentano theta-2theta configuration. A scan step of 0.05 ° and 6 s/step of acquisition time was employed, recording the spectra over the 25 – 60 ° range. The morphology of the samples was analyzed using transmission and scanning electron microscopy, respectively using a Philips Tecnai 12 and a Field Emission Gun (FEG) ZEISS microscopes. The surface chemistry of the PNPs was analyzed via FTIR spectroscopy. The spectra were recorded on a ThermoFisher Scientific Nicolet 6700 spectrometer working in transmission mode with a resolution of 1 $cm^{-1}$ over the 4000 – 800 $cm^{-1}$ range. The surface chemistry along with the chemical composition of the PNPs was further investigated by means of XPS. The spectra were recorded on a VG ESCALAB 200i XL instrument, using an Al Kα monochromatic source. The spectra were analyzed using CasaXPS® software.

**Heat conversion efficiency evaluation.** The HCE of a selected sample was evaluated irradiating a PNP aqueous sol contained in a 1x1 cm optical path cuvette with a 980 nm continuous wave (CW) laser (power = 338 mW). The local temperature increase in the cuvette was probed with a digital thermometer (equipped with a type-J thermocouple of 0.5 °C sensitivity). The PNP aqueous sol with an optical density (OD) of 0.71 at the laser wavelength (980 nm) was kept under continuous magnetic stirring during the experiment. In Figure 5.1 a scheme is reported representing the set-up used for the HCE evaluation.

## 5.2 Results and discussion

In order to identify the optimal synthetic conditions for the preparation of colloidally stable, monodisperse, and single-phase CuS PNPs, the results obtained from the optical and the structural/morphological studies were compared.

### 5.2.1 Effect of the S/Cu ratio

The parameter that experimentally has the greater effect on the PNP features is the S/Cu ratio. As discussed in Section 1.4.2, copper sulfide can crystallize in an extraordinary large number of polymorphs whose stoichiometry varies between the two extreme compounds CuS and $Cu_2S$. Among them, the more copper-deficient compounds are those displaying stronger LSPR absorption features. For this reason, it was decided to investigate the effect of S/Cu values 0.75, 1.00, 2.00, and 4.00. The use of a S/Cu ratio of 0.75 instead of the stoichiometric sulfur amount (1.00) has the sole consequence of the production of a lesser amount of PNPs, maintaining the same crystalline structure. To support this observation, the absorption spectra of these two samples have the same profile and differ just in their absolute absorbance values (Figure 5.2).

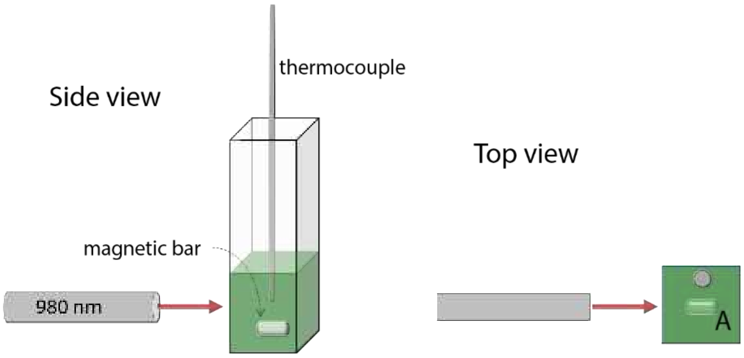

**Figure 5.1.** Scheme of the experimental setup used for the evaluation of the HCE of CuS PNPs. In the "top view" with A it is indicated the surface area through which the heat exchange with the environment takes place.

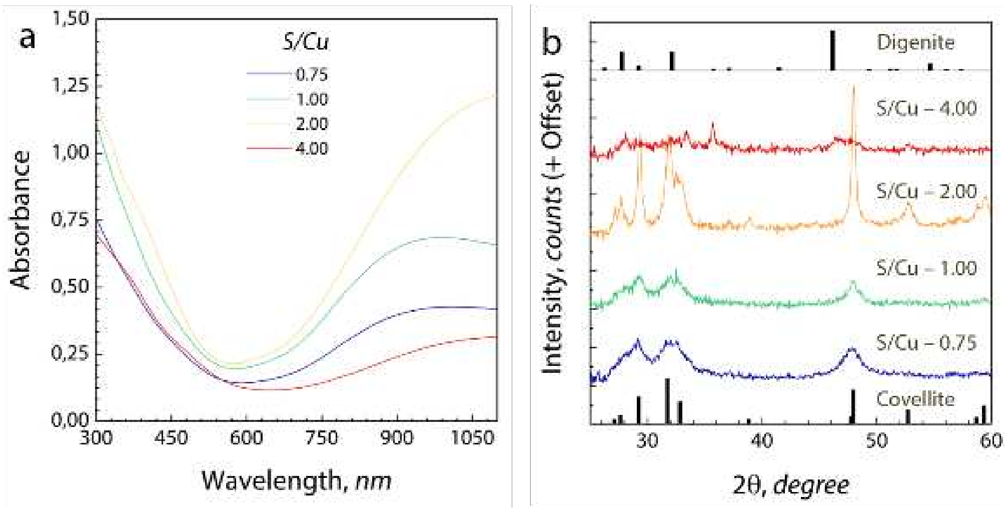

**Figure 5.2.** Absorbance spectra (*a*) and diffractograms (*b*) of PNPs synthesized varying the S/Cu ratio. Both the plasmonic band (position and intensity) and the crystallinity of the sample are greatly influenced by this parameter. An excess of $S^{2-}$ ions determines the production of poorly stable PNPs, while an under-stoichiometric amount does not allow for a complete consumption of the $Cu^{2+}$ in solution, thus leading to a low yield of the reaction.

Indeed, the diffraction patterns of these two samples are identical and the position of the reflections well matches with the position of the reflections of covellite (CuS, PDF #01-078-2121). This compound has chemical composition CuS, copper being most likely in its singly oxidized valence[1]. An increase of the S/Cu ratio to 2.00 determines an improvement of the plasmonic properties of the sample, with the LSPR band becoming more intense if compared to the band gap associated absorption at shorter wavelengths. The diffractogram of this sample shows narrower reflections with respect to those of the other samples, still falling in correspondence to the covellite peaks. This is an indication of larger crystallites and SEM observations allowed to confirm this hypothesis (Figure 5.3). Indeed, the sample is composed of PNPs having different size and morphology, the majority being large platelets having diameters varying considerably form particle to particle. According to the literature, large $Cu_{2-x}S$ nanoplatelets have better plasmonic properties than smaller spherical PNPs[2], an observation in accordance with the results we obtained from the optical analysis. When the sulfur amount was increased to a S/Cu value of 4.00, the LSPR band dramatically dropped in absolute intensity. The crystallinity of the sample is compromised and at least one secondary phase appears, which was tentatively assigned to digenite ($Cu_9S_5$, PDF #00-047-1748). Moreover, the stability of the sample is compromised and the PNPs clump, precipitating few hours after the synthesis.

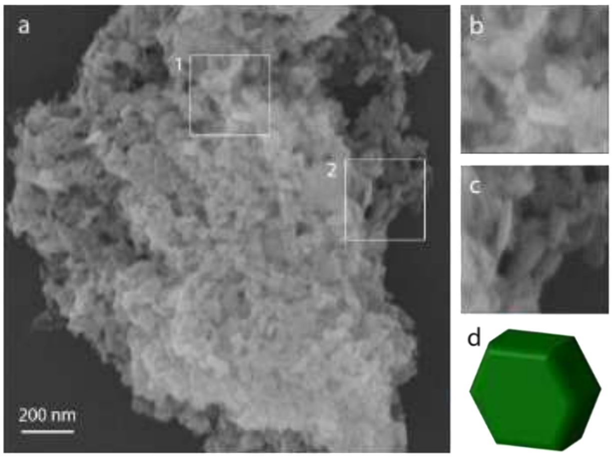

**Figure 5.3.** SEM observations of the sample synthesized with S/Cu=2.00 (*a*, with *b* and *c* being respectively zooms of square 1 and 2) show that the PNPs have different morphology and size, ranging from small quasi-spherical to larger platelets (*d*).

According to these observations, we selected the S/Cu ratio of 1.00 as the best compromise between good plasmonic properties and structural and morphological homogeneity.

### 5.2.2 Effect of the temperature

The temperature at which the reaction takes place influences the LSPR band position (Figure 5.4). In the inset of Figure 5.4a we can observe that there is a linear dependence between the peak position and the reaction temperature, with the LSPR band wavelength varying in the range 950 – 1050 nm. To interpret this behavior we considered the mechanisms responsible for the LSPR. All the samples of this series have a pure covellite phase, whose stoichiometry is fixed with Cu-to-S ratio of 1:1. Deviation from this ratio would result in a change of the crystalline structure[3]. The chemical composition of the material is also confirmed by the XPS analysis that returns a constant composition of the four samples, with a Cu-to-S ratio of respectively 0.95, 1.02, 1.05, 1.03 for the samples synthesized at 40, 60, 80, 100 °C (Figure 5.5 and Table 5.2). The survey spectra of the samples show the characteristic peaks of the species composing the PNPs. In all the samples, the Cu 2p high-resolution spectrum shows the presence of copper in its singly oxidized state as confirmed by the position of Cu LMM peak. The weak satellite peak centered approximately at 942.5 eV in all the samples suggests the presence of negligible traces of $Cu^{2+}$. S 2p peak can be fitted with two doublets corresponding respectively to metal sulfide (green lines) and partially oxidized sulfide species (light blue lines).

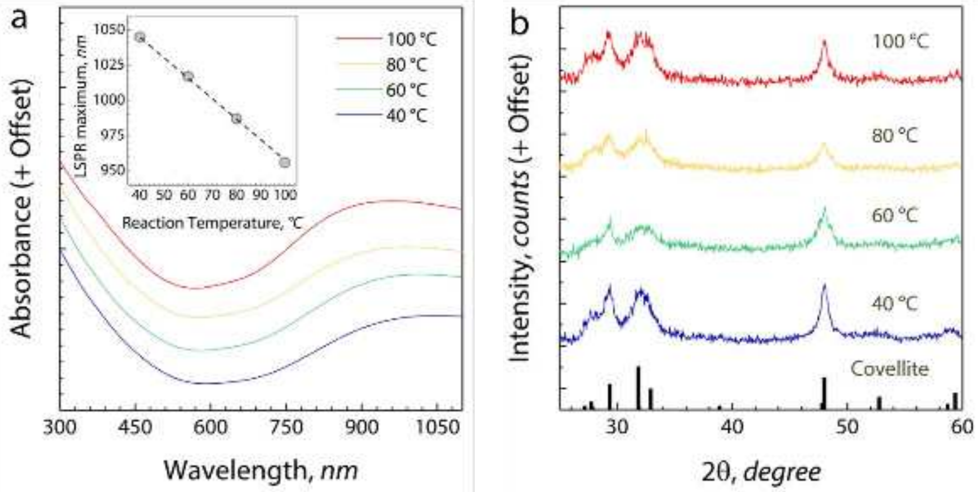

**Figure 5.4.** The reaction temperature increase does not change the shape of the LSPR peak (*a*) but determines a blue-shift of the peak maximum (inset in a). Temperature does not influence the NP crystal structure, and all the samples crystallize in the covellite polymorph (*b*).

The considerable contribution from these latter species can be justified by the fact that the reaction is conducted in water and in air atmosphere, so that surface oxidation becomes a likely event. Following these considerations, the hypothesis that compositional variations from sample to sample influence the optical behavior of the synthesized PNPs can be ruled out. Another parameter influencing the plasmonic properties of $Cu_{2-x}S$, and in particular the LSPR peak position, is the dielectric constant of the medium in which the NPs are embedded[4]. In this study the measurements were all performed in de-ionized water and the same polymer (m-PEG) covers the surface of the samples so that we can consider the local dielectric constant at the PNP/water interface to be equal in all the samples.

**Table 5.2.** Summary of the results obtained from the analysis of the XPS spectra.

| Reaction temperature, °*C* | Cu 2p peak position, *eV* | Cu LMM peak position, *eV* | S 2p peak position, *eV* (relative percentage) | Cu-to-S ratio |
|---|---|---|---|---|
| 40 | 932.63 | 568.93 | 162.03 (64.8 %) – 163.63 (36.2 %) | 0.95 |
| 60 | 932.30 | 569.00 | 162.00 (76.2 %) – 163.60 (23.8 %) | 1.02 |
| 80 | 932.23 | 568.73 | 161.83 (83.8 %) – 163.63 (16.2 %) | 1.05 |
| 100 | 932.20 | 568.56 | 161.96 (80.2 %) – 163.66 (19.8 %) | 1.03 |

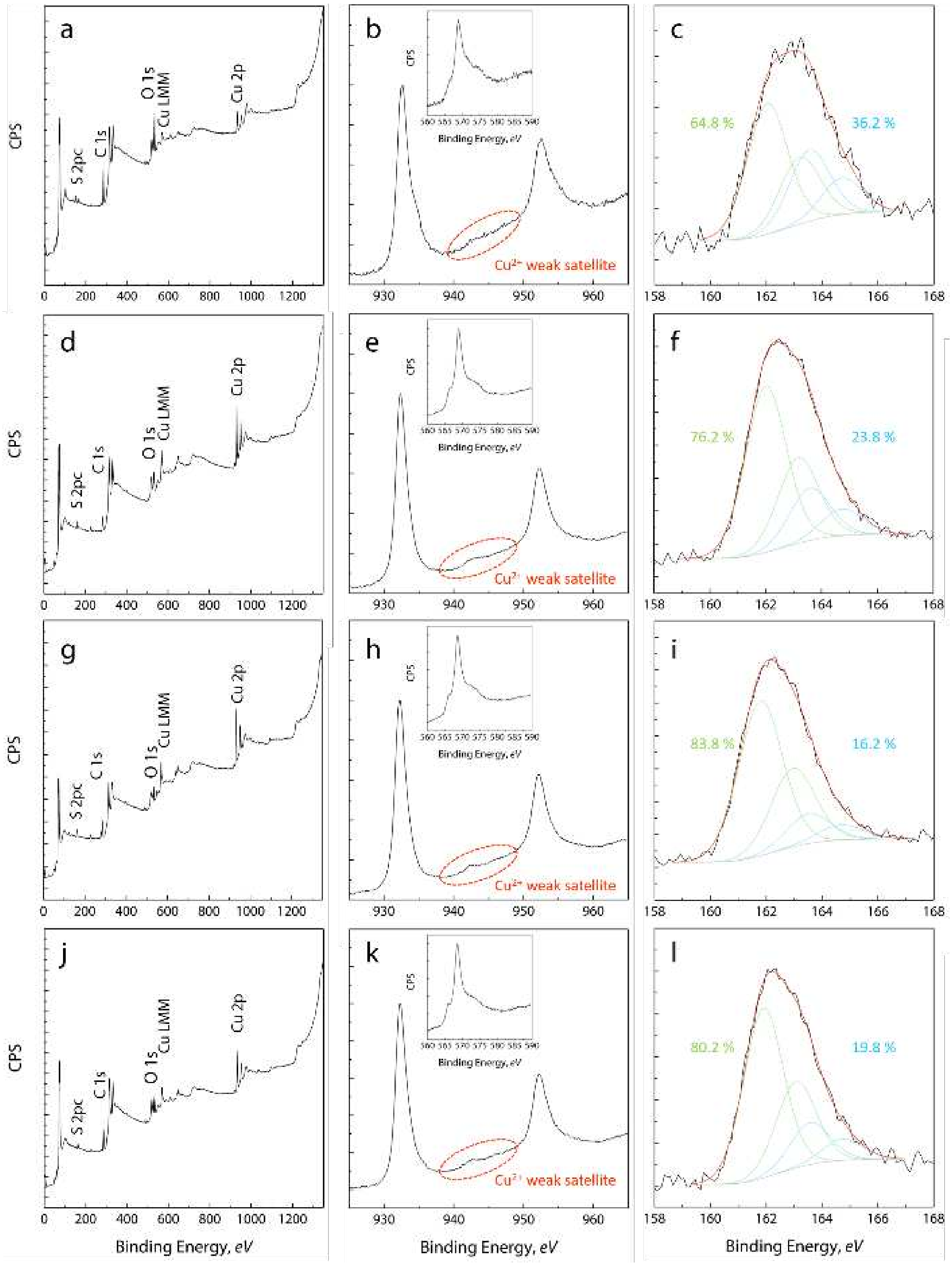

**Figure 5.5.** Survey (*a, d, g, j*), and Cu 2p (*b, e, h, k*), Cu LMM (insets in *b, e, h, k*), S 2p (*c, f, I, l*) high resolution spectra of the samples synthesized at 40, 60, 80, and 100 °C. In *b, e, h, k* the signal characteristic of $Cu^{2+}$ is highlighted in red. In *c* the relative percentage of sulfide and oxidized sulfide species are reported (light green and light blue respectively).

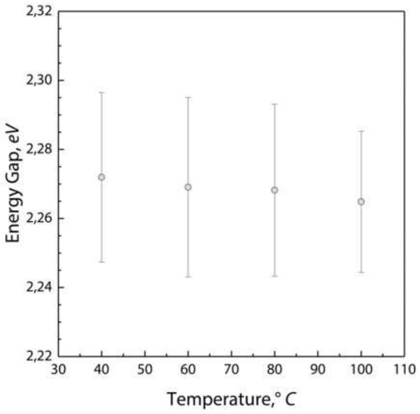

**Figure 5.6.** The determination of the energy gap using the Tauc approach returns a constant value. This result is in accordance with the observation that in $Cu_{2-x}S$ PNPs this parameter is mainly determined by the number of holes in the VB, *i.e.* the stoichiometry of the material, which is the same for all of the samples analyzed.

The last parameter that can influence the LSPR peak position is the morphology of the PNPs, *i.e.* their size. Larger PNPs have a LSPR peak blue-shifted with respect to smaller PNPs as reported from Luther et al.[5].. One can estimate in an indirect way the size of a nano-sized semiconductors using the energy gap value, obtained from the absorption spectrum, in the effective mass approximation equation[6]. To do so, we used the Tauc approach[7] on the short-wavelength side of the absorption spectra, where the interband transition dominates.

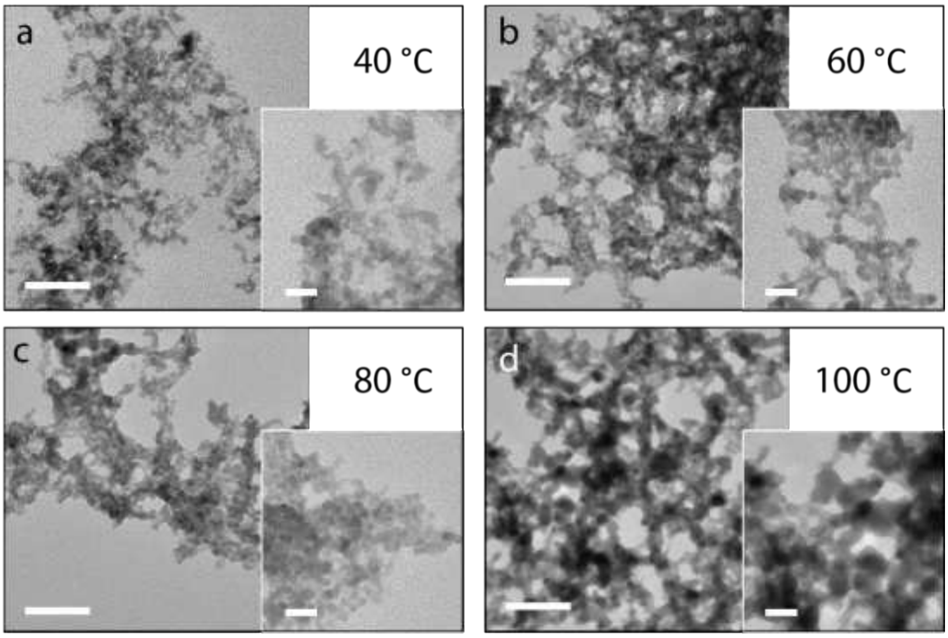

**Figure 5.7.** TEM micrographs of PNPs synthesized at 40, 60, 80, and 100 °C (a, b, c, and d) show small particles of increasing size. At 60 and 80 °C the PNPs have a more regular quasi-spherical shape. The larger scale bars are 50 nm and the smaller are 20 nm.

Nonetheless, the energy gap value in this type of degenerate semiconductors is mainly dominated by the presence of empty levels in the top of the VB, *i.e.* by the free carrier density[1]. This explains the results obtained from the Tauc approach: the values are very close one to another, corroborating the hypothesis of PNPs having the same chemical composition (Figure 5.6). The slight decrease of the energy gap values with increasing temperature could account for the growth of larger PNPs, but the error associated to each point makes this change irrelevant. An evidence of the different size of the PNPs comes from the TEM observations (Figure 5.7). Increasing the reaction temperature, the size of PNPs increases accordingly, with the samples synthesized at 60 and 80 °C displaying a clear quasi-spherical morphology. In spite of the visible size increase, the irregular shape of the samples complicates the determination of the size distribution for all of them. Easier is the case of CuS PNPs synthesized at 80 °C, for which a size of approximately 7.2 ± 0.7 nm was estimated.

### 5.2.3 Effect of the pH

As in all aqueous synthetic approaches, the pH of the reaction mixture plays a key role in controlling the properties of the final material. In the case under study, the pH of the aqueous solution in the presence of copper and m-PEG is 4.6. The pH of the reaction mixture was adjusted using 1 M solutions of NaOH and HCl. The absorption features of the PNPs are not influenced much when the pH is lowered below 4.6 (Figure 5.8a).

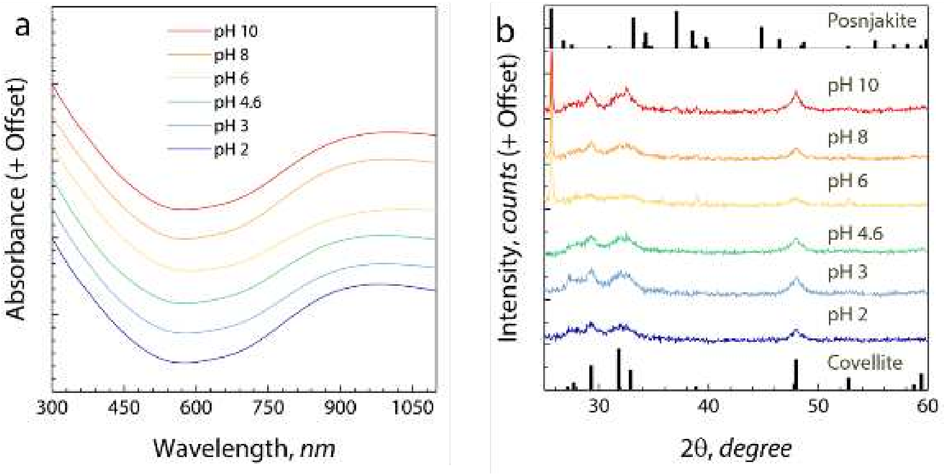

**Figure 5.8.** The change of the reaction mixture pH does not influence the LSPR band intensity and position at acidic pH (*a*), as confirmed also from the presence of a covellite single phase in these PNPs (*b*). Instead at higher pH a secondary phase appears (posnjakite) characterized by large crystallites, as confirmed by the sharp reflections in the diffraction patterns.

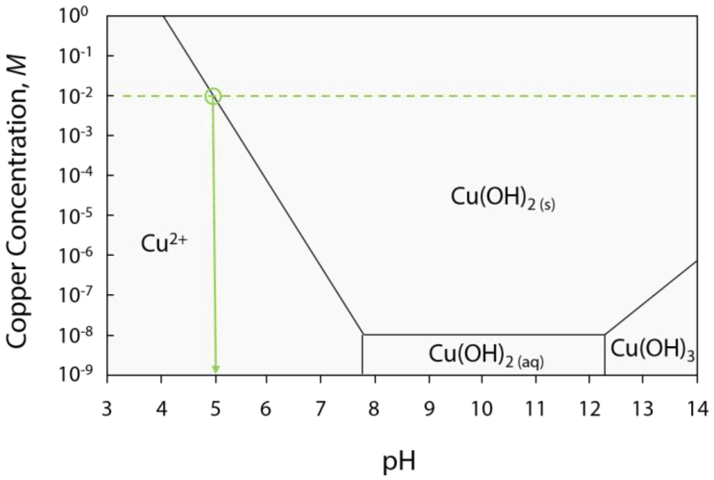

**Figure 5.9.** Stability diagram of copper. The green dashed line is drawn in correspondence of the $Cu^{2+}$ concentration used in the study. At this concentration the pH at which $Cu(OH)_2$ starts becoming the stable phase is approximately 5. Adapted from Ref. [8].

This is in accordance with the XRPD observations that reveal a covellite single phase at a pH between 2 and 4.6 (Figure 5.8b). At higher pH a secondary phase appears, namely posnjakite (PDF #01-075-1258). This compound is a hydroxy-sulfate hydrate with formula $Cu_4(SO_4)(OH)_6 \cdot H_2O$. The appearance of this $Cu^{2+}$ compound is justified at the light of the stability diagram of hydrated copper species in aqueous environment (Figure 5.9)[8]. At the copper concentration we performed the synthesis (approximately $10^{-2}$ M), copper is present as a free ion below a pH value of 5, while at more alkaline conditions copper hydroxide $Cu(OH)_2$ starts becoming the stable phase. For this reason, part of the sample is composed of posnjakite, a hydroxy-sulfate. The presence of this secondary phase is not desirable, since it crystallizes in large crystals, as can be concluded from the narrow peaks in the corresponding diffractograms. For this reason, although the optical properties are still preserved from the samples synthesized at high pH values, these samples could not be considered suitable good quality heat converters.

### 5.2.4 Effect of m-PEG amount

The amount of m-PEG introduced in the reaction environment was varied to investigate the effect of this molecule as a ligand in controlling the growth of the PNPs. The hydroxyl tail group and the oxygen atoms in the backbone of the molecules can all act as effective Lewis bases (electron lone-pair donors) to stabilize free copper ions in solution.

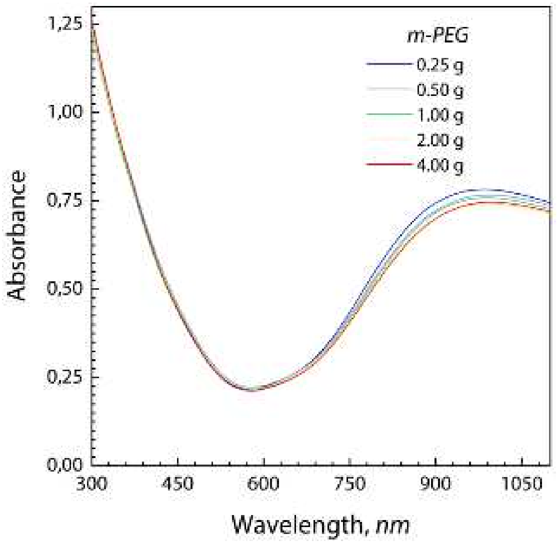

**Figure 5.10.** At the tested conditions, the amount of m-PEG introduced in the reaction environment has little effect on the synthesized PNPs. This insensitiveness of the PNP final properties upon the variation of the m-PEG concentration stems from the presence of a large excess of coordinating atoms (oxygen) with respect to the metal ions.

This is true, even though the affinity of copper towards oxygen is low, if compared for instance with the one displayed from the transition metal towards thiol groups. It was observed that this parameter plays a minor role in the synthesis at the tested conditions. Actually, even when a sub-stoichiometric amount of m-PEG (0.25 g, 0.05 mmol) is present in the reaction environment with respect to $Cu^{2+}$ (0.10 mmol), the number of oxygen atoms is in large excess with respect to the metal ions (each polymer chain counts approximately 110 $-CH_2-CH_2-O-$ repeating unities). Indeed, the variation of m-PEG amount does not influence the optical properties of the synthesized PNPs: both intensity and profile shape are substantially identical in all samples (Figure 5.10).

After the thorough characterization of the various samples, the PNPs synthesized at 80 °C, with a S/Cu=1.00, pH 4.6, and in the presence of a m-PEG amount of 4.00 g were selected for further studies. This choice was dictated by the achieved optimization between structural, morphological, and optical properties. Moreover, the maximum LSPR band position of this sample is very close to the wavelength of laser chosen for the study of HCE (*i.e.* 980 nm).

### 5.2.5 Surface chemistry

To confirm the presence of m-PEG molecules on the surface of the CuS NPs, other than conventional method such as FTIR (Figure 5.11), a particular SEM observation technique was also applied[9].

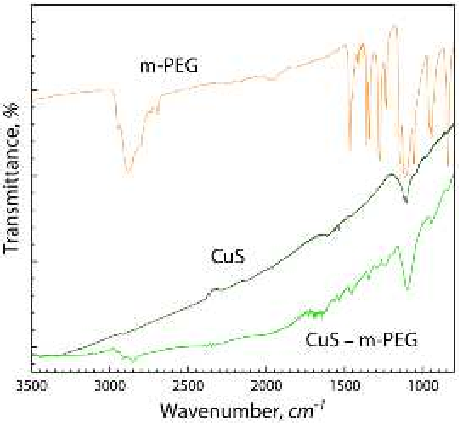

**Figure 5.11.** The presence of m-PEG on the surface of CuS PNPs is confirmed comparing the FTIR spectra of PNPs synthesized in the presence (CuS – m-PEG) and in the absence (CuS) of m-PEG. In the spectrum of the former the distinctive stretches of m-PEG (orange spectrum) are present.

A batch of CuS PNPs was synthesized following the same approach followed for the other samples, without the addition of m-PEG. This samples was used to compare the surface features of pegylated CuS PNPs. We imaged the sample (thoroughly washed three times with a mixture of water:ethanol 1:1) at decreasing electron accelerating voltage, *i.e.* decreasing electron kinetic energy. In our system, the lower the kinetic energy of the electron (in Figure 5.12 following the order: a – 20 kV, b – 10 kV, c – 5 kV, d – 2.5 kV, e – 1.25 kV) the more superficial is the generation of the so-called pear of interaction between the electron and the material.

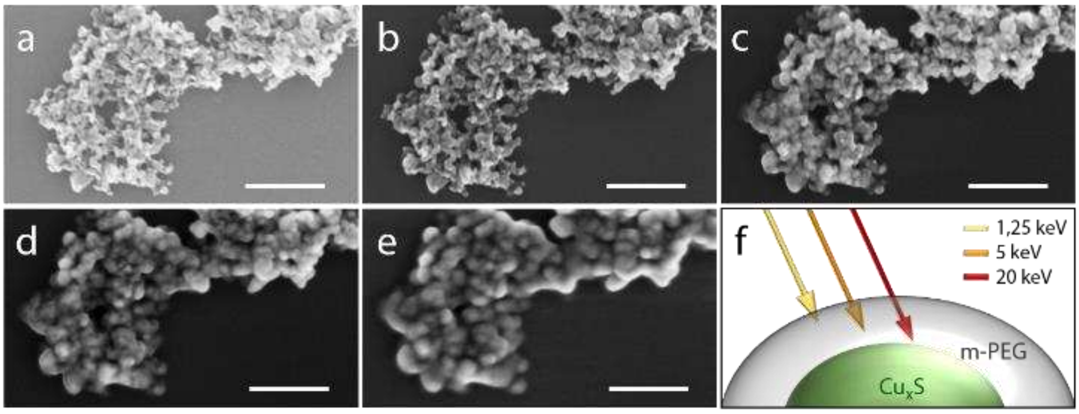

**Figure 5.12.** SEM observations of the reference sample show the presence of a consistent layer of polymer (namely m-PEG) coating the NPs. We were able to image the polymer gradually decreasing the accelerating voltage applied to the electron (*a* – 20 kV, *b* – 10 kV, *c* – 5 kV, *d* – 2.5 kV, *e* – 1.25 kV), *i.e.* decreasing their kinetic energy. In *f* a scheme is reported showing how different electron energies allow to probe the polymeric layer at different depths. Scale bars in the figures corresponds to 200 nm.

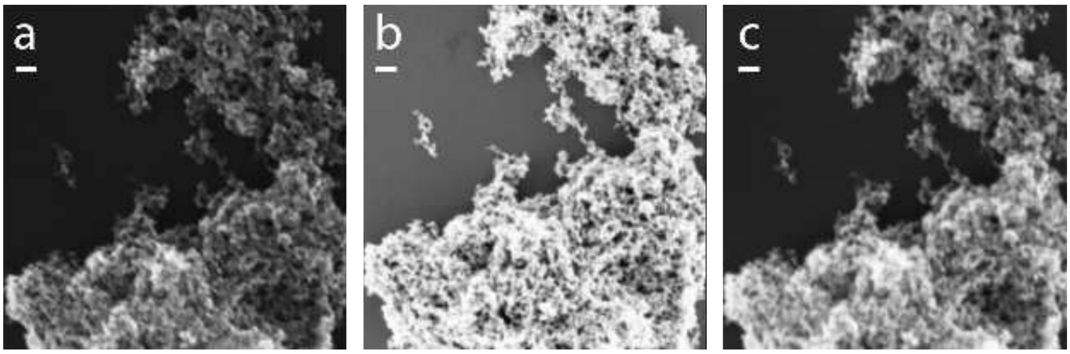

**Figure 5.13.** SEM observations of a sample synthesized in the absence of m-PEG do not show the same behavior under the electron beam at different accelerating voltages (respectively a – 10 kV, b – 5 kV, c – 1.25 kV). This confirms that the different signal observed at low voltages in the samples synthesized with m-PEG stems from the polymeric chains on the PNP surface. Scale bars in the figures corresponds to 200 nm.

At high voltage (20 – 10 kV) the signal generates at the NP surface, while at lower voltage the signal is collected progressively from layers of polymer which are more distant from the core of the NP (Figure 5 f). From the micrographs it is clearly observable the presence of the layer of polymer coating the NPs. We could not observe the same effect in a sample synthesized in the absence of m-PEG (see Figure 5.13).

### 5.2.6 Heat conversion evaluation

The sought property for the PNPs synthesized in this study is the capability of translating NIR light into heat according to the photothermal effect (Section 1.3.2.). The figure of merit that quantitatively account for this capability is the HCE. This value can be evaluated using the experimental approach presented in Scheme 1.1. The HCE value is obtained according to the equation:

$$\eta = \frac{hA(T_{max} - T_0) - Q_0}{I(1 - 10^{-OD})} \tag{5.1}$$

where $h$ is the heat-transfer coefficient, $A$ is the surface area of the liquid where the heat exchange with the environment takes place (*i.e.* the area of the cuvette section), $T_{max}$-$T_0$ ($\Delta T$) is the temperature increase realized in the cuvette during the irradiation with light, $Q_0$ is the heat exchanged by the medium (water in this case) in the same experimental conditions but in the absence of nano-heaters, $I$ is the laser intensity, and $OD$ is the optical density of the solution at the excitation wavelength ($\lambda_{ex}$)[10].

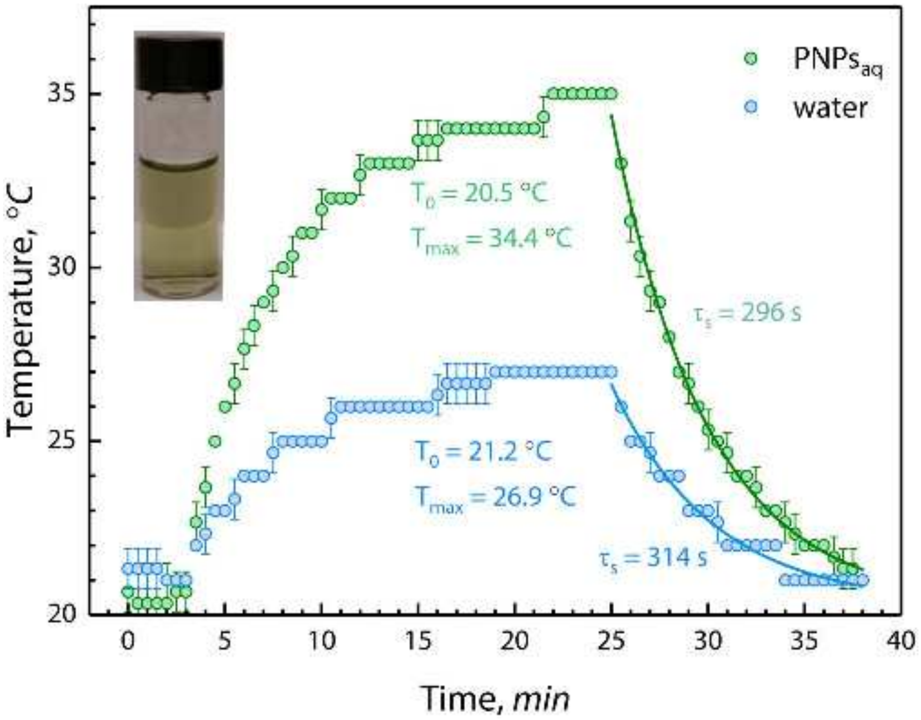

**Figure 5.14.** Temperature *vs.* time plot for PNPs and water alone, obtained under 980 nm CW laser irradiation. Dots are experimental points (the error bars are obtained repeating the measurement three times) and the solid lines in the cooling part of the curve are the exponential fit. In the inset, we report a picture of the sol used to determine the HCE of the PNPs.

$h$ and $Q_0$ are derived from the time constant ($\tau_S$) as obtained from the fit of the cooling part of the curves (starting at 25 min) using a single exponential function The thorough explanation of the mathematical approach used in this context is accurately described in Ref.[10]. The results of the experiment are reported in Figure 5.14, where a temperature increase of approximately 14 °C is observable in the PNP sol under laser illumination. Using the experimental values reported in Table 5.3, an HCE of 44.2 % was estimated. It can be observed that this value is lower than most of the best performing Au-based systems (Table 1.1). Nonetheless, it is worth noting that our CuS PNPs compete with the state-of-the-art $Cu_{2-x}S$ photothermal agents, being among the most efficient reported in the literature.

**Table 5.3.** Values of the experimental parameters used in the evaluation of the HCE of CuS PNPs sol.

| $\lambda_{ex}$, *nm* | I, *mW* | OD | A, *cm²* | Solvent mass, *g* |
|---|---|---|---|---|
| 980 | 338 | 0.71 | 1 | 1 |

### 5.2.7 Free carrier density estimation and solvent effect

An important parameter governing the heat conversion capability of a plasmonic material is the density of free carriers[1]. In Section 1.3.1 it was already described more in details the model proposed by Drude and how it can be used to interpret the behavior of PNPs, so here we will refer to those equations. In the particular case of $Cu_{2-x}S$ PNPs the plasma frequency is a function of the free holes density $N_h$, since the plasmonic properties of these PNPs arise from the free hole motion.

$$\omega_p^2 = \frac{N_h e^2}{\varepsilon_0 m^*} \tag{5.2}$$

Imposing the Fröhlich condition (Equation 1.6) and considering the relation for the plasmon resonance given in Equation 5.2 we obtain the:

$$\omega_{LSPR}(N_h, \varepsilon_m) = \sqrt{\frac{N_h e^2}{\varepsilon_0 m^*(2\varepsilon_m + \varepsilon_\infty)} - \gamma^2} \tag{5.3}$$

Indeed, $N_h$ and $\varepsilon_m$ are the two parameters that influence the most the plasmonic properties of the material. Here, our attention is focused on the estimation of $N_h$ starting from the experimental parameters, since this value is a critical feature for the heat conversion capability of the material. The experimental parameters that are used in the rest of the calculations are respectively $\varepsilon_\infty = 9^2$ and $m^* = 0.8$ times the rest mass of the electron[11]. The value of $\gamma$ in PNPs is experimentally obtained from the linewidth of the LSPR band[5]. In our case, it was estimated to be 0.8 eV as from the absorption spectrum (Figure 5.15a). A fresh batch of PNPs were synthesized and the absorption spectrum of the sample dispersed in different solvents was recorded. The chosen solvents are water ($H_2O$), *N,N*-dimethylformamide (DMF), and dimethylsuphoxide (DMSO). Notably, the LSPR peak shifts towards lower energy when the refractive index of the solvent decreases (Figure 5.15a and inset). This behavior is in accordance with the observation made by P. Alivisatos on tungsten oxide PNPs[12]. In particular, it was observed that the shift is less than 60 meV between the sample dispersed in water and the one dispersed in DMSO.

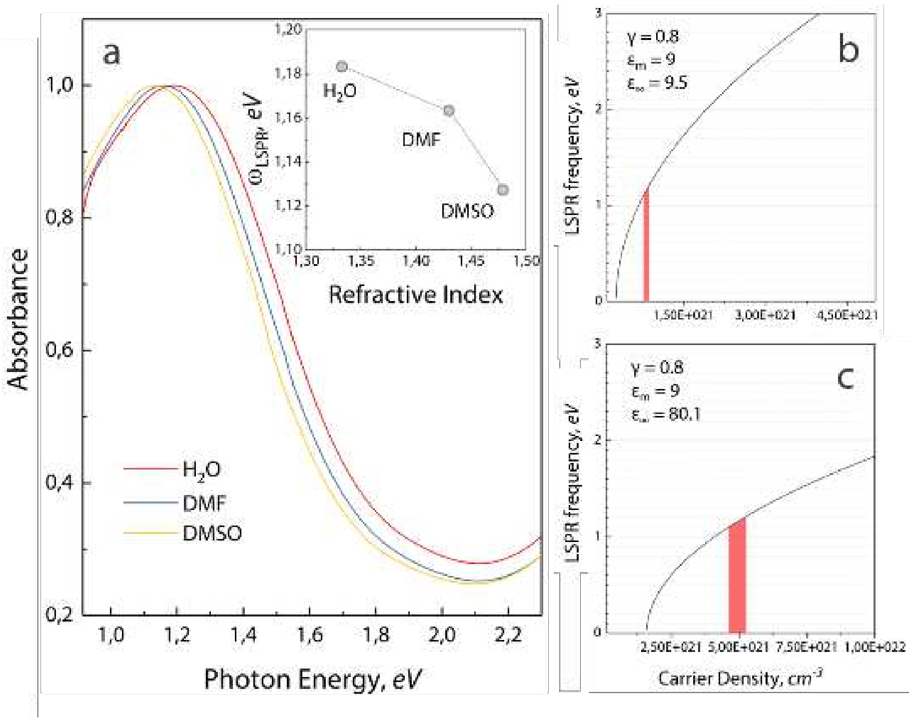

**Figure 5.15.** Dispersions of CuS NPs in different solvents ($H_2O$, DMF, and DMSO) with increasingly higher refractive index determines a shift of the LSPR peak at lower energy (Figure *a* and inset). The use of different dielectric constant to model the behavior of the material, affects the final results. This can be observed in *b* and *c*, where respectively the dielectric constant values of 9.5 (estimated for m-PEG) and 80.1 ($H_2O$) were used to obtain an indication of the density of free carriers. The red rectangles are used to account for the uncertainty on the plasmon frequency determination (experimentally observed to fall between 1.12 – 1.18 eV).

To estimate the free carrier density in the PNPs the dielectric permittivity of the three solvents was used together with the position of the LSPR peak displayed by each sol (Table 5.4). It is to be mentioned that our PNPs are rather small and they are covered with a high molecular weight polymer (m-PEG 5000). For this reason, the PNPs should see a dielectric permittivity which is not the one of the solvent itself, but rather an effective dielectric permittivity $\varepsilon_{eff} < \varepsilon_m$. This value is expected to be lower than the one of the medium in which the PNPs are dispersed, due to the effect of the thick polymeric (m-PEG) layer coating the PNPs. To obtain this value, the data obtained for high molecular weight PEG[13] was extrapolated at low temperature, choosing a value of 9.5. The use of this value returns a free carrier density $N_h = 0.82 \cdot 10^{21}$ $cm^{-3}$ (see Figure 5.15b and 5.15c for a visual representation of the effect of the medium dielectric permittivity on the LSPR peak position). This value of dielectric permittivity also allows to obtain a more reasonable value for the plasmon frequency, if compared with the values calculated using the dielectric constant of the solvents.

**Table 5.4**. Free carrier density and plasmon frequency values obtained using the dielectric permittivity of the three solvents used to disperse the PNPs ($H_2O$, DMSO, DMF) and the one of m-PEG 5000. The dielectric permittivity used for m-PEG is obtained from the extrapolation to low temperature of the data reported in Ref.[13].

| **Solvent** | $\varepsilon_m$ | $N_h$, *cm*$^{-3}$ | $\omega_p$, *eV* |
|---|---|---|---|
| $H_2O$ | 80.1 | $5.1 \cdot 10^{21}$ | 18.6 |
| DMSO | 46.7 | $2.4 \cdot 10^{21}$ | 12.8 |
| DMF | 36.7 | $2.9 \cdot 10^{21}$ | 14.0 |
| m-PEG | 9.5* | $0.8 \cdot 10^{21}$ | 7.4 |

The same calculations were repeated using different values of $\gamma$ (0.7 and 0.9 eV) observing that the results are not much influenced by variations of this parameter. To conclude, it has to be reminded that the calculations that were performed are estimations. For instance, the actual dielectric permittivity that the PNPs are experiencing should fall somewhere in between the $\varepsilon$ of the solvent and the one of the polymer. Given the uncertainty associated with these parameters, it is possible to affirm that the a free carrier density of in our PNPs is approximately $10^{21}$ cm$^{-3}$, a value that falls in the range of those reported in the literature (from $10^{20}$ to $10^{22}$ cm$^{-3}$)[2, 5, 11].

## 5.3 Conclusions

In this study we have reported an easy, reproducible, and green synthesis of highly pegylated CuS PNPs. We studied the effect of different reaction parameters on the optical, structural, and morphological features of the final reaction product, observing that the sulfur-to-copper (S/Cu) ratio plays a major role in controlling the properties of the PNPs and their morphology. Variations of reaction temperature allows for the tuning of LSPR peak position, while the pH influences the phase purity of the sample. Carefully selecting the reaction conditions, it was possible to synthesize single-phase covellite CuS PNPs with a chemical composition Cu:S=1:1, as confirmed from XPS measurements. These NPs are small, with a mean size of 7.3 ± 1.4 nm. The presence of m-PEG on the surface of the PNPs was ascertained, other than directly observing the colloidal stability of the PNP aqueous suspension, using conventional FTIR analysis and a particular SEM observation technique. In particular, this last technique relies on the variation of the accelerating voltage to probe different parts of the sample. Eventually, the sample displaying the best properties was selected and its HCE was evaluated irradiating an aqueous sol of these PNPs with a 980 nm CW laser. The observed HCE value of 44.2 % is among the highest reported in the literature for copper $Cu_{2-x}S$ systems. Moreover, it is to be highlighted that our PNPs are synthesized directly in water following a green approach that does not require a surface modification step in order to be make the PNPs water-dispersible. To conclude, the properties of these PNPs makes them ideal candidates as photothermal agents to be readily used in aqueous/biological environments.

## References

1. Comin, A.; Manna, L. *Chem Soc Rev*, **2014**, 43, (11), 3957-3975.
2. Kim, M. R.; Hafez, H. A.; Chai, X.; Besteiro, L. V.; Tan, L.; Ozaki, T.; Govorov, A. O.; Izquierdo, R.; Ma, D. *Nanoscale*, **2016**, 8, (26), 12946-12957.
3. Goble, R. J. *Can Mineral*, **1985**, 23, 61-76.
4. Khlebtsov, N. G.; Dykman, L. A. *J Quant Spectrosc Radiat Transfer*, **2010**, 111, (1), 1-35.
5. Luther, J. M.; Jain, P. K.; Ewers, T.; Alivisatos, A. P. *Nat Mater*, **2011**, 10, (5), 361-366.
6. Nishiguchi, N.; Yoh, K. *Jpn J Appl Phys*, **1997**, 36, (6S), 3928.
7. Wherrett, B. S. *Optica Acta: International Journal of Optics*, **1973**, 20, (3), 250-250.
8. Albrecht, T. W.; Addai-Mensah, J. J.; Fornasiero, D. presented in part at the Chemeca 2011: Engineering a Better World, Sydney Hilton Hotel, NSW, Australia, 18-21 September 2011, 2011.
9. Hlawacek, G.; Ahmad, I.; Smithers, M. A.; Kooij, E. S. *Ultramicroscopy*, **2013**, 135, 89-94.
10. Roper, D. K.; Ahn, W.; Hoepfner, M. *J Phys Chem C Nanomater Interfaces*, **2007**, 111, (9), 3636-3641.
11. Xie, Y.; Carbone, L.; Nobile, C.; Grillo, V.; D'Agostino, S.; Della Sala, F.; Giannini, C.; Altamura, D.; Oelsner, C.; Kryschi, C.; Cozzoli, P. D. *ACS Nano*, **2013**, 7, (8), 7352-7369.
12. Manthiram, K.; Alivisatos, A. P. *J Am Chem Soc*, **2012**, 134, (9), 3995-3998.
13. Koizumi, N.; Hanai, T. *Bulletin of the Institute for Chemical Research*, **1964**, 42, 115-127.

# Chapter 6

## *Summary and future work*

In this thesis I have presented the study of two classes of semiconductor materials with great potential from an applicative viewpoint: copper indium sulfide (CIS) quantum dots (QDs) and copper sulfide ($Cu_{2-x}S$) plasmonic nanoparticles (PNPs).

With regard to CIS QDs, my research has led to the establishment of an innovative synthetic protocol that allows for the synthesis of QDs readily dispersible in polar organic solvents. This feature stems from the use of 3-mercaptopropyl trimethoxysilane (MPTS) as sulfur source and growth controlling species in the reaction environment. These molecules remain bound on the QD surface giving rise to a complex structure, where the thiol groups govern the interaction with the solvent in which the QDs are dispersed. Moreover, the careful analysis of the optical properties of these QDs allowed to observe a growth mechanism characterized by the presence of nanoparticles of discrete size: a behavior never reported in the literature before.

In the same research framework, I have investigated the effect that the presence of halogen anions has on the growth and the final properties of CIS QDs prepared following a well-established thermal decomposition synthetic method. This study was conducted in the attempt of rationalizing the role played by the reaction parameters in the synthesis of these nanoparticles. The QDs were prepared in 1-octadecende and 1-dodecanethiol using three different halogenide copper (I) salts (CuI, CuBr, CuCl) and their optical, structural, and morphological features were thoroughly investigated. The results of this study show that the polarizability of the halogen ion has a major role in controlling the growth of the QDs and the tunability of their optical properties. Specifically, the trend displayed by the QD properties (such as photoluminescence quantum yield and anion incorporation in the crystalline lattice) follows that of the anion polarizability, according to the order described by the Hofmeister series. This observation allowed for the postulation of a modulation of the growth kinetic from the different interaction of the anions with the hydrophobic tails of the metal thiolate precursors.

Thanks to the experience gained in the synthesis of CIS QDs, I moved to the investigation of the interaction of these systems with rare earth (RE)-doped upconverting nanoparticles (UCNPs). In particular, the energy transfer that takes place from UCNPs to CIS QDs following the photoexcitation of UCNPs was thoroughly analyzed. This study aimed for the observation of evidence of Förster energy resonance energy transfer (FRET) between the two aforementioned species. This interest is justified in light of the great appeal that this phenomenon has in view of the development of optical probes for bio-assays. For this purpose $LiYF_4$:Yb,Tm UCNPs were synthesized having core-only or core/shell architecture and their interaction with copper-deficient CIS QDs was tested both in sol or in powder form. The results of this characterization show that a random motion of the nanoparticles in suspension does not allow for a sufficient proximity of the moieties (energy donors and acceptors) in order to observe appreciable FRET. Instead, when UCNPs and QDs are dried on a solid support, an appreciable decrease of the UCNP luminescence lifetime can be observed, which is known to be an undisputed evidence of FRET. These preliminary observations allowed identifying the presence of a large fraction of superficial $Tm^{3+}$ ions (*i.e.* lying in the first few nanometers of UCNP surface) as a pivotal requisite to be satisfied in order to have appreciable FRET to QDs. According to these observations, more UCNPs have been synthesized where the fraction of superficial $Tm^{3+}$ ions has been increased: the use of these UCNPs is expected to lead to an even more pronounced FRET to nearby QDs.

Eventually, considering copper sulfide PNPs, a novel green synthetic method has been developed. In particular, I exploited the weak coordinating capabilities of a high molecular weight polyethylene glycol (PEG) to control the growth and impart colloidal stability in water to small CuS PNPs. The developed protocol allows controlling the shape and position of the localized surface plasmon resonance band possessed by these PNPs. The study of the effect that reaction temperature, pH, PEG amount, and sulfur concentration have on the properties of the reaction product allowed for the optimization of the synthetic approach. Specifically, pure phase covellite PNPs with high heat conversion capabilities (HCE = 44.2 %) were obtained. This result makes these particles excellent candidates as photothermal agents.

Due to the promising properties that characterize CuS PNPs, a complex theranostic system is currently under characterization. This is composed of CuS PNPs and RE-doped fluoride NPs (Figure 6.1). The latter species have been designed in order to display both upconversion and classical luminescence under 806 nm excitation. I synthesized the composite nano-structure growing a mesoporous silica coating on the fluoride NPs and later modifying the surface of this silica intermediate layer to favor its electrostatic interaction with CuS PNPs. Thanks to this particular design, the so-composed nano-structure shows charming properties as a potential theranostic agent. The preliminary results of nano-structure characterization confirm that the different moieties composing the system allow for the simultaneous accomplishment of different tasks under laser irradiation:

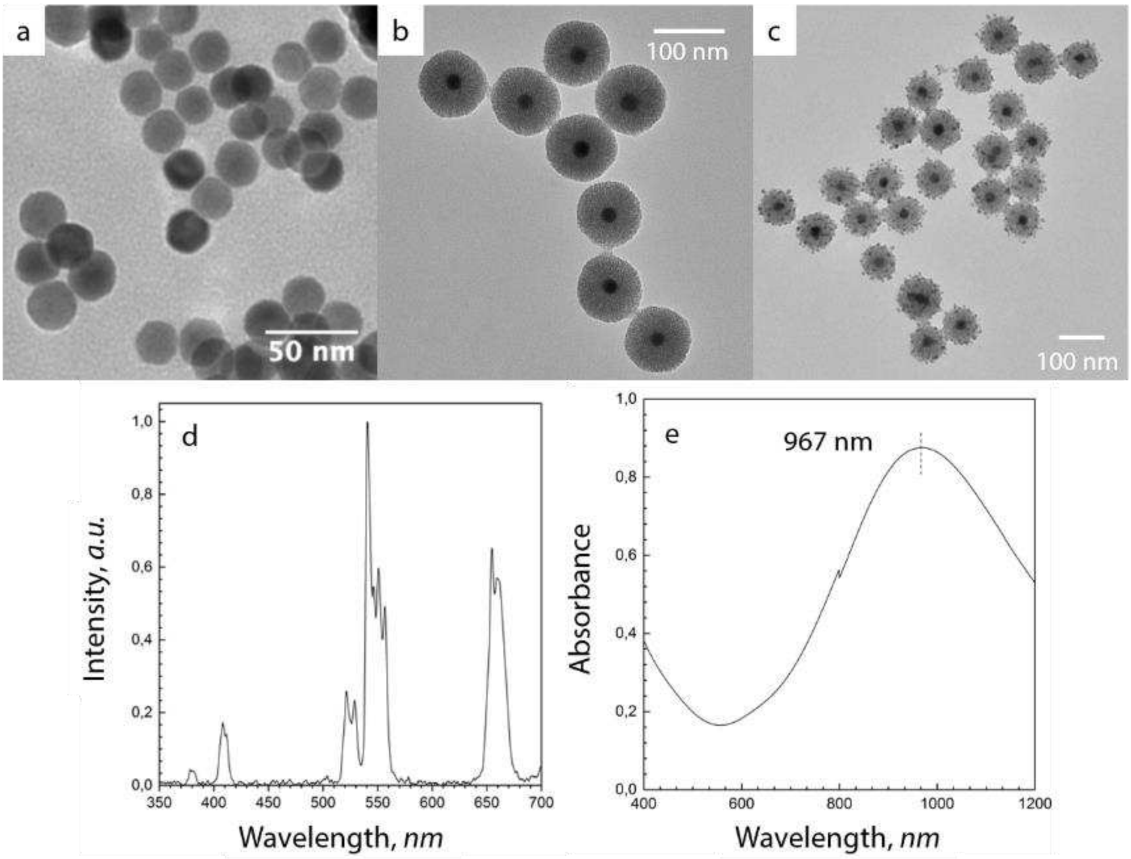

**Figure 6.1.** RE-doped fluoride NPs (*a*) were coated with a mesoporous silica layer (*b*) and then coupled with CuS PNPs (*c*). The upconversion emission under 806 nm excitation is retained from the NPs upon encapsulation in silica (*d*), while the final structure shows promising heat conversion capabilities under 980 nm laser irradiation due to the strong plasmonic absorption displayed by CuS PNPs in the NIR region (*e*).

i) CuS PNPs generate heat through the photothermal effect;

ii) fluoride NP emission can be used both to spatially locate the nano-structure and attempts are being performed to locally probe the temperature increase (thanks to the thermal response of RE emission);

iii) a drug can be loaded in the mesoporous silica shell, endowing the system with drug delivery capabilities.

Although first encouraging results, more analyses are needed in order to fully characterize this system and establish its applicability as a powerful nanostructure for self-monitored photothermal therapy.